The Astrophysical Journal, 797:54 (30pp), 2014 December 10 doi:10.1088/0004-637X/797/1/54

ULTRALUMINOUS INFRARED GALAXIES IN THE *AKARI* ALL-SKY SURVEY

E. Kilerci Eser[1], T. Goto[2], and Y. Doi[3]
[1] Dark Cosmology Centre, Niels Bohr Institute, University of Copenhagen, Juliane Maries Vej 30, DK-2100 Copenhagen Ø, Denmark; ecekilerci@dark-cosmology.dk
[2] National Tsing Hua University, No. 101, Section 2, Kuang-Fu Road, Hsinchu 30013, Taiwan; tomo@phys.nthu.edu.tw
[3] The University of Tokyo, Komaba 3-8-1, Meguro, Tokyo 153-8902, Japan; doi@ea.c.u-tokyo.ac.jp
Received 2014 January 10; accepted 2014 September 19; published 2014 November 25

ABSTRACT

We present a new catalog of 118 ultraluminous infrared galaxies (ULIRGs) and one hyperluminous infrared galaxy (HLIRG) by cross-matching the *AKARI* all-sky survey with the Sloan Digital Sky Survey Data Release 10 (SDSS DR10) and the final data release of the Two-Degree Field Galaxy Redshift Survey. Forty of the ULIRGs and one HLIRG are new identifications. We find that ULIRGs are interacting pair galaxies or ongoing or postmergers. This is consistent with the widely accepted view: ULIRGs are major mergers of disk galaxies. We confirm the previously known positive trend between the active galactic nucleus fraction and infrared luminosity. We show that ULIRGs have a large offset from the main sequence up to $z \sim 1$; their offset from the $z \sim 2$ "main sequence" is relatively smaller. We find a result consistent with the previous studies showing that, compared to local star-forming SDSS galaxies of similar mass, local ULIRGs have lower oxygen abundances. We demonstrate for the first time that ULIRGs follow the fundamental metallicity relation (FMR). The scatter of ULIRGs around the FMR (0.09 dex–0.5 dex) is comparable to the scatter of $z \sim 2$–3 galaxies. We provide the largest local ($0.050 < z < 0.487$) ULIRG catalog with stellar masses, star-formation rates, gas metallicities, and optical colors.

Key words: galaxies: general – galaxies: interactions – galaxies: starburst – infrared: galaxies

Online-only material: color figures

1. INTRODUCTION

Luminous infrared galaxies (LIRGs), ultraluminous infrared galaxies (ULIRGs), and hyperluminous infrared galaxies (HLIRGs) are defined by their high IR luminosities that are in the $10^{11}\,L_\odot \leqslant L_{\rm IR} < 10^{12}\,L_\odot$, $10^{12}\,L_\odot \leqslant L_{\rm IR} < 10^{13}\,L_\odot$, and $10^{13}\,L_\odot \leqslant L_{\rm IR}$ ranges, respectively (see the reviews by Sanders & Mirabel 1996; Lonsdale et al. 2006). The observed enormous IR luminosity is driven by the optical and ultraviolet (UV) radiation generated by intense star formation and active galactic nuclei (AGNs) that is absorbed by dust and re-emitted in the IR. ULIRGs have been considered as a transition phase from mergers to dusty quasars (Sanders et al. 1988b; Veilleux et al. 2002) such that when gas-rich spiral galaxies merge, the molecular gas clouds channeling toward the merger nucleus trigger nuclear starbursts and AGN activity by the accretion of the available fuel onto the central supermassive black hole (SMBH). According to this scenario, the starburst phase evolves to a dust-enshrouded AGN phase, and once the gas and dust are consumed, the system evolves to a bright QSO phase.

Tidal interactions and merger processes between galaxies play a major role in the formation of elliptical galaxies (Toomre & Toomre 1972). In particular, the proposed scenario by Sanders et al. (1988b) motivated further investigation of the link between mergers and quasars in numerical simulations. Hydrodynamical simulations of mergers show that merger processes lead gas inflows toward the center that trigger starbursts and AGN activity (e.g., Springel et al. 2005). In the merger-driven galaxy evolution simulations, ULIRGs represent a contemporary starburst and AGN phase at the beginning of rapid self-regulated SMBH growth (e.g., Di Matteo et al. 2005; Hopkins et al. 2007). ULIRGs evolve to red or elliptical-type remnants by negative feedback mechanisms (e.g., in the form of powerful winds and outflows) that inhibit star formation and AGN activity (e.g., Hopkins et al. 2006, 2008a, 2008b, 2009).

The link that emerged between ULIRGs and QSOs is supported by much observational evidence. The morphological properties of ULIRGs indicate that they are interacting galaxies in pre-, ongoing, or late-merger stages (Farrah et al. 2001; Kim et al. 2002; Veilleux et al. 2002, 2006). Compared to LIRGs that are disk galaxies (if $\log(L_{\rm IR}/L_\odot) < 11.5$) or interacting systems (if $11.5 \leqslant \log(L_{\rm IR}/L_\odot) < 12.0$), ULIRGs are mostly advanced mergers (Veilleux et al. 2002; Ishida 2004). Their dynamical masses obtained from near-infrared (NIR) spectroscopy show that they are major mergers of nearly equal mass galaxies (Veilleux et al. 2002; Dasyra et al. 2006a, 2006b). CO observations proved that ULIRGs contain the required cold molecular gas for central starbursts (Downes & Solomon 1998). In addition, their mid-infrared (MIR) images show that MIR emission is generated in a region of diameter ∼1 kpc (Soifer et al. 2000). At least ∼70% of 164 local ($z \leqslant 0.35$) ULIRGs harbor an AGN (Nardini et al. 2010). The coexistence of a starburst and an AGN show that both energy sources contribute to the total IR luminosity. The AGN fraction and the strength of the AGN emission increases with IR luminosity; high-luminosity ULIRGs ($\log(L_{\rm IR}/L_\odot) > 12.5$) and HLIRGs have a larger AGN contribution than do lower luminosity IR galaxies (Veilleux et al. 1995, 1999b, 2002, 2009; Genzel et al. 1998; Goto 2005; Imanishi 2009; Nardini et al. 2010). ULIRGs show starburst- and AGN-driven powerful outflows (e.g., Heckman et al. 2000; Rupke et al. 2002, 2005; Rupke & Veilleux 2011, 2013; Spoon et al. 2013; Veilleux et al. 2013, and references therein) that are consistent with the negative feedback mechanisms expected for their evolution.

The significance of ULIRGs in galaxy evolution is not limited to the local ($z < 0.3$) universe because at high redshift ($z > 1$) they are more numerous and have a substantial contribution to the total IR luminosity density (Le Floc'h et al. 2005; Caputi et al. 2007) compared to local ULIRGs (Soifer & Neugebauer 1991; Kim & Sanders 1998). There is a significant population of

ULIRGs beyond $z \sim 1$ (e.g., Goto et al. 2011b). An important question is the powering mechanism of these sources: are they powered by interaction-induced nuclear starbursts or AGN, or are they normal or undisturbed star-forming galaxies? The key properties that would answer this question are morphologies, spectral energy distributions (SEDs), and the extent of star-forming regions. Observations have shown that ULIRGs at high redshift ($1.5 < z < 3.0$) are mostly ($\sim$47%) mergers or interacting galaxies, but this sample also includes noninteracting disks, spheroids, and irregular galaxies (Kartaltepe et al. 2012). Beyond $z > 2$, the morphological properties of submillimeter galaxies (SMGs) are consistent with mergers and interacting systems (e.g., Tacconi et al. 2008). The morphologies of high-z samples show that mergers or interactions are taking place in these systems, and even a comparison of $z \sim 2$ and $z \sim 1$ samples indicates a hint of a morphological evolution such that $z \sim 1$ samples have slightly more mergers and interacting galaxies (Kartaltepe et al. 2012). The SEDs of high-redshift ULIRGs are different from those of local ones. For example, they exhibit prominent polycyclic aromatic hydrocarbon (PAH) features more similar to those of local, lower IR luminosity ($10.0 \leqslant \log(L_{\rm IR}/L_{\odot}) < 11.0$) star-forming galaxies (SFGs) than those of local ULIRGs (e.g., Farrah et al. 2008; Takagi et al. 2010). Because PAH emission indicates ongoing star formation, observations support the idea that high-z ULIRGs are starburst dominated. A similar conclusion is also achieved by the X-ray studies of high-z ULIRGs (e.g., Johnson et al. 2013). The size of the star-forming regions of high-z ULIRGs are larger than those of local ULIRGs with similar $L_{\rm IR}$ (Rujopakarn et al. 2011). This suggests that in these galaxies star formation does not occur in merger nuclei, but instead it is distributed galaxy-wide. The similarities of star-forming regions of high-z ULIRGs and local quiescent SFGs point to a different origin than merger-induced star formation (Rujopakarn et al. 2011). Although the evolution of ULIRGs is not fully understood yet, the observations provide evidence for changing properties with redshift.

Understanding the role of ULIRGs in galaxy evolution through cosmic time requires extensive studies and comparison of local and high-z samples. Local ULIRGs establish a basis for understanding the nature of ULIRGs, the origin of their extreme luminosities, and the interplay between star formation and AGN activity in the nearby mergers. Therefore, it is important to have a large local sample and to master its overall properties. The great majority of local ULIRGs are discovered with the *InfraRed Astronomy Satellite* (*IRAS*). *IRAS* performed an all-sky scan in four IR bands centered at 12 μm, 25 μm, 60 μm, and 100 μm. The *IRAS* Bright Galaxy Survey (BGS) catalog (Soifer et al. 1987) includes 10 ULIRGs selected on the basis of 60 μm flux, $F(60\,\mu\text{m})$. This catalog was replaced by the *IRAS* Revised Bright Galaxy Sample (Sanders et al. 2003), which provided more accurate infrared luminosities and increased the number of ULIRGs to 21. The *IRAS* 2 Jy (Strauss et al. 1992) and 1.2 Jy (Fisher et al. 1995) redshift surveys identified new ULIRGs. Sanders et al. (1988a) showed that ULIRGs with warmcolors ($F(25\,\mu\text{m})/F(60\,\mu\text{m}) > 0.2$) have Seyfert-like spectra, and therefore ULIRGs were separated into warm AGN-hosting and coldstar formation dominated systems. An analysis of the BGS sample showed that the $F(60\,\mu\text{m})/F(100\,\mu\text{m})$ color increases with higher $L_{\rm IR}$ (Soifer & Neugebauer 1991). A widely studied large sample of local ULIRGs is the *IRAS* 1 Jy sample (Kim et al. 1998). This is a complete flux-limited sample at 60 μm that is composed of 118 ULIRGs identified from the *IRAS* Faint Source Catalog (FSC; Moshir et al. 1992) and a dedicated redshift survey (Kim et al. 1998). Because previous studies (Soifer & Neugebauer 1991; Strauss et al. 1992) showed that $F(60\,\mu\text{m})/F(100\,\mu\text{m})$ color increases with higher $L_{\rm IR}$ and that ULIRG colors are in the range of $-0.2 < F(60\,\mu\text{m})/F(100\,\mu\text{m}) < 0.13$, the *IRAS* 1 Jy sample ULIRGs were selected based on their warm colors ($F(60\,\mu\text{m})/F(100\,\mu\text{m}) > 0.3$) (Kim et al. 1998). With other redshift surveys such as the QDOT all-sky *IRAS* galaxy redshift survey (Lawrence et al. 1999), the *IRAS* Point Source Catalog Redshift survey (Saunders et al. 2000), and the FIRST/IRAS radio–far-IR sample (Stanford et al. 2000), the number of IRAS ULIRGs increased. Large galaxy redshift surveys like the Sloan Digital Sky Survey (SDSS; York et al. 2000) and the Two-Degree Field Galaxy Redshift Survey (2dFGRS; Colless et al. 2001) provide the redshifts of millions of galaxies. In particular, the SDSS made it possible to study the optical properties of a large sample of IR galaxies. Goto (2005) cross-correlated the *IRAS* FSC with the SDSS Data Release 3 (DR3; Abazajian et al. 2005) spectroscopic catalog and identified 178 ULIRGs. Pasquali et al. (2005) cross-correlated the SDSS DR2 (Abazajian et al. 2004) with the *IRAS* FSC and investigated the IR properties of local AGNs and star-forming galaxies. Cao et al. (2006) cross-correlated the *IRAS* FSC and the Point Source Catalog (PSC) with the SDSS DR2 and identified a small sample of ULIRGs. Hwang et al. (2007) identified 324 ULIRGs, including 190 new discoveries, by cross-correlating *IRAS* FSC with SDSS DR4 (Adelman-McCarthy et al. 2006), 2dFGRS, and the second data release of the 6dF Galaxy Survey (Jones et al. 2004). Hou et al. (2009) cross-correlated the *IRAS* FSC with the SDSS DR6 (Adelman-McCarthy et al. 2008) and identified 308 ULIRGs.

The largest all-sky IR survey after *IRAS* was completed by the Japanese IR satellite launched in 2006, *AKARI* (Murakami et al. 2007), which scanned almost all of the sky in 9 μm, 18 μm, 65 μm, 90 μm, 140 μm, and 160 μm bands. The resolution and sensitivity of *AKARI* is better than those of *IRAS*: the point-spread function (PSF) of *AKARI* is $\sim$39″ (for the 90 μm band), and the PSF of *IRAS* is $\sim$4′ (for the 100 μm band); at 18 μm *AKARI* is 10 times more sensitive. Another advantage of *AKARI* is that it has a wider and longer wavelength coverage than *IRAS*. In particular, the 140 μm and 160 μm bands are very important in order to measure the peak of the dust emission near 100 μm and therefore obtain more accurate IR luminosity. Goto et al. (2011b) matched *IRAS* IR sources with SDSS DR7 (Abazajian et al. 2009) galaxies and measured the local IR luminosity function. In this study, Goto et al. (2011b) identified ULIRGs among *AKARI* sources, but they did not provide a detailed catalog of these sources. In this work, we search for ULIRGs and HLIRGs in the *AKARI* all-sky survey. We cross-correlate the *AKARI* all-sky survey with 2dFGRS and the largest SDSS spectroscopic redshift catalog DR 10 (Ahn et al. 2014). In addition to the redshift information, the SDSS has a rich view of optical properties of the sources in this database. The optical images, spectra, colors, and value-added catalogs with emission-line properties provided by SDSS D10 give us an opportunity to investigate the morphologies, colors, stellar mass, and metallicities of the local ULIRGs identified in the *AKARI* all-sky survey. We provide the first catalog of ULIRGs identified in the *AKARI* all-sky survey.

This paper has the following structure. We introduce the data to identify ULIRGs/HLIRGs and our final sample in Section 2. Our results are presented in Section 3. In Section 4, we discuss our results. This work is summarized in Section 5. Throughout this work, we adopt a cosmology with $H_0 = 70$ km s^{-1} Mpc^{-1}, $\Omega_\Lambda = 0.7$, and $\Omega_m = 0.3$.

2. IDENTIFICATION OF ULTRALUMINOUS AND HYPERLUMINOUS INFRARED GALAXIES IN THE *AKARI* ALL-SKY SURVEY

2.1. The Samples

2.1.1. The AKARI All-sky Survey Catalogs

The *AKARI* all-sky survey provides two catalogs of the IR sources across more than ∼97% of the whole sky with fluxes centered on two mid-IR and four far-IR bands. The *AKARI*/IRC all-sky survey point source catalog version 1[4] includes 870,973 IR sources with fluxes in the 9 μm and 18 μm mid-IR bands. The *AKARI*/FIS all-sky survey bright source catalog version 1[5] (Yamamura et al. 2010) contains 427,071 sources detected at 90 μm with flux measurements in the 65 μm 90 μm 140 μm and 160 μm FIR bands. In particular, the 140 μm and 160 μm fluxes are very important in constraining the FIR SED peak and measuring $L_{\rm IR}$.

In order to have a single *AKARI*/FIS/IRC catalog with both FIR and mid-IR fluxes, we cross-match the IR sources in the *AKARI*/FIS all-sky survey bright source catalog with the *AKARI*/IRC all-sky survey point source catalog within a radius of 20″. The resulting *AKARI*/FIS/IRC catalog contains 24,701 sources based on 90 μm detections.

To measure the IR luminosity, we obtain the spectroscopic redshifts of the IR galaxies from their optical counterparts. We cross-correlate the *AKARI*/FIS/IRC catalog with the large optical redshift catalogs as described in the following.

2.1.2. The AKARI–SDSS DR10 Sample

The SDSS is the largest ground-based survey that provides a unique photometric and spectroscopic database of stars, galaxies, and quasars. The SDSS is a red magnitude limited $r < 17.7$ survey over 14,555 deg^2 of the sky. We have downloaded the SDSS DR 10 (Ahn et al. 2014) catalogs *photoObj*[6] and *specObj*[3] to extract both photometric and spectroscopic information. The *photoObj* catalog includes all photometric information from previous data releases, and the *specObj* catalog includes new spectra from the Baryon Oscillation Spectroscopic Survey[7] (BOSS). We combined the two catalogs by matching OBJID in *photoObj* to "BESTOBJID" in *specObj* to obtain a full SDSS catalog of 2,745,602 sources with spectroscopic and photometric information.

The *AKARI*/FIS/IRC catalog is cross-matched with the full SDSS catalog. The astrometric precision of SDSS (∼0.″1 at $r = 19$ mag Pier et al. 2003) is much better than that of *AKARI* (∼4.″8 Yamamura et al. 2010). We follow Goto et al. (2011b) and select matching radii as 20″ because this radius is large enough to contain different emission regions (e.g., IR and optical) in a single galaxy; it is also small enough to not allow too many optical chance identifications that are not physically related to the IR source. Although we pick 20″ to be inclusive and not miss any real association, in order to eliminate any misassociation later, we check the positional overlap of the IR and the optical emission from each ULIRG candidate by eye. We avoid any duplicated matches, i.e., each IR galaxy is allowed to match only one SDSS counterpart. We obtain 6,468 matches of *AKARI*–SDSS sources. Among those we removed the sources that were classified as stars in the *specObj* catalog. This resulted in a *AKARI* SDSS sample of 6,373 galaxies. For the IR sources in this sample we adopt the SDSS spectroscopic redshifts.

2.1.3. The AKARI–2dFGRS Sample

The 2dFGRS (Colless et al. 2001) measured redshifts of 245,951 galaxies within a $b_j < 19.45$ limit. The median redshift of this survey is $z \sim 0.1$ (Colless 2004). We use the final data release of the 2dFGRS, the catalog of *best spectroscopic observations*.[8] We cross-match the *AKARI*/FIS/IRC catalog with the 2dFGRS catalog with a matching radius of 20″. We obtain a *AKARI*–2dFGRS sample of 954 galaxies with spectroscopic redshifts from 2dFGRS.

2.2. Infrared Luminosity Measurements

To estimate the total IR luminosity for the galaxies in the *AKARI*–SDSS and *AKARI*–2dFGRS samples, we perform an SED fitting using the *LePhare*[9] (Photometric Analysis for Redshift Estimations) code (Arnouts et al. 1999; Ilbert et al. 2006). The main function of the *LePhare* is to compute photometric redshifts, but it can also find the best-fitting galaxy template by a χ^2 fit for the given photometric magnitudes among the input template libraries. For the *AKARI*–SDSS and *AKARI*–2dFGRS samples, we use the six *AKARI* bands with their associated uncertainties adopted from the *AKARI* catalogs; if the flux uncertainty is not given, we adopt 25% of the measured flux as the uncertainty. We use the FIR SED templates of Dale & Helou (2002) as the input library. Dale & Helou (2002) provide 64 SED templates generated semiempirically to represent the IR SEDs of star-forming galaxies. Compared to other SED models, such as the models of Chary & Elbaz (2001), these templates include FIR improvements based on *ISO*/*IRAS*/*SCUBA* observations. However, they do not include more sophisticated dust emission modeling as provided by Siebenmorgen & Krügel (2007). Because our main focus is on measuring $L_{\rm IR}$, we avoid more sophisticated models and prefer the templates of Dale & Helou (2002) for the SED fitting. We fix the redshift of each galaxy and fit the FIR region of the SED with the *AKARI* broadband photometry. In the fitting procedure, k corrections are applied to the *AKARI* fluxes. In order to obtain the k correction, our model flux is computed by integrating the redshifted SED model flux through *AKARI*'s filter response function. The best-fit dust templates of Dale & Helou (2002) are shown in Figure 1 (left column) for representative cases. The *AKARI*/FIS name is given in the top left corner. The best-fit templates are shown as solid magenta lines. The black filled circles are the optical (shown only for illustration purposes) and *AKARI* photometric fluxes; the x-axis error bars represent the wavelength range of each photometric band.

As a result of the SED fitting, we obtain the total infrared luminosity integrated between 8 μm and 1000 μm, L_{8-1000} with the maximum and minimum possible L_{8-1000} value based on the flux errors. These are used to determine the upper and lower uncertainties of L_{8-1000}.

Based on the obtained L_{8-1000}, our initial sample includes 170 ULIRG and 10 HLIRG candidates: the *AKARI*–SDSS sample

[4] http://www.ir.isas.jaxa.jp/AKARI/Observation/PSC/Public/RN/AKARI-IRC_PSC_V1_RN.pdf
[5] http://www.ir.isas.jaxa.jp/AKARI/Observation/PSC/Public/RN/AKARI-FIS_BSC_V1_RN.pdf
[6] http://www.sdss3.org/dr10/spectro/spectro_access.php
[7] http://www.sdss3.org/surveys/boss.php
[8] http://www2.aao.gov.au/∼TDFgg/
[9] http://www.cfht.hawaii.edu/∼arnouts/lephare.html

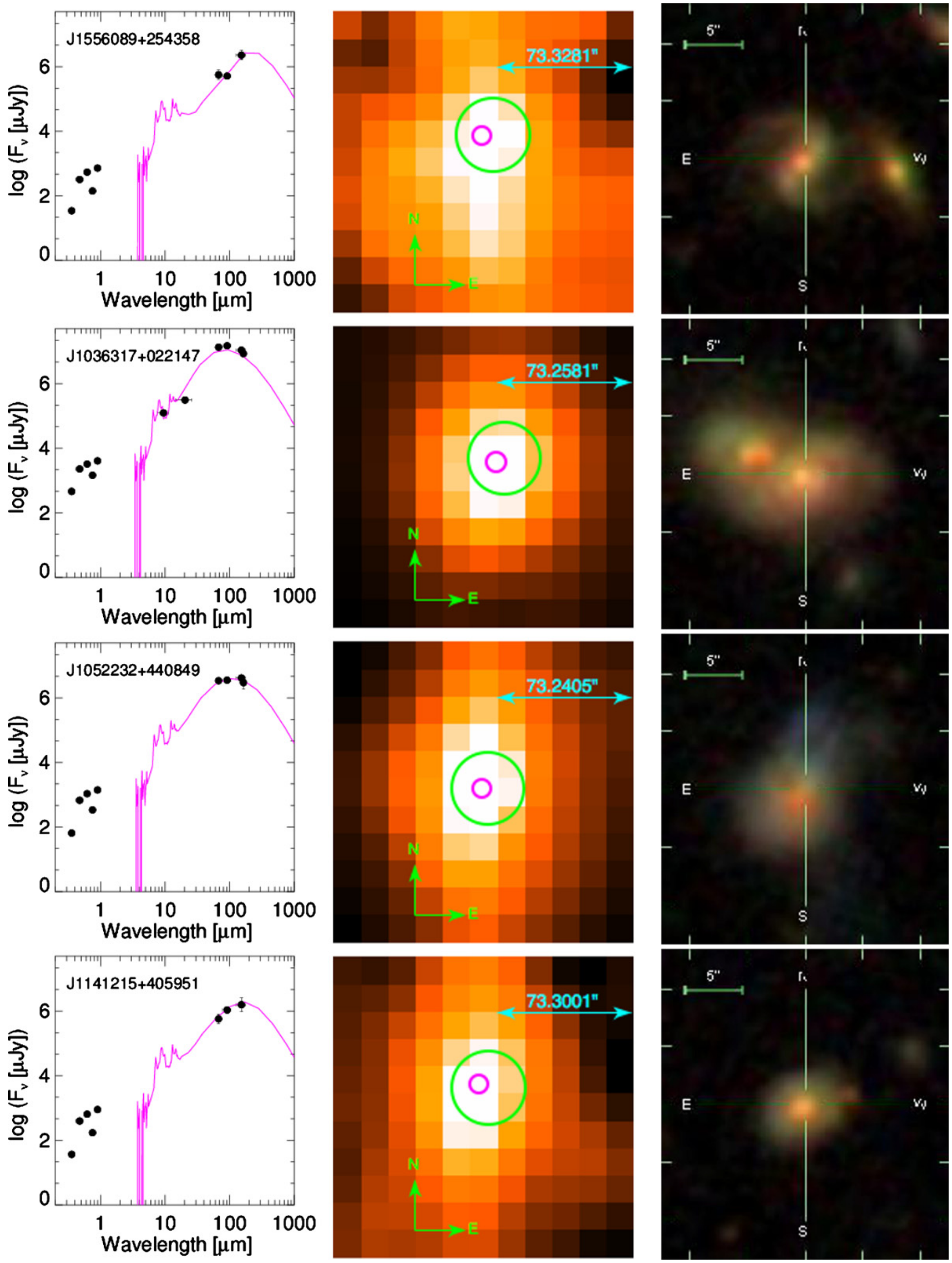

Figure 1. SEDs (left), *AKARI* (middle), and SDSS *g-r-i* color combined images (right) of the four nearest ULIRGs classified as IIIa (first row), IIIb (second row), IV (third row), and IV (fourth row). The scale of the *AKARI* 90 μm images are $165'' \times 165''$. The small $5''$ radius (colored magenta in the online version) and the large $20''$ radius (colored green in the online version) circles mark the optical and IR sources, respectively.

(A color version of this figure is available in the online journal.)

has 135 ULIRG and eight HLIRG candidates, and the *AKARI* 2dFGRS has 35 ULIRG and two HLIRG candidates. In order to have a reliable sample of ULIRGs and HLIRGs, we check each case to avoid any wrong identification as described in the following.

2.3. Elimination of the Mismatches

The (H)ULIRG candidates in our initial sample are selected based on the optical spectroscopic redshifts by matching the closest optical galaxy to the *AKARI* source. If there is more than one source satisfying the cross-match condition, then the one with the smallest positional difference is considered to be a match. Even though the positions of the optical and IR sources are close in the sky, it does not necessarily mean that the IR and optical emissions are counterparts of the same galaxy; further care is required to make this decision.

Although the optical and IR galaxies are matched within a 20″ radius, we visually check the positional overlap of the IR and optical emission in the *AKARI* images for each galaxy. For the optical counterpart we use SDSS (if available) or Digitized Sky Survey images. Examples of *AKARI* (middle panel) and optical (right panel) images are represented in Figure 1. The SDSS images are *gri* combined color images downloaded from the SDSS DR10 Finding Chart Tool.[10] In the *AKARI* images (Doi et al. 2012), the green circle represents the 20″ radius limit, whereas the optical source is marked with a 5″ radius magenta circle. Once we verify the positional overlap of the matched IR and optical sources, next we check whether there are any other sources overlapping with the IR source and possibly contaminating the IR emission. Such contaminating sources can be stars or other galaxies. In particular, nearby bright galaxies lying over the IR source contribute to the observed IR emission, and therefore such cases are eliminated from the initial sample. If there is more than one overlapping optical galaxy with similar separation values within the 20″ radius region, the closest one is not necessarily the true match. Because it is difficult to select the true optical counterpart for these four cases, these are eliminated. It is a concern if we are automatically removing compact groups of galaxies in these cases, but before we eliminate these we consider the redshifts of these galaxies and check if they are in groups.

Although the SDSS provides a large redshift database, not all galaxies have the spectroscopic information. Related to this, in some cases the optical source with the smallest positional difference is not included in the cross-match procedure. Therefore, the images show that instead of the true optical counterpart, some other optical galaxy with a large separation (8″.12–18″.87) is matched with the IR emission. For these cases we look at the literature (e.g., Wang & Rowan-Robinson 2009) and check if the true optical counterpart has a spectroscopic redshift. If the redshift is not known for the "true" optical counterpart, we eliminate these cases. If the redshift is known, we adopt it for the true optical counterpart and reobtain L_{8-1000}. Three cases (marked with an asterisk in Column 5 of Tables 1 and 2) for which $10^{12}\,L_\odot \leqslant L_{8-1000}$ are kept in the sample.

After we secure the optical and IR galaxy match by visual inspection, as an additional control we check the adopted spectroscopic redshifts. For the *AKARI*–2dFGRS sample we require a redshift quality of ⩾3. This requirement led to elimination of two ULIRG and two HLIRG candidates from the *AKARI*–2dFGRS sample. For the *AKARI*–SDSS sample, we go through the SDSS spectra.[11] The SDSS spectra are reduced through the spectroscopic pipeline (Bolton et al. 2012). The SDSS pipeline determines the classification and the redshift of the spectra by applying a χ^2 fit with rest-frame templates of stars, galaxies, and quasars. By looking at the SDSS spectra we eliminate the following cases from the sample: (1) the sources that are classified as a galaxy but show a spectrum of a star, and (2) the spectra that show an unreliable template fit and therefore indicate a wrong redshift.

2.4. The Final Sample

Our final sample of (H)ULIRGs consists of 119 galaxies: 97 are identified in the *AKARI*–SDSS sample and 22 are identified in the *AKARI*–2dFGRS sample. In order to specify the newly identified (H)ULIRGs in this work, we check our final sample against previously studied samples: Clements et al. (1996), Kim et al. (1998), Rowan-Robinson (2000), Hwang et al. (2007), Hou et al. (2009), and Nardini et al. (2010). Thus 40 ULIRGs and one HLIRG are newly identified in this work. The IR images of the newly identified ULIRGs and one HLIRG are available in the Appendix (Figure A1). We divide the final sample into three subsamples: (1) new ULIRGs identified in this work, (2) known ULIRGs, and (3) new HLIRGs identified in this work. The properties of these subsamples are listed in Tables 1, 2, and 3, respectively. These tables contain the *AKARI* name (Column 1), the *AKARI* coordinates R.A. and decl. (Columns 2 and 3, respectively), other name (Column 4), redshift (Column 5), total IR luminosity, $L_{\rm IR}$, (Column 6), *AKARI* photometric fluxes of the 65 μm (F(65 μm)), 90 μm (F(90 μm)), 140 μm (F(140 μm)), and 160 μm (F(160 μm)) bands (Columns 7, 8, 9, and 10, respectively), SDSS Petrosian r magnitude (Column 11), interaction class (IC; Column 12), reference for IC (Column 13), note related to optical images indicating if there is a star or other galaxies in the field (Column 14), and spectral classification (Column 15). Because we have only a few sources detected in the 9 μm and 18 μm bands, we do not list the photometric fluxes at these bands.

We note that three of the new ULIRGs listed in Table 1 have 65 μm fluxes above 1 Jy, the flux threshold of the 1 Jy sample of Kim et al. (1998), and have declination $\delta > -40$ deg and galactic latitude $b > 30$ deg and therefore should have made it into the 1 Jy sample. However, two of these sources (J1036317+022147 and J1125319+290316) are not observed with *IRAS*. The 60 μm flux of J0857505+512037 is below 1 Jy (∼0.6 Jy Moshir et al. 1992), and therefore it is not in the 1 Jy sample of Kim et al. (1998).

In Table 4 we list five additional ULIRG candidates that are considered as unconfirmed cases either because their IR detection is not significant (almost at 5σ) or the separation between the matched optical and IR coordinates are large (∼20″). We do not include those five sources in the final sample.

3. ANALYSIS AND RESULTS

3.1. Basic Properties of the AKARI ULIRG and HLIRG Samples

3.1.1. Redshift and $L_{\rm IR}$ Distributions

The redshift and IR luminosity distributions of our final sample are presented in the top and bottom panels of Figure 2, respectively. The redshift distribution covers $0.050 < z < 0.487$, with a median redshift of $\bar{z} = 0.181$. We have 104 ULIRGs distributed over the $0.050 < z \leqslant 0.270$ range, and 14 ULIRGs are within the $0.270 < z < 0.487$ range. The IR luminosity distribution of 80 ULIRGs covers the $12.0 \leqslant L_{\rm IR} \leqslant 12.25$ range. The higher luminosity range of $12.25 < L_{\rm IR} \leqslant 12.91$ includes 38 ULIRGs.

Figure 3 shows the IR luminosity of our sample as a function of redshift. As expected from the *AKARI* PSC detection limit (0.55 Jy at 90 μm), $L_{\rm IR}$ increases with redshift, and only the bright sources can be detected toward the higher redshifts.

[10] http://skyserver.sdss3.org/dr10/en/tools/chart/chartinfo.aspx
[11] http://dr10.sdss3.org/basicSpectra

Table 1
New ULIRG Sample

Name AKARI-FIS-V1 (1)	*AKARI* R.A. (J2000) (2)	*AKARI* Decl. (J2000) (3)	Other Name (4)	z[a] (5)	$\log(L_{\rm IR}/L_\odot)$[b] (6)	F(65 μm)[c] (Jy) (7)	F(90 μm)[c] (Jy) (8)	F(140 μm)[c] (Jy) (9)	F(160 μm)[c] (Jy) (10)	r[d] (mag) (11)	IC[e] (12)	IC[f] Ref. (13)	Note[g] (14)	Spectral[h] Class (15)
J2216028+005813	22 16 02.82	+00 58 13.5	SDSS J221602.70+005811.0	0.21*	$12.83^{+0.15}_{-0.14}$	0.54 ± 0.13	0.54 ± 0.05	0.96 ± 0.63	1.14 ± 0.28	14.30	IIIa	3	···	···
J0859229+473612	08 59 22.93	+47 36 11.7	SDSS J085923.61+473610.5	0.180	$12.20^{+0.01}_{-0.09}$	···	0.48 ± 0.06	1.95 ± 0.29	···	14.44	IIIa	3	···	Star forming
J1443444+184950	14 43 44.44	+18 49 49.7	SDSS J144344.64+184945.7	0.177	$12.21^{+0.01}_{-0.31}$	0.43 ± 0.11	0.55 ± 0.04	1.69 ± 0.53	···	16.03	V	3	···	LINER
J0857505+512037	08 57 50.48	+51 20 37.2	SDSS J085750.79+512032.6	0.366	$12.89^{+0.07}_{-0.02}$	1.12 ± 0.28	0.68 ± 0.06	1.58 ± 0.08	···	14.40	IIIb	3	···	LINER
J1106104+023458	11 06 10.37	+02 34 57.8	SDSS J110611.44+023502.2	0.283	$12.23^{+0.06}_{-0.06}$	···	0.42 ± 0.01	1.42 ± 0.36	0.56 ± 0.14	17.17	NI	3	B	Seyfert
J1157412+321316	11 57 41.21	+32 13 16.4	SDSS J115741.47+321316.4	0.160	$12.14^{+0.01}_{-0.12}$	0.66 ± 0.16	0.60 ± 0.03	2.22 ± 1.21	2.23 ± 0.40	16.37	V	3	···	Star forming
J1149200−030357	11 49 20.03	−03 03 57.3	SDSS J114920.04−030402.1	0.162	$12.02^{+0.02}_{-0.04}$	0.19 ± 0.05	0.42 ± 0.02	1.30 ± 0.33	2.58 ± 0.21	13.97	V,G	3	···	Star forming
J0126038+022456	01 26 03.80	+02 24 55.9	SDSS J012604.62+022509.9	0.242	$12.22^{+0.04}_{-0.06}$	···	0.63 ± 0.01	0.70 ± 0.18	···	14.73	Tp1,G	3	···	LINER
J1556089+254358	15 56 08.92	+25 43 57.8	SDSS J155609.36+254355.9	0.154	$12.03^{+0.01}_{-0.26}$	0.56 ± 0.14	0.51 ± 0.01	2.26 ± 0.57	···	16.76	IIIa,G	3	···	Composite
J0140364+260016	01 40 36.40	+26 00 15.9	SDSS J014037.36+260001.5	0.321	$12.77^{+0.06}_{-0.02}$	0.57 ± 0.14	0.56 ± 0.03	0.70 ± 0.17	2.51 ± 0.15	16.01	IIIa,G	3	···	Seyfert
J1257392+080935	12 57 39.15	+08 09 35.1	SDSS J125739.33+080931.7	0.272	$12.24^{+0.04}_{-0.02}$	0.46 ± 0.12	0.51 ± 0.01	···	0.22 ± 0.06	17.72	NI	3	···	QSO
J0800007+152319	08 00 00.68	+15 23 18.7	SDSS J080000.05+152326.0	0.274	$12.14^{+0.00}_{-0.00}$	···	0.43 ± 0.03	···	···	14.50	V	3	A	LINER*
J0800279+074858	08 00 27.92	+07 48 57.6	SDSS J080028.37+074915.5	0.173	$12.12^{+0.00}_{-0.09}$	0.34 ± 0.09	0.35 ± 0.09	2.29 ± 0.57	2.04 ± 0.51	13.10	V,G	3	···	LINER
J0834438+334427	08 34 43.82	+33 44 27.2	SDSS J083443.56+334432.5	0.166	$12.13^{+0.03}_{-0.20}$	0.59 ± 0.15	0.65 ± 0.04	···	2.07 ± 0.52	15.90	IIIb	3	A	Composite
J0823089+184234	08 23 08.91	+18 42 33.9	SDSS J082309.51+184233.4	0.425	$12.57^{+0.43}_{-0.03}$	0.45 ± 0.11	0.41 ± 0.02	···	···	12.52	V	3	···	···
J1202527+195458	12 02 52.69	+19 54 58.4	SDSS J120252.39+195456.7	0.132	$12.05^{+0.04}_{-0.02}$	0.11 ± 0.03	0.54 ± 0.05	0.69 ± 0.10	3.43 ± 0.04	14.50	IIIb	3	···	Star forming
J0912533+192701	09 12 53.33	+19 27 00.8	SDSS J091253.25+192653.9	0.233	$12.11^{+0.09}_{-0.04}$	0.17 ± 0.04	0.44 ± 0.04	0.68 ± 0.17	0.93 ± 0.23	15.49	V	3	···	Composite
J0941010+143622	09 41 01.03	+14 36 22.4	SDSS J094100.81+143614.5	0.384	$12.75^{+0.01}_{-0.05}$	0.89 ± 0.22	0.77 ± 0.07	0.24 ± 0.06	0.46 ± 0.11	17.19	NI	3	B	QSO
J1016332+041418	10 16 33.25	+04 14 17.9	SDSS J101633.19+041422.1	0.266	$12.39^{+0.03}_{-0.05}$	0.51 ± 0.13	0.65 ± 0.10	0.91 ± 0.01	1.34 ± 0.33	14.73	IIIb	3	···	Composite
J1401186−021131	14 01 18.61	−02 11 30.9	SDSS J140119.02−021126.7	0.172	$12.07^{+0.01}_{-0.08}$	0.26 ± 0.06	0.30 ± 0.08	1.85 ± 0.30	···	15.98	IIIa	3	···	Seyfert
J1258241+224113	12 58 24.10	+22 41 13.0	SDSS J125824.16+224113.6	0.208	$12.07^{+0.05}_{-0.04}$	0.97 ± 0.24	0.60 ± 0.05	1.44 ± 1.09	0.86 ± 0.21	16.62	IIIb	3	···	Composite
J1036317+022147	10 36 31.66	+02 21 47.3	SDSS J103631.88+022144.1	0.050	$12.06^{+0.03}_{-0.04}$	13.32 ± 1.09	14.81 ± 0.54	10.83 ± 1.15	8.46 ± 0.74	14.75	IIIb	3	···	Composite
J1050567+185316	10 50 56.73	+18 53 16.1	SDSS J105056.78+185316.9	0.219	$12.60^{+0.03}_{-0.06}$	0.67 ± 0.17	0.93 ± 0.10	3.08 ± 2.13	3.32 ± 0.45	14.91	Tp1,G	3	···	Seyfert
J1111177+192259	11 11 17.72	+19 22 58.9	SDSS J111117.46+192255.0	0.225	$12.60^{+0.03}_{-0.06}$	···	0.55 ± 0.05	0.05 ± 2.25	···	14.56	IIIb	3	···	Star forming
J1219585+051745	12 19 58.50	+05 17 44.6	SDSS J121958.11+051735.1	0.487	$12.87^{+0.02}_{-0.04}$	0.29 ± 0.07	0.82 ± 0.09	0.43 ± 0.11	···	15.16	NI	3	A	···
J1414276+605726	14 14 27.55	+60 57 25.8	SDSS J141427.98+605727.0	0.151	$12.11^{+0.00}_{-0.12}$	0.37 ± 0.09	0.63 ± 0.04	1.94 ± 0.36	2.75 ± 1.38	14.11	V	3	···	Composite
J0936293+203638	09 36 29.33	+20 36 37.6	SDSS J093629.03+203620.0	0.175	$12.01^{+0.04}_{-0.02}$	0.42 ± 0.11	0.57 ± 0.09	2.05 ± 0.23	0.83 ± 0.21	14.12	IIIb	3	···	Composite
J1533582+113413	15 33 58.15	+11 34 12.7	SDSS J153358.24+113415.8	0.337	$12.32^{+0.08}_{-0.08}$	0.25 ± 0.06	0.33 ± 0.04	0.46 ± 0.11	···	15.29	V,G	3	A	···
J1348483+181401	13 48 48.32	+18 14 00.9	SDSS J134848.32+181357.4	0.179	$12.19^{+0.03}_{-0.03}$	0.42 ± 0.11	0.66 ± 0.04	1.66 ± 0.03	1.17 ± 0.29	14.89	IV	3	···	Composite
J1125319+290316	11 25 31.92	+29 03 16.2	SDSS J112531.90+290311.3	0.138	$12.27^{+0.01}_{-0.05}$	1.98 ± 0.14	1.84 ± 0.09	1.53 ± 0.56	···	13.34	IV	3	···	QSO
J1603043+094717	16 03 04.29	+09 47 17.5	SDSS J160304.57+094707.8	0.152	$12.02^{+0.03}_{-0.03}$	0.79 ± 0.20	0.54 ± 0.07	1.70 ± 0.01	0.36 ± 0.09	13.11	V	3	···	Star forming
J1639245+303719	16 39 24.50	+30 37 19.1	SDSS J163925.01+303709.8	0.224	$12.11^{+0.01}_{-0.05}$	0.51 ± 0.13	0.51 ± 0.04	1.14 ± 0.23	0.12 ± 0.03	16.53	IIIb	3	···	···
J1050288+002806	10 50 28.80	+00 28 06.0	SDSS J105028.49+002807.7	0.216	$12.38^{+0.13}_{-0.08}$	0.53 ± 0.13	0.79 ± 0.06	1.79 ± 0.37	···	14.77	IIIb	3	···	Composite
J0928103+232521	09 28 10.29	+23 25 21.0	SDSS J092810.52+232515.8	0.197	$12.07^{+0.08}_{-0.04}$	0.09 ± 0.02	0.44 ± 0.01	1.13 ± 0.28	···	15.40	IIIb	3	···	Star forming

Table 1
(Continued)

Name AKARI-FIS-V1 (1)	*AKARI* R.A. (J2000) (2)	*AKARI* Decl. (J2000) (3)	Other Name (4)	z[a] (5)	$\log(L_{\mathrm{IR}}/L_{\odot})$[b] (6)	$F(65\,\mu\mathrm{m})$[c] (Jy) (7)	$F(90\,\mu\mathrm{m})$[c] (Jy) (8)	$F(140\,\mu\mathrm{m})$[c] (Jy) (9)	$F(160\,\mu\mathrm{m})$[c] (Jy) (10)	r[d] (mag) (11)	IC[e] (12)	IC[f] Ref. (13)	Note[g] (14)	Spectral[h] Class (15)
J2344170+053520	23 44 17.04	+05 35 19.8	SDSS J234417.43+053533.5	0.267	$12.56^{+0.01}_{-0.19}$	0.64 ± 0.16	0.42 ± 0.06	1.29 ± 0.90	1.80 ± 0.45	15.80	IIIa	3	···	Seyfert
J2353152−313234	23 53 15.20	−31 32 34.5	TGS430Z217	0.185	$12.04^{+0.00}_{-0.12}$	0.37 ± 0.09	0.23 ± 0.06	1.67 ± 0.44	2.78 ± 0.70	14.29	···	···	···	···
J1222488−040307	12 22 48.78	−04 03 07.1	TGN123Z071	0.181	$12.19^{+0.02}_{-0.04}$	0.16 ± 0.04	0.59 ± 0.10	1.68 ± 0.04	1.09 ± 0.27	15.17	···	···	···	···
J1419037−034657	14 19 03.68	−03 46 56.6	TGN145Z052	0.152	$12.09^{+0.01}_{-0.08}$	···	0.61 ± 0.15	1.86 ± 0.66	2.49 ± 0.62	16.95	···	···	···	···
J1048019−013017	10 48 01.87	−01 30 17.4	TGN296Z061	0.167	$12.09^{+0.07}_{-0.07}$	0.49 ± 0.12	1.10 ± 0.15	1.13 ± 0.40	···	13.53	IV	3	···	···
J1338353−041131	13 38 35.29	−04 11 31.4	TGN139Z200	0.175	$12.14^{+0.12}_{-0.22}$	0.40 ± 0.10	0.68 ± 0.29	1.77 ± 0.68	···	15.67	···	···	···	···

Notes.

[a] Based on SDSS optical spectra. The redshifts marked with an asterisk are adopted from Wang & Rowan-Robinson (2009) because there are no available SDSS spectra for these sources.

[b] L_{IR} is the total IR luminosity between 8 and 1000 μm measured from the SEDs fitted to the *AKARI* fluxes at 65, 90, 140, and 160 μm.

[c] The *AKARI* flux density and the associated uncertainties are adopted from Yamamura et al. (2010). For the cases for which the flux uncertainties are not available, we adopt 25% of the measured flux as the uncertainty.

[d] SDSS Petrosian r magnitude.

[e] Interaction classes (IC) are described in Section 3.2. The IC listed in this table are based on combined gri SDSS images; " ··· " entries in the Table indicate the lack of an SDSS image.

[f] References: (1) Veilleux et al. (2002); (2) Hwang et al. (2007); (3) this work.

[g] Superposition of other sources in the field: (A) star; (B) galaxy.

[h] Classifications based on optical spectra. For the sources that are in the SDSS DR10 *emissionlinesPort* catalog (Thomas et al. 2013), we adopt the given BPT classifications: star forming, composite, LINER, and Seyfert. In the case of quasars (QSO), we adopt the "spectrotype" classification from the *galSpecInfo* catalog (see Richards et al. 2002, for the details of SDSS spectroscopic target selection). The classifications marked with a star are based on our BPT classification based on the emission-line fluxes adopted from the SDSS catalog *galSpecLine*[7] (Tremonti et al. 2004; Brinchmann et al. 2004).

Table 2
Known ULIRG Sample

Name AKARI-FIS-V1 (1)	*AKARI* R.A. (J2000) (2)	*AKARI* Decl. (J2000) (3)	Other Name (4)	z[a] (5)	$\log(L_{\rm IR}/L_{\odot})$[b] (6)	F(65 μm)[c] (Jy) (7)	F(90 μm)[c] (Jy) (8)	F(140 μm)[c] (Jy) (9)	F(160 μm)[c] (Jy) (10)	r[d] (mag) (11)	IC[e] (12)	IC[f] Ref. (13)	Note[g] (14)	Spectral[h] Class (15)
J0857064+190855	08 57 06.37	+19 08 55.4	SDSS J085706.35+190853.5	0.331	$12.92^{+0.01}_{-0.05}$	...	0.48 ± 0.06	...	2.56 ± 0.10	15.79	NI	3	...	QSO
J1022125+241208	10 22 12.46	+24 12 07.8	SDSS J102212.64+241202.4	0.188	$12.01^{+0.22}_{-0.08}$	...	0.59 ± 0.03	0.90 ± 2.81	...	15.80	IV	3	...	LINER
J1422313+260205	14 22 31.27	+26 02 05.2	SDSS J142231.37+260205.1	0.159	$12.20^{+0.11}_{-0.05}$	0.96 ± 0.24	1.36 ± 0.04	2.29 ± 0.43	...	13.59	IIIa	1	...	Star forming
J1231216+275524	12 31 21.57	+27 55 24.4	SDSS J123121.37+275524.0	0.212	$12.33^{+0.01}_{-0.09}$	0.52 ± 0.13	0.40 ± 0.10	1.41 ± 0.35	1.93 ± 0.48	17.35	IV	3	...	Composite
J1251200+021900	12 51 20.03	+02 19 00.2	SDSS J125120.04+021902.4	0.253	$12.48^{+0.04}_{-0.02}$	1.00 ± 0.25	0.73 ± 0.04	1.86 ± 0.09	0.81 ± 0.20	15.00	V	2	...	Composite
J0030089−002743	00 30 08.95	−00 27 43.5	SDSS J003009.08−002744.2	0.242*	$12.46^{+0.03}_{-0.03}$	0.37 ± 0.09	0.62 ± 0.06	1.34 ± 0.30	0.40 ± 0.10	14.56	IIIb	3	...	...
J0914140+032200	09 14 14.01	+03 22 00.4	SDSS J091413.79+032201.4	0.145	$12.07^{+0.06}_{-0.03}$	1.11 ± 0.28	1.39 ± 0.11	2.29 ± 0.51	0.86 ± 0.21	14.48	IIIa	1	...	LINER
J1105377+311432	11 05 37.71	+31 14 32.3	SDSS J110537.54+311432.2	0.199	$12.20^{+0.05}_{-0.02}$	0.71 ± 0.18	0.98 ± 0.06	1.31 ± 0.33	0.59 ± 0.15	16.03	IV	1	...	Composite
J0323227−075612	03 23 22.75	−07 56 12.1	SDSS J032322.87−075615.3	0.166	$12.14^{+0.11}_{-0.06}$	0.50 ± 0.12	0.91 ± 0.00	1.80 ± 0.25	...	12.99	IV	1	...	Composite
J1632212+155145	16 32 21.24	+15 51 44.8	SDSS J163221.38+155145.5	0.242	$12.67^{+0.02}_{-0.04}$	1.50 ± 0.13	1.46 ± 0.03	2.42 ± 0.48	2.75 ± 0.06	14.27	V	1	...	Composite
J0148531+002857	01 48 53.10	+00 28 57.1	SDSS J014852.57+002859.8	0.280	$12.30^{+0.26}_{-0.04}$	0.70 ± 0.17	0.48 ± 0.05	0.94 ± 0.39	...	15.49	IIIa	2	...	Composite
J0159503+002340	01 59 50.28	+00 23 39.9	SDSS J015950.25+002340.9	0.163	$12.43^{+0.01}_{-0.04}$	2.01 ± 0.03	1.82 ± 0.17	2.94 ± 0.18	0.16 ± 0.04	15.63	IV	1	...	QSO
J1353317+042809	13 53 31.72	+04 28 08.8	SDSS J135331.57+042805.3	0.136*	$12.44^{+0.01}_{-0.05}$	1.26 ± 0.31	1.62 ± 0.05	0.23 ± 0.06	1.61 ± 0.40	12.67	IV	1	B	...
J0244173−003040	02 44 17.35	−00 30 40.3	SDSS J024417.44−003041.1	0.200	$12.07^{+0.01}_{-0.05}$	0.36 ± 0.09	0.65 ± 0.19	0.77 ± 0.19	0.86 ± 0.22	15.08	IIIa,G	2	...	QSO
J1202268−012918	12 02 26.81	−01 29 18.0	SDSS J120226.76−012915.3	0.150	$12.36^{+0.05}_{-0.01}$	1.94 ± 0.39	2.54 ± 0.20	3.09 ± 0.67	1.06 ± 1.26	15.68	IV,G	3	...	Star forming*
J1013477+465402	10 13 47.75	+46 54 02.1	SDSS J101348.09+465359.6	0.206	$12.24^{+0.09}_{-0.05}$	0.13 ± 0.03	0.72 ± 0.05	...	...	16.78	IV	3	...	Seyfert
J0858418+104124	08 58 41.77	+10 41 24.3	SDSS J085841.77+104122.1	0.148	$12.17^{+0.05}_{-0.03}$	1.00 ± 0.25	1.55 ± 0.13	2.09 ± 0.38	2.62 ± 0.94	16.17	IV,G	1	...	Seyfert
J1347336+121727	13 47 33.58	+12 17 27.4	SDSS J134733.36+121724.3	0.120	$12.18^{+0.03}_{-0.03}$	1.90 ± 0.47	1.75 ± 0.08	0.96 ± 0.24	0.97 ± 0.24	14.13	IIIb	1	...	Seyfert*
J0853252+252646	08 53 25.21	+25 26 45.6	SDSS J085325.07+252656.0	0.256	$12.37^{+0.09}_{-0.08}$	0.56 ± 0.14	0.68 ± 0.06	0.68 ± 4.39	1.28 ± 0.32	11.72	V	3	B	QSO
J0825215+383306	08 25 21.47	+38 33 05.7	SDSS J082521.65+383258.5	0.206	$12.28^{+0.10}_{-0.08}$	0.26 ± 0.06	0.59 ± 0.01	1.49 ± 0.37	...	16.03	IIIb	2	...	Composite
J0829512+384528	08 29 51.18	+38 45 27.8	SDSS J082951.39+384523.7	0.195	$12.02^{+0.11}_{-0.07}$	0.33 ± 0.08	0.53 ± 0.09	0.89 ± 0.22	...	13.34	IIIb	2	...	Composite
J1142035+005135	11 42 03.51	+00 51 35.5	SDSS J114203.41+005135.8	0.245	$12.10^{+0.04}_{-0.04}$	0.37 ± 0.09	0.45 ± 0.05	0.15 ± 0.04	0.67 ± 0.17	15.26	IV	2	...	Composite
J0810595+281354	08 10 59.51	+28 13 54.1	SDSS J081059.61+281352.2	0.336	$12.65^{+0.18}_{-0.14}$	...	0.63 ± 0.01	1.10 ± 0.28	...	15.40	IIIb	2	...	Composite
J0900252+390400	09 00 25.21	+39 03 59.8	SDSS J090025.37+390353.7	0.058	$12.03^{+0.01}_{-0.04}$	5.93 ± 0.70	5.13 ± 0.19	2.62 ± 0.91	1.43 ± 0.36	15.97	IIIb	1	...	Star forming
J0830197+192040	08 30 19.74	+19 20 40.0	SDSS J083019.75+192050.0	0.186	$12.03^{+0.12}_{-0.07}$	0.49 ± 0.12	0.59 ± 0.07	...	1.30 ± 0.33	15.02	IIIb	3	...	Star forming
J1121293+112233	11 21 29.25	+11 22 33.3	SDSS J112129.00+112225.7	0.185	$12.32^{+0.04}_{-0.03}$	0.83 ± 0.21	1.07 ± 0.03	2.16 ± 0.11	...	13.37	IIIa	2	...	Seyfert
J1006038+411223	10 06 03.83	+41 12 23.4	SDSS J100603.85+411224.8	0.328	$12.42^{+0.03}_{-0.05}$	0.28 ± 0.07	0.54 ± 0.03	0.47 ± 0.12	...	15.36	V	2	...	Star forming
J0838034+505516	08 38 03.36	+50 55 16.5	SDSS J083803.61+505508.9	0.097	$12.03^{+0.01}_{-0.04}$	2.31 ± 0.04	2.00 ± 0.08	2.62 ± 0.40	...	17.30	IV	2	...	Composite
J0902489+523623	09 02 48.87	+52 36 22.6	SDSS J090248.90+523624.7	0.157	$12.05^{+0.01}_{-0.06}$	1.20 ± 0.30	0.87 ± 0.04	0.25 ± 0.06	1.56 ± 0.39	15.72	V	1	...	Composite
J0847504+232113	08 47 50.37	+23 21 12.8	SDSS J084750.26+232110.9	0.152	$12.01^{+0.09}_{-0.08}$	...	0.75 ± 0.06	1.66 ± 0.39	...	13.62	IIIb	3	...	Star forming
J1559301+380843	15 59 30.13	+38 08 42.7	SDSS J155930.40+380838.8	0.218	$12.19^{+0.02}_{-0.04}$	0.07 ± 0.02	0.58 ± 0.06	1.36 ± 0.14	2.17 ± 0.38	13.85	IV	2	...	Seyfert
J1324197+053705	13 24 19.74	+05 37 05.4	SDSS J132419.89+053704.7	0.203	$12.66^{+0.02}_{-0.04}$	1.22 ± 0.30	0.89 ± 0.08	...	...	14.68	V	1	...	QSO
J1102140+380240	11 02 14.02	+38 02 40.0	SDSS J110214.00+380234.6	0.158	$12.15^{+0.06}_{-0.01}$	1.12 ± 0.28	1.32 ± 0.03	2.36 ± 0.70	0.46 ± 0.20	15.27	IIIb	1	...	Composite
J1204244+192509	12 04 24.41	+19 25 08.9	SDSS J120424.54+192509.8	0.168	$12.15^{+0.02}_{-0.04}$	1.62 ± 0.41	1.24 ± 0.03	1.19 ± 0.04	0.79 ± 0.20	15.38	IV	1	...	Composite
J1108513+065915	11 08 51.31	+06 59 15.1	SDSS J110851.03+065901.5	0.182	$12.07^{+0.09}_{-0.11}$	0.30 ± 0.07	0.52 ± 0.05	0.29 ± 4.55	1.68 ± 0.42	15.64	IIIa	3	B	QSO
J1040290+105325	10 40 29.05	+10 53 25.3	SDSS J104029.17+105318.3	0.136	$12.26^{+0.06}_{-0.03}$	2.02 ± 0.50	2.13 ± 0.13	1.46 ± 2.03	0.75 ± 0.19	14.73	IV	1	...	LINER
J1207210+021702	12 07 21.03	+02 17 01.7	SDSS J120721.45+021657.8	0.222	$12.09^{+0.04}_{-0.04}$	1.32 ± 0.33	0.58 ± 0.02	0.54 ± 0.13	0.81 ± 0.20	14.36	V	2	...	Composite
J1255482−033908	12 55 48.19	−03 39 08.2	SDSS J125547.83−033909.6	0.169	$12.06^{+0.13}_{-0.08}$	...	0.73 ± 0.02	...	1.66 ± 0.41	15.53	IV	2	A	QSO
J0906339+045136	09 06 33.93	+04 51 35.5	SDSS J090634.03+045127.6	0.125	$12.02^{+0.06}_{-0.04}$	1.62 ± 0.40	1.64 ± 0.07	2.94 ± 1.55	2.43 ± 0.61	13.68	IV	1	...	Composite
J1153144+131432	11 53 14.39	+13 14 32.1	SDSS J115314.23+131427.9	0.127	$12.26^{+0.05}_{-0.02}$	2.37 ± 0.16	2.57 ± 0.14	2.76 ± 0.55	1.03 ± 1.03	13.50	IV	1	...	Composite

Table 2
(Continued)

Name AKARI-FIS-V1 (1)	*AKARI* R.A. (J2000) (2)	*AKARI* Decl. (J2000) (3)	Other Name (4)	z[a] (5)	$\log(L_{\rm IR}/L_\odot)$[b] (6)	F(65 μm)[c] (Jy) (7)	F(90 μm)[c] (Jy) (8)	F(140 μm)[c] (Jy) (9)	F(160 μm)[c] (Jy) (10)	r[d] (mag) (11)	IC[e] (12)	IC[f] Ref. (13)	Note[g] (14)	Spectral[h] Class (15)
J1202054+112813	12 02 05.41	+11 28 13.2	SDSS J120205.59+112812.2	0.194	$12.19^{+0.05}_{-0.03}$	0.07 ± 0.02	1.03 ± 0.03	···	0.87 ± 0.22	14.85	IIIa	2	A	Star forming
J1006432+091726	10 06 43.16	+09 17 26.3	SDSS J100643.50+091727.5	0.171	$12.10^{+0.07}_{-0.01}$	0.79 ± 0.20	1.02 ± 0.08	1.22 ± 0.30	0.42 ± 0.10	13.72	IIIb	2	···	Composite
J1052232+440849	10 52 23.24	+44 08 48.6	SDSS J105223.52+440847.6	0.092	$12.06^{+0.03}_{-0.03}$	3.39 ± 0.27	3.53 ± 0.12	4.11 ± 0.37	2.96 ± 1.01	15.33	IV	1	···	Composite
J1254008+101115	12 54 00.82	+10 11 14.6	SDSS J125400.80+101112.4	0.319	$12.58^{+0.03}_{-0.05}$	0.69 ± 0.17	0.79 ± 0.05	···	0.99 ± 0.25	12.99	V	3	···	QSO
J1348397+581854	13 48 39.66	+58 18 54.1	SDSS J134840.08+581852.0	0.158	$12.12^{+0.03}_{-0.04}$	0.53 ± 0.13	1.36 ± 0.03	0.93 ± 0.23	1.26 ± 0.63	15.08	IIIb	1	···	Composite
J1015153+272717	10 15 15.33	+27 27 17.1	SDSS J101515.35+272717.1	0.210	$12.09^{+0.03}_{-0.04}$	0.84 ± 0.21	0.64 ± 0.02	0.86 ± 0.21	0.74 ± 0.18	13.88	V	3	···	Composite
J1356100+290538	13 56 09.98	+29 05 38.0	SDSS J135609.99+290535.1	0.109	$12.04^{+0.02}_{-0.05}$	1.70 ± 0.43	1.78 ± 0.05	2.72 ± 0.56	0.26 ± 0.07	14.21	IIIb	1	···	Composite
J1502320+142132	15 02 31.95	+14 21 32.4	SDSS J150231.96+142135.3	0.162	$12.12^{+0.04}_{-0.03}$	0.26 ± 0.06	1.69 ± 0.08	2.37 ± 0.28	0.77 ± 0.19	15.15	Tp1	1	···	Composite
J1336237+391733	13 36 23.74	+39 17 32.5	SDSS J133624.06+391731.1	0.179	$12.37^{+0.06}_{-0.06}$	1.38 ± 0.34	1.03 ± 0.06	2.58 ± 0.36	2.74 ± 1.36	16.01	IV,G	1	···	QSO
J1141215+405951	11 41 21.52	+40 59 51.3	SDSS J114122.03+405950.3	0.149	$12.01^{+0.18}_{-0.04}$	0.58 ± 0.14	1.08 ± 0.05	1.57 ± 0.61	···	15.66	V	1	···	Composite
J1433271+281157	14 33 27.14	+28 11 57.0	SDSS J143327.52+281159.9	0.175	$12.12^{+0.16}_{-0.07}$	0.46 ± 0.11	0.83 ± 0.05	1.64 ± 0.41	···	13.94	IIIb	3	···	Seyfert
J1450544+350835	14 50 54.40	+35 08 34.7	SDSS J145054.16+350837.9	0.206	$12.34^{+0.11}_{-0.14}$	0.34 ± 0.08	0.72 ± 0.07	1.81 ± 0.90	···	14.35	V	3	···	Composite
J1406380+010258	14 06 37.97	+01 02 58.1	SDSS J140638.20+010254.6	0.236	$12.35^{+0.01}_{-0.05}$	0.99 ± 0.25	0.74 ± 0.09	0.18 ± 0.05	···	16.03	IV	2	···	Composite
J1522382+333135	15 22 38.17	+33 31 35.4	SDSS J152238.10+333135.9	0.125	$12.03^{+0.01}_{-0.05}$	0.91 ± 0.23	1.26 ± 0.04	1.22 ± 0.25	···	17.23	IV	1	···	Composite⋆
J1505390+574305	15 05 39.04	+57 43 04.6	SDSS J150539.55+574307.1	0.151	$12.02^{+0.02}_{-0.08}$	1.14 ± 0.28	0.87 ± 0.05	1.61 ± 0.97	0.73 ± 2.51	14.70	IIIb	1	···	Star forming
J1441041+532011	14 41 04.11	+53 20 10.8	SDSS J144104.38+532008.7	0.105	$12.03^{+0.01}_{-0.04}$	2.03 ± 0.45	1.78 ± 0.13	1.77 ± 0.41	0.91 ± 2.13	16.49	Tp1	1	···	LINER⋆
J1706529+382010	17 06 52.87	+38 20 09.9	SDSS J170653.27+382007.1	0.168	$12.15^{+0.02}_{-0.04}$	0.79 ± 0.20	0.96 ± 0.02	1.68 ± 0.75	0.19 ± 0.05	15.16	IIIa,G	2	A	LINER
J1649140+342510	16 49 14.01	+34 25 09.8	SDSS J164914.09+342513.2	0.113	$12.07^{+0.08}_{-0.01}$	2.28 ± 0.36	2.24 ± 0.08	2.69 ± 0.95	1.96 ± 3.66	15.55	IIIb	1	···	Star forming
J0823127+275140	08 23 12.66	+27 51 39.6	SDSS J082312.61+275139.8	0.168	$12.07^{+0.03}_{-0.03}$	0.53 ± 0.13	1.04 ± 0.02	0.96 ± 0.24	1.26 ± 0.32	18.30	IV	1	···	Star forming
J1213460+024844	12 13 45.99	+02 48 43.8	SDSS J121346.11+024841.5	0.073	$12.25^{+0.03}_{-0.03}$	7.10 ± 0.51	8.69 ± 0.31	6.17 ± 0.36	3.90 ± 1.32	15.42	IIIb	1	···	Composite
J1346511+074720	13 46 51.09	+07 47 20.0	SDSS J134651.09+074719.0	0.135	$12.09^{+0.06}_{-0.02}$	1.71 ± 0.43	1.49 ± 0.10	2.25 ± 0.86	0.61 ± 0.15	16.68	Tp1,G	1	···	Composite
J2257246−262120	22 57 24.65	−26 21 20.5	TGS123Z162	0.164	$12.16^{+0.05}_{-0.06}$	1.27 ± 0.32	1.17 ± 0.17	1.53 ± 1.17	1.68 ± 0.11	15.22	IIIa	2	···	···
J2223286−270006	22 23 28.57	−27 00 05.7	TGS178Z172	0.131	$12.19^{+0.05}_{-0.02}$	1.87 ± 0.08	1.90 ± 0.09	2.90 ± 0.87	1.06 ± 0.26	12.70	IIIb	1	···	···
J1132417−053940	11 32 41.68	−05 39 40.2	TGN111Z322	0.230	$12.18^{+0.07}_{-0.05}$	0.44 ± 0.11	0.64 ± 0.02	0.81 ± 0.20	···	14.46	IV	2	···	···
J0238167−322036	02 38 16.66	−32 20 36.3	TGS465Z105	0.198	$12.31^{+0.02}_{-0.03}$	1.08 ± 0.27	0.95 ± 0.11	1.66 ± 0.10	2.33 ± 0.58	13.90	V	2	···	···
J0238126−473813	02 38 12.64	−47 38 12.9	TGS875Z072	0.098	$12.07^{+0.02}_{-0.03}$	2.76 ± 0.32	3.24 ± 0.09	3.99 ± 0.42	2.34 ± 0.66	14.53	V	2	···	···
J0237297−461544	02 37 29.66	−46 15 44.4	TGS875Z471	0.206	$12.37^{+0.06}_{-0.06}$	0.90 ± 0.56	1.13 ± 0.07	1.04 ± 1.04	1.99 ± 0.50	15.94	V	2	···	···
J0048064−284820	00 48 06.37	−28 48 20.0	TGS288Z046	0.110	$12.12^{+0.04}_{-0.02}$	2.56 ± 0.64	2.48 ± 0.16	4.08 ± 0.36	···	16.85	IIIa	1	···	···
J0112165−273819	01 12 16.49	−27 38 18.8	TGS213Z002	0.222	$12.37^{+0.01}_{-0.24}$	0.43 ± 0.11	0.45 ± 0.04	0.83 ± 0.99	1.79 ± 0.45	15.05	IIIa	2	···	···
J0138061−324519	01 38 06.14	−32 45 18.6	TGS509Z038	0.198	$12.12^{+0.08}_{-0.02}$	1.23 ± 0.31	0.75 ± 0.07	0.89 ± 0.22	0.40 ± 0.10	16.99	V	2	···	···
J0302108−270725	03 02 10.82	−27 07 24.7	TGS238Z241	0.221	$12.42^{+0.06}_{-0.03}$	0.98 ± 0.24	1.22 ± 0.15	1.07 ± 0.27	0.42 ± 0.11	15.98	IV	2	···	···
J0118266−253607	01 18 26.61	−25 36 06.8	TGS147Z020	0.237	$12.12^{+0.04}_{-0.03}$	0.67 ± 0.17	0.54 ± 0.03	0.50 ± 0.13	0.59 ± 0.15	16.32	V	2	···	···
J0152042−285116	01 52 04.20	−28 51 16.5	TGS302Z057	0.184	$12.06^{+0.06}_{-0.04}$	0.46 ± 0.11	0.73 ± 0.06	2.14 ± 0.60	1.02 ± 0.26	15.63	IIIa	2	···	···
J0159138−292436	01 59 13.82	−29 24 36.1	TGS304Z128	0.140	$12.06^{+0.08}_{-0.02}$	2.16 ± 0.40	1.36 ± 0.05	1.61 ± 0.36	0.63 ± 0.16	16.72	IV	1	···	···
J1329391−034654	13 29 39.11	−03 46 53.7	TGN137Z043	0.222	$12.19^{+0.33}_{-0.00}$	0.58 ± 0.14	0.75 ± 0.06	···	2.49 ± 3.85	16.39	IV	2	···	···
J1112034−025414	11 12 03.36	−02 54 13.8	TGN232Z018	0.106	$12.14^{+0.07}_{-0.02}$	2.55 ± 0.39	2.93 ± 0.26	1.47 ± 0.28	···	14.31	IV	1	···	···
J2307212−343838	23 07 21.24	−34 38 38.4	TGS538Z137	0.208	$12.22^{+0.04}_{-0.02}$	0.76 ± 0.19	0.89 ± 0.10	1.43 ± 0.36	0.34 ± 0.59	18.43	V	2	···	···
J2208493−344627	22 08 49.25	−34 46 27.4	TGS528Z076	0.174	$12.21^{+0.05}_{-0.14}$	0.80 ± 0.20	0.67 ± 0.02	1.88 ± 0.45	···	14.93	V	2	···	···

Notes. For a, b, c, d, f, g, and h see the notes in Table 2.
[e] See Section 3.2 for the details of the interaction classes. The IC listed in this table are mostly adopted from the references given in Column 13.

Table 3
New HLIRG

Name AKARI-FIS-V1 (1)	*AKARI* R.A. (J2000) (2)	*AKARI* Decl. (J2000) (3)	Other Name (4)	z^{a} (5)	$\log(L_{IR}/L_{\odot})^{b}$ (6)	$F(65\,\mu m)^{c}$ (Jy) (7)	$F(90\,\mu m)^{c}$ (Jy) (8)	$F(140\,\mu m)^{c}$ (Jy) (9)	$F(160\,\mu m)^{c}$ (Jy) (10)	r^{d} (mag) (11)	IC[e] (12)	IC[f] Ref. (13)	Note[g] (14)	Spectral[h] Class (15)
J1425001+103045	14 25 00.06	+10 30 44.7	SDSS J142500.73+103043.6	0.480	$13.34^{+0.01}_{-0.16}$	0.95 ± 0.24	0.61 ± 0.06	1.97 ± 0.48	1.97 ± 0.49	18.51	V	3	···	Composite

Notes. For a, b, c, d, e, f, g, and h see the notes in Table 2.

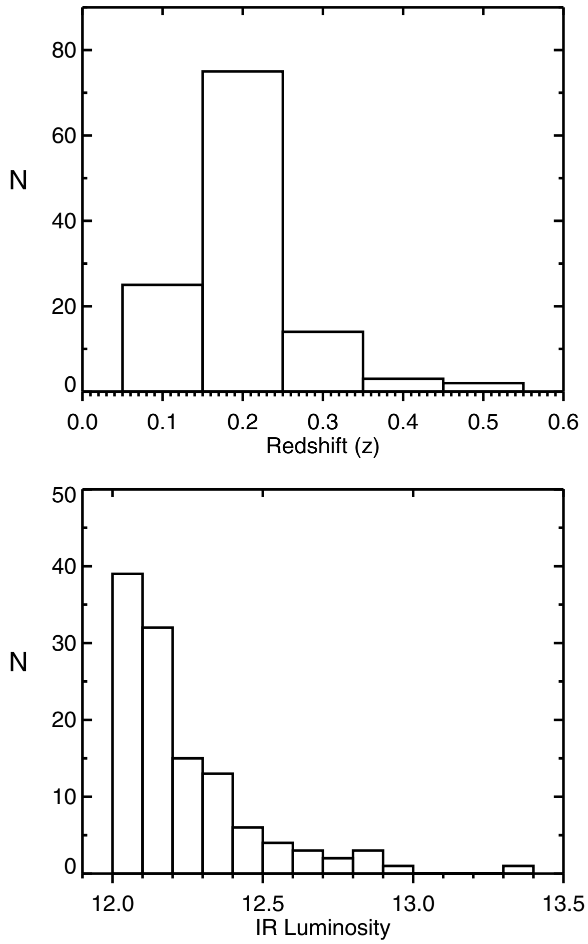

Figure 2. Distributions of redshift (top) and IR luminosity, $\log(L_{IR}/L_{\odot})$, (bottom) for the final (H)ULIRG sample.

3.1.2. FIR Color Properties of Our Sample

The IR emission of the so-called normal star-forming galaxies (that are not dominated by AGN activity) is mostly due to the thermal radiation from dust grains heated by star formation. The "normal" star-forming galaxies detected by *IRAS* showed a clear trend of decreasing 60- to 100-μm flux ratios, $F(60\,\mu m)/F(100\,\mu m)$, with increasing 12- to 25-μm flux ratios, $F(12\,\mu m)/F(25\,\mu m)$, (Helou 1986). This trend is associated with the intensity dependence of IR colors, such that "warm" colors (greater $F(60\,\mu m)/F(100\,\mu m)$ values) are related to active star formation with high IR luminosities (Helou 1986).

Dale et al. (2001) construct single-parameter dust models of normal star-forming galaxies based on the $F(60\,\mu m)/F(100\,\mu m)$ color and the intensity of the interstellar radiation field, U. They characterize the overall IR SED as a power-law distribution of dust mass over U such that $dM(U) \sim U^{-\alpha} dU$, where α is the exponent of the power-law distribution. Dale & Helou (2002) provide 64 SED models for a wide range of U or equivalently *IRAS* $F(60\,\mu m)/F(100\,\mu m)$ color (between -0.54 and 0.21) and α values ($0.0625 \leqslant \alpha \leqslant 4.0$). In Section 2.2 we measured L_{IR} based on these models. In the following, we investigate the *AKARI* color properties of our ULIRG sample and compare the observed colors with the SED models of Dale & Helou (2002).

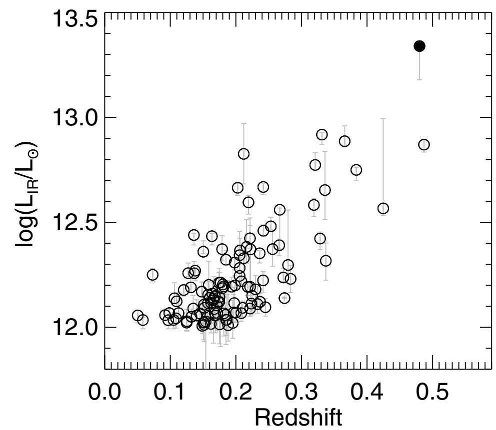

Figure 3. IR luminosity vs. redshift for 118 ULIRGs (open circles) and one HLIRG (filled circle) in the final sample.

For this investigation we use the *AKARI* $F(9\,\mu m)$ and $F(18\,\mu m)$ fluxes from the *AKARI*/IRC all-sky survey point source catalog. The $F(65\,\mu m)$, $F(90\,\mu m)$, $F(140\,\mu m)$, and $F(160\,\mu m)$ fluxes are listed in Tables 1, 2, and 3. Figure 4 presents the observed *AKARI* color–color diagrams: (a) $F(9\,\mu m)/F(18\,\mu m)$ versus $F(18\,\mu m)/F(65\,\mu m)$, (b) $F(18\,\mu m)/F(65\,\mu m)$ versus $F(65\,\mu m)/F(90\,\mu m)$, (c) $F(65\,\mu m)/F(90\,\mu m)$ versus $F(90\,\mu m)/F(140\,\mu m)$, and (d) $F(90\,\mu m)/F(140\,\mu m)$ versus $F(140\,\mu m)/F(160\,\mu m)$. Panels (a) and (b) show only the two sources that are detected in all of the *AKARI* bands. Panels (c) and (d) include 71 sources that are detected in all *AKARI* FIS bands. The different symbols represent the spectral classes as listed in Tables 1, 2, and 3 (see Section 3.3): circle (composite), star (star forming), square (LINER), diamond (Seyfert[12]), triangle (QSOs), plus (unclassified). In Panels (c) and (d) the FIR colors of different classes of galaxies are distributed over the entire color range. Therefore, AGNs or galaxies cannot be distinguished by their FIR colors. However, this is expected because FIR is tracing star-formation activity with low-temperature dust and is not sensitive to AGN activity. It is known that the *IRAS* mid-IR $F(25\,\mu m)/F(60\,\mu m)$ color is an indicator of "warm" dust and an AGN component ($F(25\,\mu m)/F(60\,\mu m) \geqslant 0.2$) (e.g., Sanders et al. 1988a). Unfortunately, the majority of our ULIRG sample is not detected in the mid-IR colors, and therefore we do not have enough data to explore the mid-IR color properties of our sample.

The color–color diagrams in Panels (c) and (d) do not show a clear correlation. It is important to keep in mind that the detection limits of *AKARI* bands affect the shape of the color–color diagrams. The detection limits of the *AKARI* FIS bands are 3.2 Jy, 0.55 Jy, 3.8 Jy, and 7.5 Jy for the

[12] Seyfert galaxies are low-redshift ($z \leqslant 0.1$), less luminous cousins of quasars (e.g., Richards et al. 2002).

Table 4
Unconfirmed ULIRG Candidates

Name AKARI-FIS-V1 (1)	*AKARI* R.A. (J2000) (2)	*AKARI* Decl. (J2000) (3)	Other Name (4)	z[a] (5)	$\log(L_{\rm IR}/L_{\odot})$[b] (6)	F(65 μm)[c] (Jy) (7)	F(90 μm)[c] (Jy) (8)	F(140 μm)[c] (Jy) (9)	F(160 μm)[c] (Jy) (10)	r[d] (mag) (11)	IC[e] (12)	IC[f] Ref. (13)	Note[g] (14)	Spectral[h] Class (15)
J0058034−025406	00 58 03.44	−02 54 05.8	SDSS J005802.70−025401.8	0.267	$12.27^{+0.03}_{-0.43}$	···	0.21 ± 0.05	5.13 ± 1.49	···	14.31	IIIb	3	B ···	···
J1444024+000415	14 44 02.37	+00 04 15.0	SDSS J144402.86+000411.9	0.330	$12.66^{+0.02}_{-0.06}$	0.09 ± 0.02	0.23 ± 0.06	0.96 ± 0.24	3.74 ± 0.32	13.44	IIIa	3	··· ···	···
J0545295−011324	05 45 29.50	−01 13 24.5	SDSS J054529.53−011318.0	0.884	$12.82^{+0.02}_{-0.07}$	0.41 ± 0.10	0.57 ± 0.20	···	0.24 ± 0.06	12.76	NI	3	··· ···	···
J1352265+020815	13 52 26.48	+02 08 14.9	SDSS J135227.76+020816.5	2.853	$13.01^{+0.12}_{-0.06}$	···	0.39 ± 0.07	0.76 ± 0.18	3.28 ± 0.82	15.70	IIIa	3	Large separation ···	···
J1716527+271405	17 16 52.73	+27 14 04.6	SDSS J171653.48+271406.2	0.539	$12.21^{+0.09}_{-0.11}$	···	0.23 ± 0.06	1.97 ± 0.36	0.17 ± 0.04	11.74	V	3	A ···	···

Notes. For a, b, c, d, e, f, g, and h see the notes in Table 2.

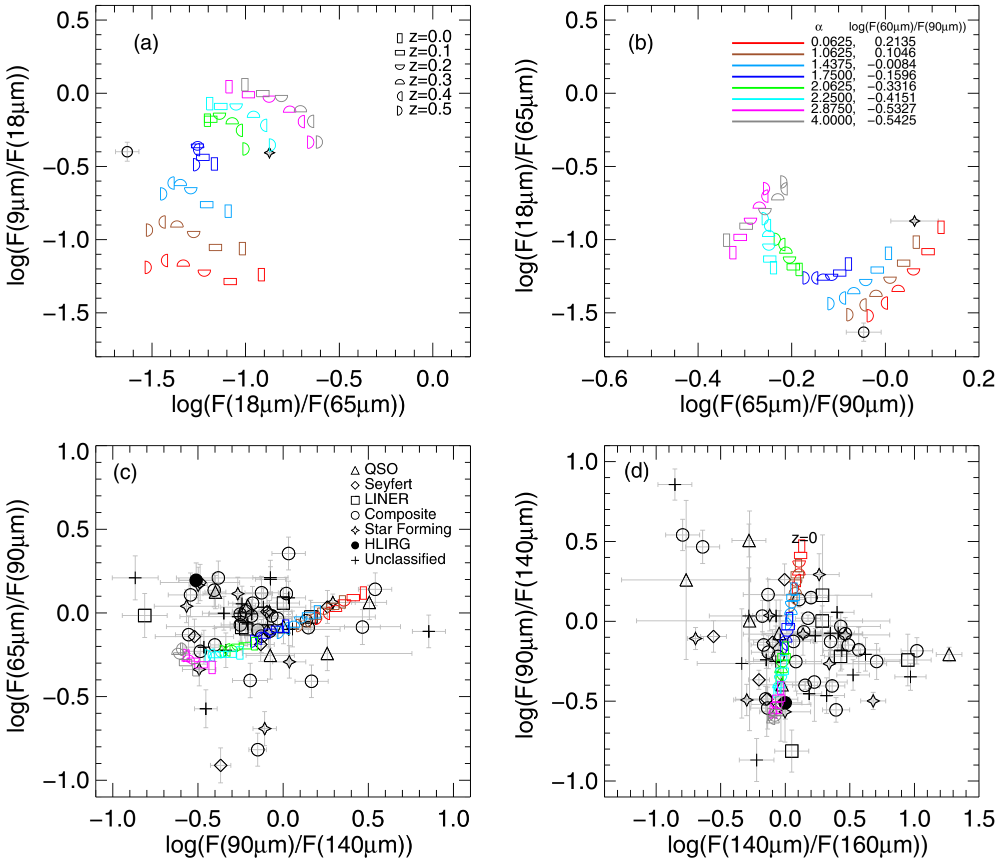

Figure 4. *AKARI* color–color diagrams. The top left (a) and right (b) panels show $\log(F(9\,\mu\text{m})/F(18\,\mu\text{m}))$ vs. $\log(F(18\,\mu\text{m})/F(65\,\mu\text{m}))$ and $\log(F(18\,\mu\text{m})/F(65\,\mu\text{m}))$ vs. $\log(F(65\,\mu\text{m})/F(90\,\mu\text{m}))$ for the two ULIRGs detected in all of the *AKARI* bands. The bottom panels show $\log(F(65\,\mu\text{m})/F(90\,\mu\text{m}))$ vs. $\log(F(90\,\mu\text{m})/F(140\,\mu\text{m}))$ (c) and $\log(F(90\,\mu\text{m})/F(140\,\mu\text{m}))$ vs. $\log(F(140\,\mu\text{m})/F(160\,\mu\text{m}))$ (d) colors for 71 sources that are detected in the *AKARI* 65 μm, 90 μm, 140 μm, and 160 μm bands. The symbol code is given in the legend of panel (c). The colored symbols in each panel indicate the expected colors from the SED templates of Dale & Helou (2002) at redshifts $z = 0.0$, 0.1, 0.2, 0.3, 0.4, and 0.5. The symbol codes for the redshifts are given in the legend of panel (a). We only show the expected colors for eight SED templates. Different colors represent different models; the parameters of the models are given in the legend of panel (b).

65 μm, 90 μm, 140 μm and 160 μm bands (Yamamura et al. 2010), respectively. The WIDE-S filter centered at 90 μm is the broadest, and therefore it has the deepest detection limit compared to other bands. In Panel (d) the distribution of the colors is shaped by the observational detection limits. This is mainly because 140 μm is common in both axes. In the x-axis as the 140 μm flux gets brighter the $\log(F(140\,\mu\text{m})/F(160\,\mu\text{m}))$ color moves toward the right, but at the same time in the y-axis the $\log(F(90\,\mu\text{m})/F(140\,\mu\text{m}))$ color moves downward. This behavior creates a boundary on the top right corner of this diagram. Even if there were an intrinsic color–color correlation in Panel (d), it would be truncated on the upper right corner because of the observational limits. We expect to have a similar detection limit effect in Panel (c) because the 65 μm and 140 μm detection limits are brighter than 90 μm, and this may cause colors to hit the boundaries of 65 μm and 140 μm before the limit of 90 μm.

In Figure 4, the colored symbols in each panel show the expected colors by the IR SED models of Dale & Helou (2002). We choose eight SEDs with different α and $F(60\,\mu\text{m})/F(100\,\mu\text{m})$ values among the 64. The selected models have a sequence in terms of α and $\log(F(60\,\mu\text{m})/F(100\,\mu\text{m}))$: $0.06 \leqslant \alpha \leqslant 4.0$ and $-0.54 \leqslant \log(F(60\,\mu\text{m})/F(100\,\mu\text{m})) \leqslant 0.21$. The expected colors from the selected SEDs are shown with different colors; the α and $\log(F(60\,\mu\text{m})/F(100\,\mu\text{m}))$ parameters of each model are given in the top corner of Panel (b). We show the colors expected from each model as a function of redshift from 0 to 0.5 in order to illustrate the redshift dependence of the colors. The symbol code for $z = 0.0$, 0.1, 0.2, 0.3, 0.4, and 0.5 is given in the legend of Panel (a). In Panels (c) and (d) the data show a large spread around the model colors. In Panel (c), the large vertical and horizontal spreads of $\log(F(65\,\mu\text{m})/F(90\,\mu\text{m}))$ and $\log(F(90\,\mu\text{m})/F(140\,\mu\text{m}))$ colors around the models are mainly due to the limited parameter coverage of the SED models. The models cover the ranges between −0.54–0.21 and −0.62–0.47 in the y- and x-axis, respectively. Therefore, the models do not overlap with the colors exceeding this range. In Panel (d), in particular the $\log(F(140\,\mu\text{m})/F(160\,\mu\text{m}))$ colors have a large scatter around the models; the models cover only the −0.11–0.13 range, but the observed colors can exceed this up to 1.27. We do not see a clear trend in $\log(F(140\,\mu\text{m})/F(160\,\mu\text{m}))$ colors with redshift. Because we show the expected colors for $z = 0.0$–0.5, the observed scatter does not seem to be due to the range in redshift of our sample. We further discuss such outliers in color–color diagrams in Section 4.

Because the *AKARI* $\log(F(65\,\mu\text{m})/F(90\,\mu\text{m}))$ color is equivalent to the *IRAS* $\log(F(60\,\mu\text{m})/F(100\,\mu\text{m}))$ color, it is possible to compare the *AKARI* and *IRAS* color distributions of ULIRGs. Hwang et al. (2007) investigate the *IRAS* colors of 324 ULIRGs and report a $\log(F(60\,\mu\text{m})/F(100\,\mu\text{m}))$ within the −0.80–0.22 range with a mean of −0.19. The ULIRGs in our sample have a slightly larger range, between −0.91–0.36, but

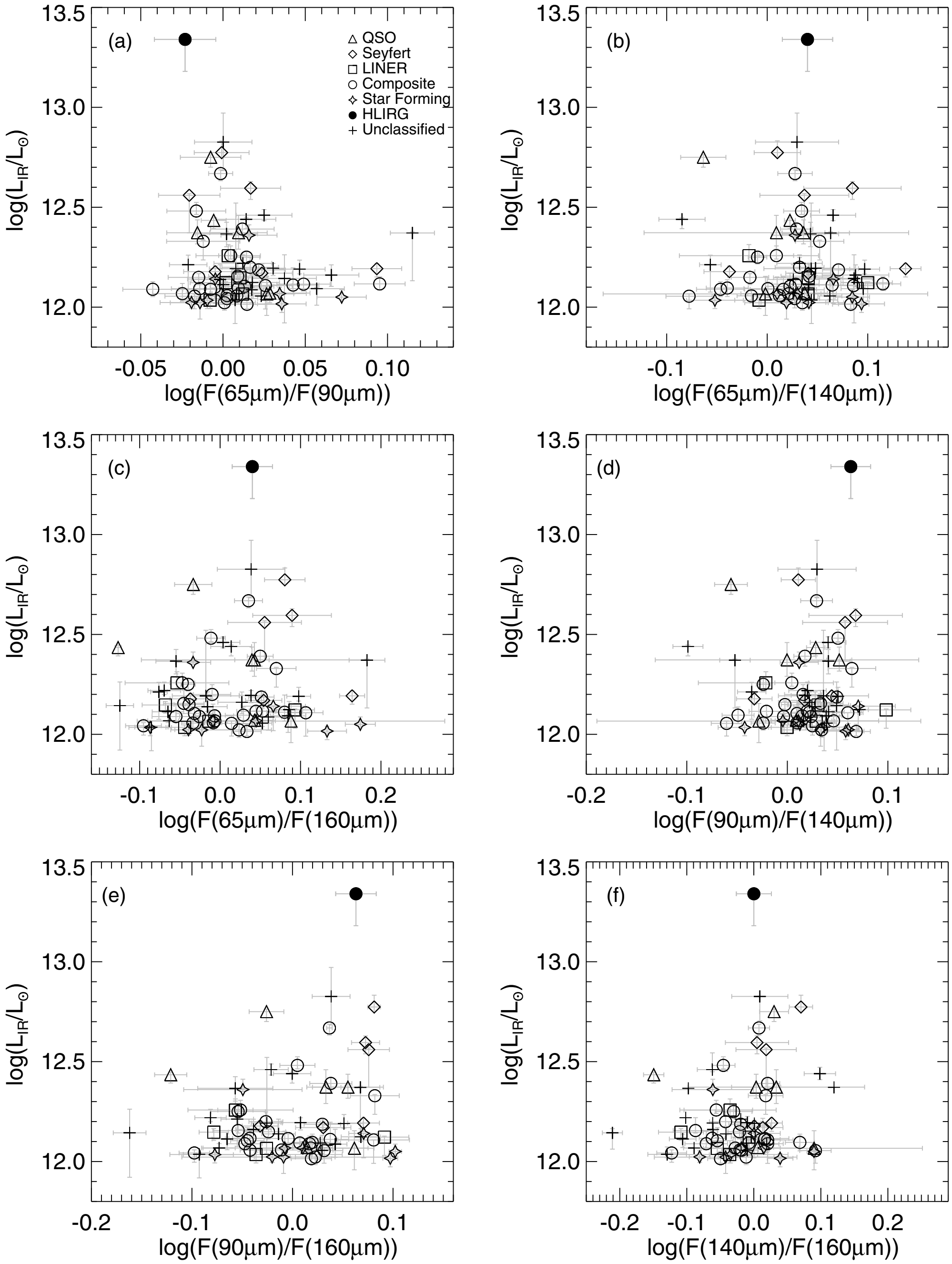

Figure 5. Color–luminosity diagrams of 71 (H)ULIRGs that are detected in all of the *AKARI* FIS bands. The symbol code is given in panel (a).

still the *AKARI* log(F(65 μm)/F(90 μm)) colors overlap with the *IRAS* log(F(60 μm)/F(100 μm)) colors.

3.1.3. FIR Colors versus IR Luminosity

The IR-bright galaxies ($10^{9.5}\ L_\odot \leqslant L_{\rm IR} < 10^{13}\ L_\odot$) studied with *IRAS* show a correlation between the IR colors and the IR luminosity: the log(F(12 μm)/F(25 μm)) color decreases, and the log(F(60 μm)/F(100 μm)) color increases with increasing IR luminosity (Soifer & Neugebauer 1991). As stated in Section 3.1.3, the log(F(60 μm)/F(100 μm)) color is related to the intensity of the radiation field. The SED models of Dale & Helou (2002) cover a wide range of *IRAS* log(F(60 μm)/F(100 μm)) colors that correlate with $L_{\rm IR}$; higher log(F(60 μm)/F(100 μm)) colors indicate higher $L_{\rm IR}$ (Dale & Helou 2002). In the following we investigate the color dependence of the IR luminosities for our (H)ULIRG sample.

Figure 5 presents IR luminosity versus (a) log(F(65 μm)/F(90 μm)), (b) log(F(65 μm)/F(140 μm)), (c) log(F(65 μm)/F(160 μm)), (d) log(F(90 μm)/F(140 μm)), (e) log(F(90 μm)/F(160 μm)), and (f) log(F(140 μm)/F(160 μm)), for 71 sources that are detected in all of the *AKARI* FIS bands. As noted before, because we have only very few sources detected in the 9- and 18-μm bands, we do not include those in this investigation. Because the observed colors change as a function of redshift and luminosity depends on redshift, we apply a k-correction to the *AKARI* FIS colors shown in Figure 5.

As noted before, the *AKARI* log(F(65 μm)/F(90 μm)) color is similar to *IRAS* log(F(60 μm)/F(100 μm)) color, and therefore we would expect a strong correlation in Panel (a). However, none of the *AKARI* colors in Figure 5 show a clear dependence in $L_{\rm IR}$ between $12.0 \leqslant \log(L_{\rm IR}/L_\odot) < 13.3$. Because the $L_{\rm IR}$ range of interest in this study is very narrow compared to the $L_{\rm IR}$ range probed in previous studies (e.g., Soifer & Neugebauer 1991), it is natural not to see the previously discovered significant color–$L_{\rm IR}$correlations. The representative SED models shown in Figure 4 show a luminosity dependence with color, but the observed colors show a large scatter around the models (discussed in Sections 3.1.3 and 4). The large differences between the SED models and the observed colors weaken the color–$L_{\rm IR}$ correlation expectation.

In Figure 5, apart from the color dependence of the IR luminosity, different galaxy types do not show a significant dependence on color.

3.2. Visual Morphologies and Interaction Classes

Morphological studies of local ULIRGs showed that they are mostly interacting galaxies showing tidal features or disturbed morphology (e.g., Farrah et al. 2001; Veilleux et al. 2002, 2006). Surace (1998) introduced an interaction classification scheme based on the evolution sequence that merging galaxies follow in simulations (e.g., Mihos & Hernquist 1996). Such an interaction classification scheme is important in interpreting the morphological properties of ULIRGs in the context of a galaxy evolution triggered by mergers. Veilleux et al. (2002) classified 117 local ULIRGs based on this scheme and showed that ULIRGs are interacting or advanced merger systems.

Here we investigate the morphological properties of our sample with the aim of identifying interaction classes. We use the following widely preferred classification scheme that is described by Veilleux et al. (2002):

1. I: first approach. Separated galaxies with no signs of interaction or merging.
2. II: first contact. Overlapped disks without interaction signs.
3. III: premergers. Two nuclei separated by more than 10 kpc (a; wide binary) or less than 10 kpc (b; close binary), with interaction signs.
4. Tp1: interacting triplet system.
5. IV: merger. One nucleus with prominent tidal features.
6. V: old merger. Disturbed central morphology without clear tidal tail signs.
7. NI: noninteracting. Isolated single galaxy, no signs of disturbed morphology.

Note that we added class NI to represent isolated single galaxies showing no signs of disturbed morphology. Also note that we do not subdivide class IV into two as done by Veilleux et al. (2002) because we do not have *K*-band luminosities.

We (two classifiers: EKE and TG) examined SDSS *g*-*r*-*i* color combined images and classified only the galaxies for which SDSS images are available. For the known ULIRGs, we adopt the interaction classifications from the literature. We prefer to adopt the classifications mainly from Veilleux et al. (2002) and Hwang et al. (2007). The interaction classifications of the galaxies in our sample are given in Column 12 of Tables 1–3. The references for the interaction classes are given in Column 13 of Tables 1–3. In additional to the above interaction classification, we also note whether the galaxies are in a group with (G). We define groups as galaxy systems with more than two members with similar colors. We note that our group definition is subjective, and the group classification given in this work is only for guidance. The SDSS images showing examples of different interaction classes are represented in Figure 1.

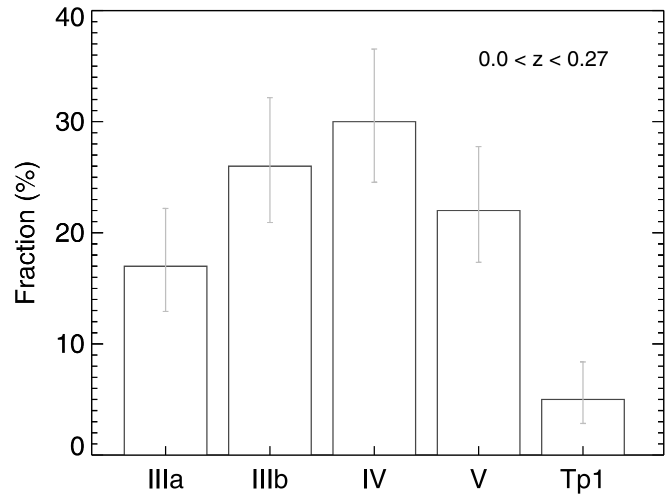

Figure 6. Distribution of the interaction classes for 100 ULIRGs within a $0.0 < z < 0.27$ limit. Interaction classes are described in Section 3.2. The fraction of the late or old mergers that are classified as IV or V is 52%. Error bars represent the 1σ Poisson errors (Gehrels 1986).

As shown in Figure 3, luminosity is correlated with distance, and it becomes more difficult to identify the morphological details for more distant sources. To avoid uncertainties in interaction classifications due to the distances, in the following analysis we focus on a redshift-limited sample of 100 ULIRGs. For comparison purposes, we apply a redshift cut of $z = 0.27$; this is the limit of the Veilleux et al. (2002) ULIRG sample. The distribution of interaction classes of 100 ULIRGs is shown in Figure 6. This figure presents the percentage of different interaction classes. There are no ULIRGs classified as I and II, so they are not in an early interaction phase. The fraction of triplets (Tp1) in our sample is very small (5%). The fraction of binary systems showing strong interaction features (IIIa and IIIb) is 43%. Most of the ULIRGs (52%) are single-nucleus galaxies classified as IV and V, indicating a late- or postmerger phase. Veilleux et al. (2002) study 117 ULIRGs from the *IRAS* 1 Jy sample (Kim et al. 1998) and report 56% of the sample as single-nucleus systems at a late merger stage. The fraction of such systems (IV or V) in our sample is 52%, and this is a result consistent with Veilleux et al. (2002). In our morphology subsample, 35 of the 100 ULIRGs are also part of the sample of 117 ULIRGs studied by Veilleux et al. (2002), and therefore our results can be considered as independent from those derived by Veilleux et al. (2002). We also find 11% of the ULIRGs to be in a group environment.

In Figure 7 we show the fraction of ULIRGs in different interaction classes as a function of IR luminosity. We divide IR luminosities into three bins ($12.0 \leqslant \log(L_{\rm IR}) < 12.25$, $12.25 \leqslant \log(L_{\rm IR}) < 12.5$, and $12.5 \leqslant \log(L_{\rm IR})$); the number of sources in each bin is 73, 22, and 5, respectively. This figure shows a hint of a negative trend for premergers (IIIa and IIIb). The fraction of galaxies classified as IIIa and IIIb decreases from the first bin to the second, but IIIa galaxies increase in the highest $L_{\rm IR}$ bin. The fraction of mergers (IV) increases from the first bin to the second, but it decreases in the third bin. The fraction of old mergers (V) appears to be almost constant with luminosity. The fraction of triplets is constant in the first two bins, but it increases in the third bin. The fraction in the highest luminosity bin is highly uncertain because of the very small

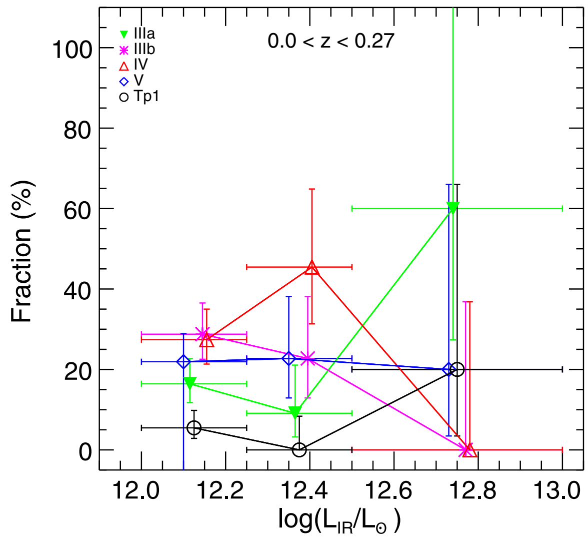

Figure 7. Fraction of interaction classes per IR luminosity for 100 ULIRGs within a $z < 0.27$ limit. The x-axis error bars represent the range of the IR luminosity bins ($12.0 \leqslant L_{\rm IR} < 12.25$, $12.25 \leqslant L_{\rm IR} < 12.5$, $12.5 \leqslant L_{\rm IR} < 13.0$). The y-axis error bars represent the 1σ confidence limits of the Poisson errors on the counts given by Gehrels (1986).

(A color version of this figure is available in the online journal.)

number of sources. Therefore, we consider the trends, including the highest luminosity bin, to be unreliable. If we only take into account the first two luminosity bins, then it is clear that the fraction of premergers has a negative trend and the mergers have a positive trend with increasing luminosity. This is a result consistent with Veilleux et al. (2002), who find a positive trend in the fraction of advanced mergers and IR luminosity.

The morphological properties of our sample confirm that ULIRGs are mostly either in premerger two-galaxy systems or single galaxies in the late or postmerger phase. This is a picture consistent with the general idea that ULIRGs are triggered by strong interactions between galaxies.

3.3. Spectral Classification of Our Sample

The power sources of ULIRGs are high rates of star formation and AGN activity (e.g., Nardini et al. 2010). The traces of the dominant power source can be detected in optical spectra. The properties of the emission lines provide a practical tool for uncovering the source of the ionization producing those lines. To identify the spectral classes of the ULIRGs in our sample, we make use of the available SDSS catalogs providing such a classification. The SDSS spectroscopic pipeline classifies objects as broad-line AGNs/quasars, galaxies, or stars. We adopt this classification to identify the quasars in our sample.

Thomas et al. (2013) investigate the emission line properties of SDSS sources that are already classified as "galaxies" through the pipeline. They apply Baldwin–Phillips–Terlevich (BPT) diagnostics (Baldwin et al. 1981) based on [O III]/Hβ and [N II]/Hα emission line ratios to classify sources into Seyfert, low-ionization nuclear emission region (LINER), SFG, and star-forming/AGN composite. Thomas et al. (2013) use the empirical separation between AGNs and star-forming galaxies according to Kauffmann et al. (2003a), and they use the separation line defined by Schawinski et al. (2007) to select LINERs. We adopt the spectral classification given by Thomas et al. (2013) for the ULIRGs included in their galaxy sample. Some of the ULIRGs in our sample are not included in the

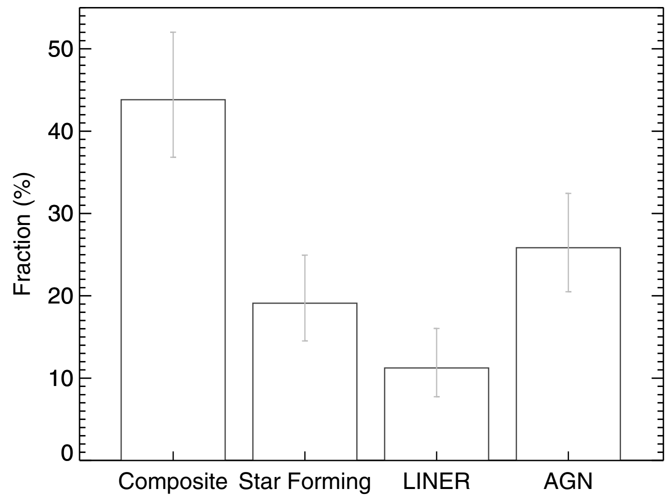

Figure 8. Distribution of spectral classes of 89 ULIRGs for which the SDSS spectra are available. Error bars represent the same quantity as in Figure 6.

sample of Thomas et al. (2013). These are mostly AGNs, but a few sources are classified as broad-line AGN starbursts by the spectroscopic pipeline. To classify such sources, we adopt the available line flux measurements in the SDSS database (see the footnotes of Table 1 for the SDSS references) and use a similar line diagnostic diagram as described by Thomas et al. (2013). The spectral classes are listed in Column 15 of Tables 1–3. The spectral classes marked with a star were obtained in this work.

The distribution of the spectral classes is shown in Figure 8; it represents only 89 source ULIRGs for which SDSS spectra are available. The fraction of purely star-forming galaxies is 19%. The fraction of composite galaxies in our sample is 44%. The fraction of LINERs in our sample is 11%. The LINERs are thought to be powered by AGNs (e.g., Nagar et al. 2005); however, other power sources can also produce LINER-like emission (e.g., Maoz et al. 1998; Sarzi et al. 2010). Because there is a debate whether LINERs are low-luminosity AGNs or a separate class of objects, to be conservative in this work we separate LINERs from AGNs. The fraction of AGN (QSOs and Seyferts) ULIRGs in our sample is 26%.

Most of the ULIRGs in our sample are classified as composite galaxies. It is important to note that these are SFGs, possibly with a hidden AGN component. To be conservative, we do not include composites to AGNs. Because both LINERs and composites may harbor an AGN, the given AGN fraction is only a lower limit.

Figure 9 shows the fraction of ULIRGs in different spectral classes as a function of IR luminosity. We use the same $L_{\rm IR}$ bins as in Figure 7. Each bin include 61 ($12.0 \leqslant \log(L_{\rm IR}) < 12.25$), 18 ($12.25 \leqslant \log(L_{\rm IR}) < 12.5$), and 10 ($12.5 \leqslant \log(L_{\rm IR})$) sources. The fraction of AGNs grows with increasing $L_{\rm IR}$. Star-forming galaxies show an opposite trend: their fraction decreases with increasing $L_{\rm IR}$. This is consistent with the results of previous studies, which showed that the fraction of AGNs in IR galaxies increases with higher IR luminosity (Veilleux et al. 1995; Kim et al. 1998; Goto 2005). The LINERs tend to be constant in each luminosity bin. Composites also tend to be almost constant in the first two bins, but they show a dramatic decrease in the highest luminosity bin. Again, because the LINERs and composites may have an AGN contribution that is hidden in the optical wavelengths, the AGN fractions in each luminosity bin represent the lower limit. However, the trends seen in Figure 9 still agree

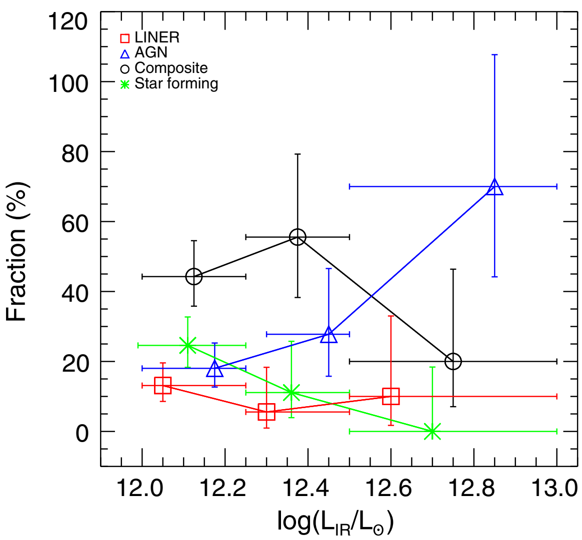

Figure 9. Spectral class fraction per IR luminosity bins for 89 ULIRGs. See the caption of Figure 7 for the error bars.

(A color version of this figure is available in the online journal.)

with the known correlation between the AGN fraction and IR luminosity. Some 28 of the 89 ULIRGs in our optical spectral type subsample are also part of the 1 Jy sample of Veilleux et al. (1995, 1999a). Because ∼31% is a small fraction, our results are mostly independent of those derived for the 1 Jy sample.

3.4. Stellar Masses, Star-formation Rates, Metallicities, and Optical Colors of ULIRGs

The ULIRGs are very special galaxies that are selected according to their enormous IR luminosity, which means a rich dust content. Dust has an important role in galaxy growth and evolution because it is directly linked to star formation and metals in the interstellar medium (ISM). The interplay between the dust and stellar content with the star-formation rate (SFR) controls the galaxy evolution. For normal SFGs, this is evident from the observed correlations between these parameters. Stellar mass ($M_{\rm star}$) and SFR tightly correlate within a $0 < z < 3$ range, and normal star-forming galaxies lie on the so-called main sequence (e.g., Noeske et al. 2007; Elbaz et al. 2007; Santini et al. 2009; Rodighiero et al. 2011; Tadaki et al. 2013). Stellar mass also strongly correlates with the metallicity (Z): massive galaxies show a higher metallicity than the less massive systems. The $M_{\rm star}$–Z relationship is confirmed for normal star-forming galaxies in the local universe ($z \sim 0.15$) (Tremonti et al. 2004). Although there is not a strong relation between SFR and Z, metallicity is a function of SFR and $M_{\rm star}$ in the $M_{\rm star}$–Z–SFR plane (Lara-López et al. 2010; Mannucci et al. 2010). Recently, Santini et al. (2014) showed that there is a tight correlation between the dust mass and SFR, and they introduce a fundamental relation between gas fraction, $M_{\rm star}$, and SFR. These relationships provide a basis for understanding the evolution of normal SFGs. The ULIRGs do not belong to this galaxy category, and in order to explore their place in galaxy evolution, we need to compare them with normal star-forming galaxies. In the following, we investigate the position of ULIRGs in $M_{\rm star}$– SFR, $M_{\rm star}$–Z relationships and in the color–magnitude diagram (CMD). Below we briefly outline the SDSS data used in this investigation.

The available SDSS photometric and spectral data allow us to obtain stellar masses, metallicities, and optical colors of ULIRGs in our sample. The SDSS DR10 (see Ahn et al. 2014) provides stellar masses, emission-line fluxes, stellar and gas kinematics, and velocity dispersion derived spectra of galaxies observed by the BOSS. Following the spectroscopic pipeline (Bolton et al. 2012), the objects classified as a galaxy with a reliable redshift are studied by several groups. "The Portsmouth" group derives photometric stellar mass estimates (Maraston et al. 2013) and measure emission-line fluxes (Thomas et al. 2013).

Maraston et al. (2013) estimate stellar masses through SED fitting of stellar population models to u, g, r, i, and z magnitudes. They use both passive (Maraston et al. 2009) and star-forming templates (Maraston 2005) with Salpeter (1955) and Kroupa (2001) initial mass functions (IMF). Maraston et al. (2013) use the fixed BOSS spectroscopic redshift values and do not include internal galaxy reddening in the SED fitting procedure. The Wisconsin group also derives stellar masses via full spectral fitting (Chen et al. 2012). They use models based on stellar population models of Bruzual & Charlot (2003) with a Kroupa (2001) IMF. Chen et al. (2012) and Maraston et al. (2013) use different stellar population models based on different galaxy star-formation histories, reddening, and IMF assumptions. The stellar masses given by Maraston et al. (2013) are ∼0.2 dex smaller than the masses estimated by Chen et al. (2012), and for high signal-to-noise spectra, the results from both of the methods agree well (Chen et al. 2012). Because spectral data quality is an issue, in this work we prefer to adopt the stellar masses given by Maraston et al. (2013); however, this preference does not change the results of this work. Maraston et al. (2013) obtain stellar masses for active and passive stellar population models. Because ULIRGs are actively SFGs, we adopt the stellar masses from the stellarMassPortStarforming[13] catalog. These are listed in Table 5. The magnitudes used in the stellar mass estimates include contributions from star formation but also possible AGN contamination. The errors associated with the stellar masses are discussed in Section 4.5.

Thomas et al. (2013) fit stellar population synthesis models of Maraston & Strömbäck (2011) and Gaussian emission-line templates to the spectra by using the Gas and Absorption Line Fitting (GANDALF) code of Sarzi et al. (2006). This code accounts for the diffuse dust on the spectral shape according to the Calzetti (2001) obscuration curve. Thomas et al. (2013) correct for the diffuse dust extinction and provide dereddened emission-line fluxes (this includes Galactic extinction). In the following analysis we adopt the emission-line fluxes from the SDSS emissionlinesPort'[3]catalog.

3.4.1. Star-formation Rate and Stellar Mass

The IR luminosity measured from the SEDs (Section 2.2) between 8 μm–1000 μm is the obscured emission from young stars that is re-emitted by dust, so it can be converted to SFR. We use Equation (4) given by Kennicutt (1998) to estimate the SFR based on $L_{\rm IR}$, SFR(IR). This conversion assumes a Salpeter (1955) IMF and that $L_{\rm IR}$ is generated by recent star formation and re-emitted by dust. Even in the case of AGN we expect this assumption to still be valid to infer SFR(IR) because ULIRGs on average have an AGN contribution from 5.0% to 40.0% AGN (e.g., Genzel et al. 1998; Veilleux et al. 2009), but they are mostly powered by star formation. Therefore we note that the SFR(IR) values of the AGN, LINERS, and composites may have on average ∼40.0% AGN contamination and may be

[13] http://www.sdss3.org/dr10/spectro/galaxy_portsmouth.php

Table 5
Stellar Masses, Star-formation Rates, Oxygen Abundances, Optical Colors, and Absolute Magnitudes

AKARI-FIS-V1 Name (1)	*IRAS* Name (2)	$\log(M_{\rm star}(M_{\odot}))$ (3)	SFR(IR) ($M_{\odot}$ yr^{-1}) (4)	SFR(Hα) ($M_{\odot}$ yr^{-1}) (5)	12+log(O/H) (6)	$u^{0.1}-r^{0.1}$ (mag) (7)	$M_r^{0.1}$ (mag) (8)
J2216028+005813	F22134+0043	···	1153^{463}_{320}	···	···	···	
J0859229+473612	F08559+4748	$10.74^{0.10}_{0.06}$	275^{2}_{49}	37^{10}_{10}	8.94 ± 0.08	2.92 ± 0.12	−21.41 ± 0.01
J1443444+184950	F14414+1902	$10.34^{0.08}_{0.02}$	281^{10}_{141}	14^{19}_{19}	···	2.47 ± 0.12	−21.07 ± 0.01
J0857505+512037	F08542+5132	$10.96^{0.03}_{0.04}$	1325^{247}_{61}	77^{87}_{87}	···	2.23 ± 0.43	−21.35 ± 0.01
J1106104+023458	···	$11.14^{0.03}_{0.03}$	292^{46}_{39}	7^{86}_{86}	···	2.59 ± 0.29	−21.77 ± 0.01
J1157412+321316	F11550+3233	$10.58^{0.03}_{0.08}$	238^{1}_{57}	62^{22}_{22}	8.79 ± 0.10	1.45 ± 0.02	−21.70 ± 0.01
J1149200−030357	F11467−0247	···	178^{10}_{16}	···	···	1.72 ± 0.03	−21.29 ± 0.01
J0126038+022456	F01234+0209	$10.88^{0.40}_{0.08}$	288^{31}_{34}	0^{0}_{0}	···	3.18 ± 0.48	−21.06 ± 0.01
J1556089+254358	F15540+2552	$10.47^{0.06}_{0.13}$	183^{5}_{83}	35^{14}_{14}	8.89 ± 0.11	2.19 ± 0.06	−21.08 ± 0.01
J0140364+260016	F01378+2545	$11.03^{0.18}_{0.32}$	1021^{152}_{52}	···	···	1.61 ± 0.67	−21.40 ± 0.02
J1257392+080935	F12551+0825	···	297^{32}_{11}	···	···	0.43 ± 0.01	−22.52 ± 0.01
J0800007+152319	···	···	237^{3}_{0}	···	···	1.34 ± 0.06	−21.40 ± 0.01
J0800279+074858	···	$11.26^{0.01}_{0.34}$	228^{3}_{42}	0^{4}_{4}	···	3.06 ± 0.17	−21.11 ± 0.01
J0834438+334427	F08315+3354	$10.42^{0.17}_{0.02}$	231^{17}_{86}	69^{42}_{42}	···	2.27 ± 0.08	−21.30 ± 0.01
J0823089+184234	···	$10.63^{0.01}_{0.12}$	634^{1068}_{44}	···	···	1.77 ± 0.15	−21.45 ± 0.01
J1202527+195458	F12002+2011	$10.58^{0.02}_{0.30}$	193^{17}_{6}	51^{11}_{11}	8.92 ± 0.08	1.89 ± 0.03	−21.06 ± 0.01
J0912533+192701	···	$10.71^{0.17}_{0.04}$	222^{49}_{20}	19^{14}_{14}	8.63 ± 0.28	2.87 ± 0.19	−22.04 ± 0.01
J0941010+143622	F09382+1449	···	968^{32}_{101}	···	···	1.37 ± 0.06	−22.29 ± 0.01
J1016332+041418	F10139+0429	$10.40^{0.32}_{0.01}$	423^{31}_{44}	38^{21}_{21}	8.40 ± 0.22	1.93 ± 0.09	−21.37 ± 0.01
J1401186−021131	···	$10.80^{0.01}_{0.25}$	201^{4}_{35}	6^{3}_{3}	···	2.01 ± 0.06	−21.98 ± 0.01
J1258241+224113	···	$10.09^{0.06}_{0.04}$	201^{25}_{16}	17^{14}_{14}	8.59 ± 0.23	2.77 ± 0.65	−19.93 ± 0.02
J1036317+022147	···	$9.98^{0.15}_{0.23}$	196^{12}_{14}	7^{2}_{2}	8.69 ± 0.12	1.68 ± 0.01	−20.43 ± 0.01
J1050567+185316	F10482+1909	$10.40^{0.14}_{0.07}$	678^{56}_{80}	154^{83}_{83}	···	2.49 ± 0.11	−21.23 ± 0.01
J1111177+192259	···	$10.27^{0.12}_{0.14}$	243^{2}_{36}	42^{8}_{8}	8.83 ± 0.15	0.98 ± 0.03	−21.62 ± 0.01
J1219585+051745	···	$10.88^{0.45}_{0.09}$	1277^{74}_{94}	···	···	2.52 ± 1.19	−21.66 ± 0.01
J1414276+605726	F14129+6111	$10.16^{0.06}_{0.06}$	220^{0}_{51}	28^{9}_{9}	8.69 ± 0.10	1.07 ± 0.02	−20.69 ± 0.01
J0936293+203638	F09336+2049	$10.60^{0.01}_{0.15}$	177^{16}_{8}	29^{11}_{11}	9.00 ± 0.23	2.44 ± 0.09	−21.34 ± 0.01
J1533582+113413	···	$11.34^{0.04}_{0.32}$	357^{78}_{67}	···	···	2.11 ± 0.41	−22.18 ± 0.01
J1348483+181401	F13464+1828	$10.16^{0.08}_{0.07}$	264^{18}_{17}	39^{18}_{18}	8.78 ± 0.84	2.75 ± 0.30	−19.73 ± 0.02
J1125319+290316	···	···	320^{10}_{32}	···	···	1.96 ± 0.03	−21.24 ± 0.01
J1603043+094717	F16006+0955	$10.51^{0.18}_{0.02}$	181^{14}_{10}	57^{21}_{21}	···	2.37 ± 0.06	−21.54 ± 0.01
J1639245+303719	F16374+3043	···	223^{5}_{25}	···	···	1.69 ± 0.08	−21.64 ± 0.01
J1050288+002806	···	$10.26^{0.01}_{0.22}$	416^{148}_{66}	63^{26}_{26}	8.74 ± 0.13	1.31 ± 0.04	−21.58 ± 0.01
J0928103+232521	···	$10.01^{0.32}_{0.03}$	202^{44}_{18}	10^{5}_{5}	9.06 ± 0.09	2.18 ± 0.17	−20.18 ± 0.02
J2344170+053520	F23417+0518	$11.61^{0.09}_{0.11}$	625^{14}_{218}	43^{275}_{275}	···	4.00 ± 1.64	−22.39 ± 0.01
J2353152−313234	···	···	186^{0}_{43}	···	···	···	
J1222488−040307	···	···	269^{20}_{16}	···	···	···	
J1419037−034657	···	···	213^{36}_{4}	···	···	···	
J1048019−013017	···	···	210^{29}_{40}	···	···	···	
J1338353−041131	···	···	239^{76}_{95}	···	···	···	
J0857064+190855	F08542+1920	···	1425^{34}_{139}	···	···	0.16 ± 0.01	−23.15 ± 0.01
J1022125+241208	F10194+2427	$10.78^{0.03}_{0.09}$	176^{113}_{27}	···	···	2.39 ± 0.07	−21.91 ± 0.01
J1422313+260205	F14202+2615	$10.31^{0.36}_{0.06}$	274^{83}_{30}	29^{8}_{8}	8.68 ± 0.09	1.15 ± 0.02	−21.47 ± 0.01
J1231216+275524	F12288+2811	$10.58^{0.15}_{0.04}$	367^{6}_{69}	7^{5}_{5}	8.54 ± 0.24	2.44 ± 0.09	−21.92 ± 0.01
J1251200+021900	F12487+0235	$10.60^{0.24}_{0.01}$	521^{56}_{18}	67^{67}_{40}	8.40 ± 0.32	1.67 ± 0.04	−22.24 ± 0.01
J0030089−002743	F00275−0044	···	496^{34}_{28}	···	···	···	
J0914140+032200	F09116+0334	$10.56^{0.06}_{0.01}$	200^{28}_{11}	374^{303}_{303}	···	2.21 ± 0.03	−21.92 ± 0.01
J1105377+311432	F11028+3130	$9.97^{0.06}_{0.04}$	272^{33}_{13}	3^{1}_{1}	···	1.90 ± 0.10	−20.72 ± 0.01
J0323227−075612	F03209−0806	$10.41^{0.12}_{0.03}$	235^{66}_{27}	37^{10}_{10}	8.75 ± 1.21	1.37 ± 0.03	−21.51 ± 0.01
J1632212+155145	F16300+1558	$10.65^{0.01}_{0.17}$	802^{38}_{60}	43^{36}_{36}	8.69 ± 0.21	1.75 ± 0.06	−22.07 ± 0.01
J0148531+002857	F01462+0014	$10.47^{0.03}_{0.24}$	340^{284}_{29}	74^{37}_{37}	···	1.33 ± 0.04	−21.72 ± 0.01
J0159503+002340	F01572+0009	···	467^{15}_{41}	···	···	···	
J1353317+042809	F13509+0442	···	473^{47}_{9}	···	···	···	

Table 5
(Continued)

AKARI-FIS-V1 Name	*IRAS* Name	$\log(M_{\rm star}(M_\odot))$	SFR(IR) ($M_\odot$ yr^{-1})	SFR(Hα) ($M_\odot$ yr^{-1})	12+log(O/H)	$u^{0.1}-r^{0.1}$ (mag)	$M_r^{0.1}$ (mag)
(1)	(2)	(3)	(4)	(5)	(6)	(7)	(8)
J0244173−003040	F02417−0043	...	202^{6}_{20}	...	...	...	
J1202268−012918	F11598−0112	...	394^{51}_{6}	...	...	...	
J1013477+465402	F10107+4708	$10.17^{0.30}_{0.05}$	302^{68}_{31}	...	...	1.98 ± 0.13	−20.91 ± 0.01
J0858418+104124	F08559+1053	$10.67^{0.06}_{0.04}$	254^{29}_{14}	...	...	2.18 ± 0.03	−21.91 ± 0.01
J1347336+121727	F13451+1232	...	259^{18}_{15}	...	...	...	
J0853252+252646	F08504+2538	...	405^{91}_{68}	...	...	...	
J0825215+383306	F08220+3842	$10.65^{0.06}_{0.01}$	329^{87}_{57}	26^{18}_{18}	8.64 ± 0.20	2.68 ± 0.11	−21.70 ± 0.01
J0829512+384528	F08266+3855	$9.66^{0.02}_{0.05}$	180^{51}_{27}	26^{19}_{19}	8.40 ± 0.27	2.11 ± 0.25	−19.45 ± 0.02
J1142035+005135	F11394+0108	$10.16^{0.21}_{0.07}$	214^{22}_{19}	75^{43}_{43}	...	1.08 ± 0.03	−21.63 ± 0.01
J0810595+281354	F08079+2822	$10.28^{0.36}_{0.01}$	775^{415}_{212}	36^{19}_{19}	8.06 ± 0.26	1.23 ± 0.06	−21.43 ± 0.01
J0900252+390400	F08572+3915	$9.42^{0.04}_{0.02}$	186^{6}_{16}	5^{2}_{2}	8.63 ± 0.14	1.84 ± 0.03	−19.40 ± 0.01
J0830197+192040	F08274+1930	$10.24^{0.16}_{0.07}$	186^{60}_{28}	18^{5}_{5}	8.89 ± 0.07	1.00 ± 0.03	−21.03 ± 0.01
J1121293+112233	F11188+1138	$10.46^{0.01}_{0.01}$	361^{39}_{20}	81^{27}_{27}	...	1.67 ± 0.03	−21.97 ± 0.01
J1006038+411223	F10030+4126	$10.18^{0.19}_{0.01}$	455^{35}_{50}	66^{40}_{40}	8.56 ± 0.27	1.38 ± 0.07	−21.46 ± 0.01
J0838034+505516	F08344+5105	$9.96^{0.08}_{0.01}$	186^{6}_{16}	18^{5}_{5}	8.63 ± 0.19	1.94 ± 0.03	−20.48 ± 0.01
J0902489+523623	F08591+5248	$10.57^{0.01}_{0.11}$	195^{6}_{25}	35^{12}_{12}	...	2.15 ± 0.04	−21.68 ± 0.01
J0847504+232113	F08449+2332	$10.23^{0.17}_{0.06}$	176^{42}_{29}	36^{8}_{8}	8.81 ± 0.07	1.06 ± 0.02	−20.88 ± 0.01
J1559301+380843	F15577+3816	$10.70^{0.01}_{0.05}$	268^{16}_{23}	23^{10}_{10}	...	1.89 ± 0.08	−21.56 ± 0.01
J1324197+053705	F13218+0552	...	795^{42}_{60}	...	...	...	
J1102140+380240	F10594+3818	$10.47^{0.12}_{0.04}$	245^{40}_{6}	45^{13}_{13}	8.89 ± 0.30	1.45 ± 0.02	−21.50 ± 0.01
J1204244+192509	F12018+1941	$10.15^{0.02}_{0.04}$	242^{11}_{18}	65^{35}_{35}	7.62 ± 0.37	1.90 ± 0.05	−21.30 ± 0.01
J1108513+065915	F11062+0715	...	200^{45}_{43}	...	...	...	
J1040290+105325	F10378+1108	$10.35^{0.18}_{0.01}$	311^{43}_{17}	43^{14}_{14}	...	2.21 ± 0.05	−21.35 ± 0.01
J1207210+021702	F12047+0233	$10.20^{0.24}_{0.11}$	211^{20}_{16}	48^{18}_{18}	8.89 ± 0.10	1.00 ± 0.03	−21.50 ± 0.01
J1255482−033908	F12532−0322	...	195^{69}_{33}	...	...	...	
J0906339+045136	F09039+0503	$10.45^{0.01}_{0.33}$	181^{29}_{14}	36^{14}_{14}	8.22 ± 0.20	1.82 ± 0.04	−20.82 ± 0.01
J1153144+131432	F11506+1331	$10.08^{0.05}_{0.01}$	311^{37}_{11}	$47^{28.}_{28}$	8.40 ± 0.28	2.17 ± 0.07	−20.51 ± 0.01
J1202054+112813	F11595+1144	$10.17^{0.50}_{0.01}$	268^{30}_{14}	71^{25}_{25}	8.75 ± 0.17	1.22 ± 0.02	−21.61 ± 0.01
J1006432+091726	F10040+0932	$10.34^{0.12}_{0.03}$	218^{36}_{11}	26^{15}_{15}	8.75 ± 0.15	1.55 ± 0.04	−21.06 ± 0.01
J1052232+440849	F10494+4424	$10.22^{0.04}_{0.03}$	196^{14}_{10}	20^{5}_{5}	8.37 ± 0.16	2.52 ± 0.06	−20.45 ± 0.01
J1254008+101115	F12514+1027	...	659^{50}_{75}	...	...	...	
J1348397+581854	F13469+5833	$10.46^{0.06}_{0.13}$	224^{16}_{16}	13^{6}_{6}	8.77 ± 0.40	2.23 ± 0.07	−21.02 ± 0.01
J1015153+272717	F10124+2742	$10.36^{0.32}_{0.01}$	213^{17}_{19}	49^{19}_{19}	8.45 ± 0.16	1.91 ± 0.06	−21.26 ± 0.01
J1356100+290538	F13539+2920	$11.00^{0.06}_{0.10}$	190^{7}_{18}	39^{14}_{14}	...	3.09 ± 0.11	−20.41 ± 0.01
J1502320+142132	F15001+1433	$10.44^{0.07}_{0.01}$	225^{20}_{15}	71^{28}_{28}	8.38 ± 0.21	2.07 ± 0.04	−21.58 ± 0.01
J1336237+391733	F13342+3932	...	405^{66}_{47}	...	...	...	
J1141215+405951	F11387+4116	$10.45^{0.06}_{0.02}$	174^{93}_{13}	70^{55}_{55}	8.14 ± 1.22	2.47 ± 0.06	−21.08 ± 0.01
J1433271+281157	F14312+2825	$10.72^{0.01}_{0.06}$	227^{102}_{31}	83^{32}_{32}	...	2.23 ± 0.05	−21.79 ± 0.01
J1450544+350835	F14488+3521	$10.86^{0.07}_{0.02}$	379^{115}_{103}	183^{57}_{57}	8.79 ± 0.15	1.55 ± 0.02	−22.33 ± 0.01
J1406380+010258	F14041+0117	$10.11^{0.18}_{0.01}$	387^{12}_{37}	11^{22}_{8}	7.79 ± 0.67	1.28 ± 0.04	−21.40 ± 0.01
J1522382+333135	F15206+3342	...	184^{6}_{18}	...	...	...	
J1505390+574305	F15043+5754	$10.45^{0.06}_{0.08}$	181^{9}_{30}	19^{11}_{11}	8.85 ± 0.13	1.29 ± 0.03	−20.69 ± 0.01
J1441041+532011	F14394+5332	...	186^{5}_{16}	...	...	...	
J1706529+382010	F17051+3824	$10.26^{0.01}_{0.01}$	241^{10}_{20}	14^{9}_{9}	...	2.17 ± 0.06	−20.94 ± 0.01
J1649140+342510	F16474+3430	$9.63^{0.32}_{0.15}$	201^{43}_{4}	6^{2}_{2}	8.87 ± 0.09	1.73 ± 0.06	−19.69 ± 0.01
J0823127+275140	F08201+2801	$10.38^{0.11}_{0.20}$	201^{16}_{12}	14^{4}_{4}	8.70 ± 0.10	1.58 ± 0.04	−21.19 ± 0.01
J1213460+024844	F12112+0305	$10.28^{0.01}_{0.01}$	306^{23}_{21}	9^{3}_{3}	8.39 ± 0.33	1.78 ± 0.03	−20.14 ± 0.01
J1346511+074720	F13443+0802	$10.57^{0.05}_{0.01}$	211^{33}_{10}	20^{3}_{3}	8.97 ± 0.04	2.08 ± 0.03	−21.49 ± 0.01
J2257246−262120	F22546−2637	...	249^{32}_{29}	...	...	...	
J2223286−270006	F22206−2715	...	266^{30}_{13}	...	...	...	
J1132417−053940	F11300−0522	...	161^{43}_{27}	...	...	...	
J0238167−322036	F02361−3233	...	350^{19}_{25}	...	...	...	
J0238126−473813	F02364−4751	...	201^{11}_{14}	...	...	...	

Table 5
(Continued)

AKARI-FIS-V1 Name (1)	*IRAS* Name (2)	$\log(M_{\mathrm{star}}(M_\odot))$ (3)	SFR(IR) ($M_\odot$ yr^{-1}) (4)	SFR(Hα) ($M_\odot$ yr^{-1}) (5)	12+log(O/H) (6)	$u^{0.1}-r^{0.1}$ (mag) (7)	$M_r^{0.1}$ (mag) (8)
J0237297−461544	F02356−4628	···	400^{59}_{53}	···	···	···	
J0048064−284820	F00456−2904	···	228^{23}_{11}	···	···	···	
J0112165−273819	F01098−2754	···	404^{7}_{170}	···	···	···	
J0138061−324519	F01358−3300	···	224^{43}_{8}	···	···	···	
J0302108−270725	F03000−2719	···	457^{28}_{70}	···	···	···	
J0118266−253607	F01160−2551	···	227^{23}_{13}	···	···	···	
J0152042−285116	F01497−2906	···	197^{28}_{18}	···	···	···	
J0159138−292436	F01569−2939	···	195^{37}_{6}	···	···	···	
J1329391−034654	F13270−0331	···	268^{305}_{0}	···	···	···	
J1112034−025414	F11095−0238	···	236^{44}_{11}	···	···	···	
J2307212−343838	F23046−3454	···	285^{30}_{11} ···	···	···		
J2208493−344627	F22058−3501	···	280^{33}_{75} ···	···	···		
J1425001+103045	F14225+1044	$10.77^{0.04}_{0.05}$	3766^{101}_{1151}	139^{80}_{80}	8.64 ± 0.17	1.19 ± 0.06	−22.62 ± 0.00

Notes. (1) *AKARI* FIS-V1 Catalog name. (2) *IRAS* Faint Source Catalog name. (3) Stellar mass adopted from Maraston et al. (2013). (4) SFRs derived from IR luminosity. (5) SFRs derived from Hα luminosity. (6) Oxygen abundances derived in this work. (7) $u^{0.1}-r^{0.1}$ color. (8) Absolute magnitude in the r band.

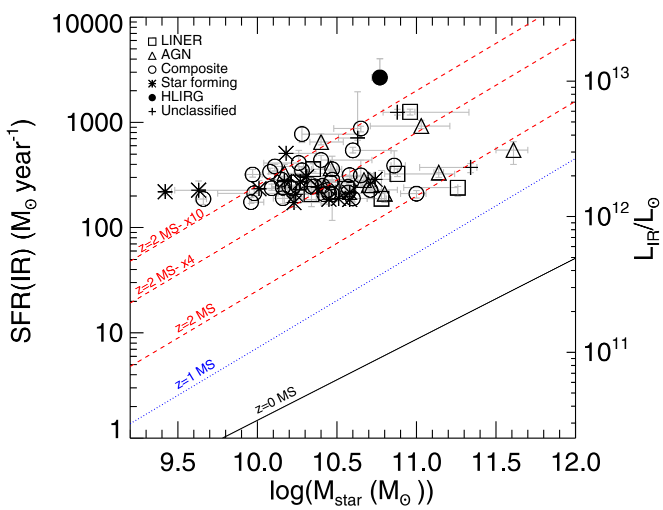

Figure 10. SFR(IR) vs. stellar mass for 75 ULIRGs and one HLIRG. The SFR(IR) values are derived from Equation (4) of Kennicutt (1998). The error bars of SFR(IR) represent the uncertainties propagated through L_{IR} uncertainties. The solid line is the $z = 0$ "main sequence" of normal star-forming galaxies; see Equation (5) of Elbaz et al. (2007). The dotted (colored blue in the online version) line is the SFR–M_{star} relationship of $z = 1$ star-forming galaxies in the GOODS fields; see Equation (4) of Elbaz et al. (2007). The dashed (colored red in the online version) lines represent the SFR–M_{star} relationship of $z = 2$ star-forming galaxies in the GOODS fields (Daddi et al. 2007) and 4 and 10 times above this relationship.

(A color version of this figure is available in the online journal.)

overestimated up to 80–100% (Veilleux et al. 2009). Derived SFR(IR) values are tabulated in Table 5.

Figure 10 shows SFR versus M_{star} for 75 ULIRGs and one HLIRG, for which M_{star} estimates are given by Maraston et al. (2013). The solid (black), dotted (blue), and dashed (red) lines represent the "main sequence" of normal SFGs at $z \sim 0$ (Elbaz et al. 2007), $z \sim 1$ (Elbaz et al. 2007), and $z \sim 2$ (Daddi et al. 2007), respectively. For comparison we also show the 4 and 10 times above the $z \sim 2$ "main sequence" (MS) relationship (top dashed lines). Local ULIRGs exhibit extremely high SFRs compared to normal SFGs with the same masses. It is evident from Figure 10 that local ULIRGs lie above the "main sequence" up to $z \sim 2$. We note that the "main sequence" relationships represent the total SFR obtained from the L_{IR} and UV continuum, SFR(IR+UV). Because we do not include SFR from the UV continuum, SFR(UV), our SFR(IR) estimates are lower than for SFR(IR+UV). However, the total SFR is dominated by SFR(IR), and therefore the difference between SFR(IR) and SFR(IR+UV) should be small.

Previously, Elbaz et al. (2007) showed that (their Figure 17) Arp220 (a well-studied nearby ULIRG) exhibits a large offset both from the "main sequence" and the $z \sim 1$ relationship. In the same figure they also show that M82 (a starburst galaxy) lies above the local main sequence, but it is located in the 1σ confidence level of the $z \sim 1$ SFR–M_{star} relationship. da Cunha et al. (2010) also compared local ULIRGs with local star-forming SDSS galaxies and showed that ULIRGs have higher SFRs. In Figure 10 we show a large local ULIRG sample, 75 ULIRGs, and one HLIRG. We find that local ULIRGs do not exhibit typical SFR for their masses even at $z \sim 2$. Compared to the "main sequence" at $z \sim 0$, $z \sim 1$, and $z \sim 2$, on average ULIRGs have 92, 17, and 5 times higher SFRs, respectively. Local ULIRGs seem to be equally distributed around the dashed line, representing four times above the $z \sim 2$ MS. Compared to the "main sequence" at $z \sim 2$, on average the AGNs, LINERs, and composite and star-forming ULIRGs have 3, 4, 5, and 5 times higher SFRs, respectively. We do not see a significant systematic offset with optical spectral type. However, we note that AGNs, LINERs, and composites tend to have the highest SFR(IR), which might be a sign of the AGN contamination of L_{IR}. We discuss the impact of SFH on stellar mass estimates in Section 4.5.

The ionizing radiation of recently formed young stars produces nebular lines such as Hα; hence it traces the unobscured radiation generated by star formation. Therefore, it can be used to derive the SFR. As noted above, Thomas et al. (2013) only correct for the diffuse dust extinction widely spread throughout the whole galaxy that affects the emission lines and stellar continuum, but they do not consider an embedded dust component local to star-forming regions that affects the emission lines. This is mainly to avoid highly uncertain dust extinction

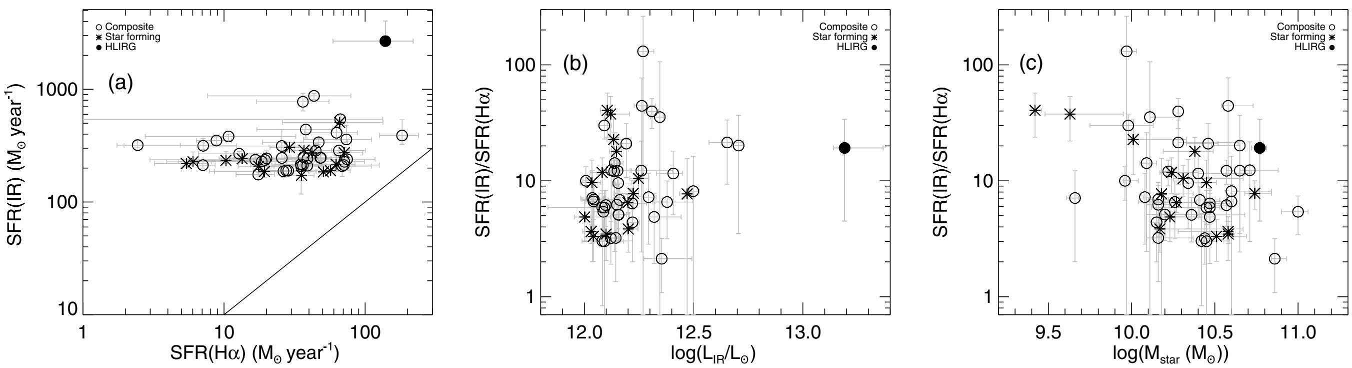

Figure 11. (a) SFR(IR) vs. SFR(Hα), (b) SFR(IR)/SFR(Hα) vs. L_{IR}, and (c) stellar mass for 55 ULIRGs and one HLIRG. In panel (a) the solid line represents the one-to-one relation.

values measured from a Balmer decrement due to low signal-to-noise ratio (S/N) spectra. However, if we avoid this additional dust extinction, we may underestimate the SFR based on Hα luminosity, SFR(Hα). Therefore we use the already dereddened emission-line fluxes (only for the diffuse dust component) given in emissionlinesPort[3] catalog and obtain the Balmer decrement. The predicted Hα/Hβ ratio is 2.86 for 10^4 K (Osterbrock & Ferland 2006), and we adopt this value to estimate the local dust extinction around nebular regions and correct Hα emission-line flux for the estimated extinction. Applying this additional extinction correction typically results in a factor of 3.4 higher Hα emission-line flux with large uncertainties. We apply Equation (2) given in Kennicutt (1998) to obtain SFR(Hα), as listed in Table 5. Because in the presence of an AGN Hα emission represents the photoionization from the AGN, we do not obtain SFR(Hα) for AGNs and LINERs. Figure 11 shows a comparison between the SFR(IR) and SFR(Hα) values (a). Note that error bars of SFR(Hα) are dominated by the Hα and Hβ emission-line flux uncertainties. The SFR(IR) values are systematically larger than the SFR(Hα) values; this difference is between a factor of 2 and a factor of 130, and the median difference is a factor of 8. This indicates that even with the highest possible dust extinction correction applied, the Hα luminosity underestimates SFR at least by a factor of two. Therefore, it is evident that Hα is not sufficient to trace the SFR for ULIRGs, and IR observations are crucial to inferring the SFR of these galaxies. This is consistent with the fact that hydrogen recombination line SFR indicators are underluminous relative to the IR indicators in ULIRGs (e.g., Goldader et al. 1995; Kim et al. 1998). In Figures 11(b) and (c) show that the difference between the SFR(IR) and SFR(Hα) does not depend on L_{IR} or M_{star}. In Figure 12 SFR(Hα) versus M_{star} is shown. Although SFR(Hα) underestimates SFR, Figure 12 shows that ULIRGs still lie above the local main sequence.

3.4.2. Stellar Mass and Gas Metallicity

Nuclear metallicities and stellar masses of normal star-forming galaxies show a well-established M_{star}–Z correlation (Tremonti et al. 2004, hereafter T04). In the following, we compare the stellar masses and oxygen abundances of ULIRGs with the mass–metallicity relation of local star-forming SDSS galaxies obtained by Tremonti et al. (2004). Reliable metallicity constraints are difficult to obtain from the broadband SED fitting applied by Maraston et al. (2013). Therefore, in order to measure metallicity we adopt the relevant emission-line fluxes from Thomas et al. (2013). First, we apply the additional extinction correction based on the Balmer decrement (see Section 3.4.1) to the adopted emission-line fluxes. Then we compute the line ratio R_{23} = ([O II] $\lambda\lambda$3726, 3729+[O III] $\lambda\lambda$4959, 5007)/Hβ. We convert R_{23} values to oxygen abundances, O/H, by following Equation (1) of Tremonti et al. (2004). We list the derived oxygen abundances in Table 5. Note that this conversion and the R_{23} line ratio are only applicable to normal star-forming galaxies, and they are not relevant for AGNs because the radiation from the AGN contributes to the line emission. Therefore we do not calculate metallicities for AGNs, and to be conservative we also exclude LINERs from this investigation. After excluding AGNs and LINERs, we are left with 48 ULIRGs and one HLIRG for which emission-line fluxes are given by Thomas et al. (2013).

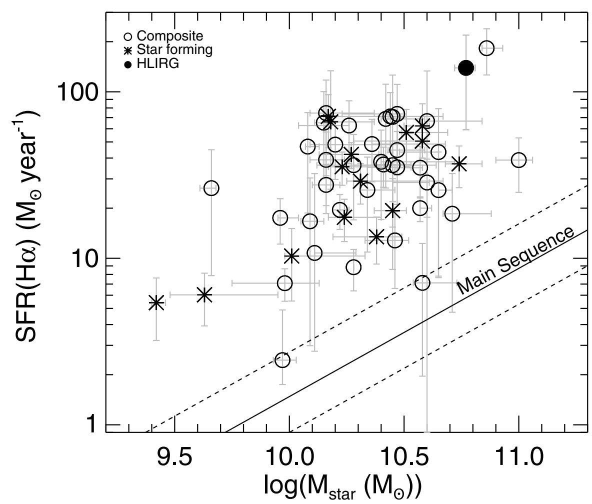

Figure 12. SFR(Hα) vs. stellar mass. The SFR(Hα) values are derived from Equation (2) of Kennicutt (1998). The error bars of SFR(Hα) are dominated by the emission-line fluxes. The black solid line is the "main sequence" from Elbaz et al. (2007); dashed lines represent the 1σ width of the "main sequence".

The M_{star}–Z distribution of our ULIRG sample is shown in Figure 13 (top). The error bars of the oxygen abundances represent the uncertainties associated with emission-line fluxes and additional extinction obtained from the Balmer decrement. The black solid line is the M_{star}–Z relationship, Equation (3) given by Tremonti et al. (2004). The vast majority of ULIRGs (46 out of 48) have lower metallicities than that of the normal star-forming SDSS galaxies at similar masses. In the bottom panel of Figure 13, the distribution of the residuals of the measured oxygen abundances to the expected oxygen abundances from the T04 relationship is displayed. The distribution of the residuals is comparable to the overplotted Gaussian distribution with standard deviation σ = 0.20 dex; therefore we consider the shift of ULIRGs from the T04 relationship as

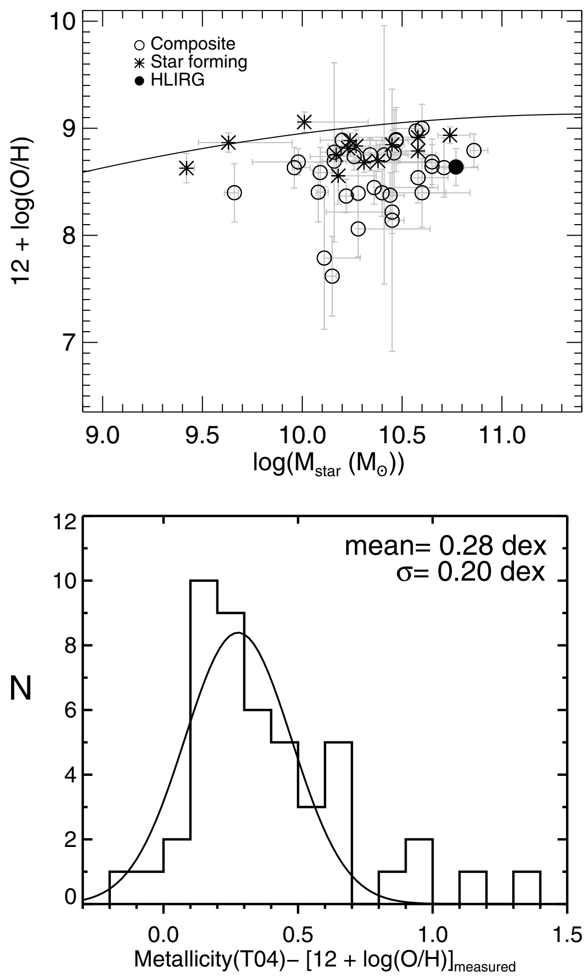

Figure 13. Top: oxygen abundances vs. stellar mass for 48 ULIRGs and one HLIRG. The black solid line represents the mass–metallicity relation of the local SDSS galaxies given by Tremonti et al. (2004). Error bars of the oxygen abundances represent the uncertainties of emission-line fluxes (including the uncertainties associated with additional extinction based on the Balmer decrement) propagated through Equations (1) and (2) of Tremonti et al. (2004). Bottom: the distribution of the residuals between the measured oxygen abundances and the ones expected from the T04 relation. The overplotted Gaussian function demonstrates that the residuals have a normal distribution with a few outliers.

0.20 dex. Normal star-forming SDSS galaxies exhibit a scatter between 0.07 dex–0.2 dex with a mean of 0.1 dex (Tremonti et al. 2004) around the stellar mass–metallicity relation. The scatter of normal star-forming galaxies from this relationship is mostly attributed to the observational errors in the mass and metallicity measurements (Tremonti et al. 2004). The scatter of ULIRGs (0.20 dex) is equal to the upper limit of the scatter of normal star-forming galaxies. The median error in metallicity measurements of ULIRGs is large, ∼0.17 dex, and the median error in mass measurements is smaller, ∼0.08 dex. If we consider the lower error bars, it is very likely that the metallicity distribution of ULIRGs may shift to even lower values, and this may result in a larger scatter with respect to the T04 relationship. However, if we consider the upper error bars, only six ULIRGs may move above the T04 relationship, and most of the ULIRGs would still lie below this relationship.

Previously, Rupke et al. (2008) showed that ULIRGs are underabundant compared to the SFGs on the $M_{\rm star}$–Z relation. The position of our ULIRG sample with respect to the $M_{\rm star}$–Z relationship of normal SFGs is consistent with the results of (Rupke et al. 2008). In our $M_{\rm star} - Z$ subsample, 11 of the 48 ULIRGs are also part of the 100 (U)LIRGs of Rupke et al. (2008). Because a small fraction (23%) of our sample overlaps with the sample of Rupke et al. (2008), our results are highly independent of theirs.

3.4.3. Color–Magnitude Distribution of ULIRGs

The color versus magnitude distribution, the so-called color–magnitude diagram, of galaxies out to $z \sim 1$ show two separate distributions (e.g., Hogg et al. 2003; Blanton et al. 2003; Baldry et al. 2004, 2006; Cooper et al. 2006; Muzzin et al. 2012): (1) a "red sequence" of early-type galaxies, and (2) a "blue cloud" of late-type galaxies. The red sequence galaxies are bulge-dominated, more massive, non-star-forming, passive galaxies (e.g., Blanton et al. 2003, 2005; Hogg et al. 2003; Baldry et al. 2006; Driver et al. 2006). The blue cloud galaxies are disk-dominated, less massive, actively star-forming galaxies (e.g., Kauffmann et al. 2003b; Brinchmann et al. 2004; Wyder et al. 2007). Observations show that while the number density of blue cloud galaxies has stayed almost constant, the red sequence galaxies have doubled from $z \sim 1$ to $z \sim 0$ (Bell et al. 2004; Faber et al. 2007). This suggests that star-forming disk galaxies at $z \sim 1$ evolve to local passive galaxies. Such an evolution involves different physical processes that change galaxy morphology and quench star formation. As galaxies go through a transition phase from blue cloud to red sequence, they reside in the region in between, the so-called green valley.

The transition of a late-type galaxy to an early type includes physical processes that are not fully understood yet. Mergers and AGN feedback are among the proposed star formation quenching mechanisms (e.g., Barnes & Hernquist 1996; Hopkins et al. 2006, 2008a). Becasue ULIRGs are both merging systems and mostly host an AGN, they are good candidates for evolving galaxies from a blue cloud to a red sequence. In the following, we explore the location of our ULIRG sample in the CMD of local SDSS galaxies.

For this investigation we have selected a local comparison sample from the SDSS DR 10 database. We selected sources classified as galaxies that are brighter than $r_{\rm Petrosian}$ <17.7 and have spectroscopic redshifts within the $0.018 < z < 0.260$ interval ($z_{\rm median} = 0.1$). We also select galaxies that have photometric measurements in the u, g, and r bands. Our selection criterion leads to 499,953 galaxies. Throughout this analysis we use the Galactic extinction corrected "modelMag" measurements from the SDSS DR10 "PhotoObj" catalog. The K-corrections are calculated using the *kcorrect* code v4.2 of Blanton & Roweis (2007). For comparison with previous studies, we derive K-corrections for a fixed bandpass shift by $z = 0.1$. The absolute magnitudes and colors are denoted with $M_r^{0.1}$ and $u^{0.1}{-}r^{0.1}$, respectively; these are tabulated in Table 5. Figure 14 shows the CMD, $(u^{0.1}{-}r^{0.1})$ versus $M_r^{0.1}$, of the comparison and our ULIRG samples. The contours represent the number density of the comparison sample. The distribution of local SDSS galaxies shows two separate distributions: the red sequence and the blue cloud. We determine the color–magnitude relation of the red sequence and the blue cloud by following Baldry et al. (2004). We divide the comparison sample into 16 $M_r^{0.1}$ bins from −23.5 to −15.5; the bin size is 0.5 mag. For each $M_r^{0.1}$ bin we fit the color distribution with a double Gaussian and obtain the mean and variance for the red and the blue distributions. We adopt the color function and the absolute magnitude functions given by Baldry et al. (2004) and obtain

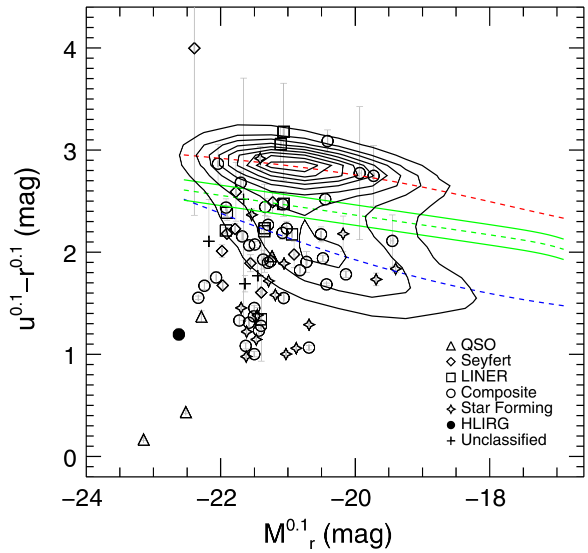

Figure 14. Color–magnitude diagram for a local SDSS comparison sample, 82 ULIRGs and one HLIRG. The contours represent the number densities for 10 levels. (H)ULIRGs are shown on top of the contours. The color–magnitude relations for the red sequence (the upper dashed, colored red in the online version), the blue sequence (the lower dashed, colored blue in the online version) and the green valley (the lower dashed, colored green in the online version) are shown. The solid (colored green in the online version) lines show the ±0.1 mag width of the green valley. See the text for detailed descriptions of these relations. The vertical and horizontal error bars represent the uncertainties in the model magnitude measurements.

(A color version of this figure is available in the online journal.)

the color–magnitude relations as

$$(u^{0.1} - r^{0.1})_{\mathrm{red-sequence}} = 2.559 + (-0.045) \times (M_r^{0.1} + 20) + (-0.298) \times \tanh\left(\frac{M_r^{0.1} - (-17.757)}{2.833}\right), \quad (1)$$

$$(u^{0.1} - r^{0.1})_{\mathrm{blue-cloud}} = 2.831 + 0.066 \times (M_r^{0.1} + 20) + (-2.180) \times \tanh\left(\frac{M_r^{0.1} - (-22.999)}{6.786}\right). \quad (2)$$

The upper and lower dashed lines in Figure 14 represent the red and blue sequence color–magnitude relations, respectively. To derive the color–magnitude relation of the green valley, we locate the minimum in the double Gaussian functions. We then fit a linear plus a tanh function, the same function used to fit red and blue sequence relations, to the minimums. The resulting relation of the green valley is

$$(u^{0.1} - r^{0.1})_{\mathrm{green-valley}} = 2.232 + (-0.096) \times (M_r^{0.1} + 20) + (-0.131) \times \tanh\left(\frac{M_r^{0.1} - (-16.447)}{0.492}\right). \quad (3)$$

We choose the width of the green valley to be 0.1. The middle dashed line in Figure 14 represents Equation (3); the solid lines represent the 0.1 mag width.

In Figure 14 the color–magnitude distribution of 82 ULIRGs and one HLIRG in our sample is shown on top of the contours of the comparison sample. From our ULIRG sample, 10 are in the red sequence, 6 are in the green valley, and 66 are in the blue cloud. Some 81% of the ULIRGs are located in the blue cloud, 12% are in "the red sequence," and only 7% are in the green valley. Two of the 6 (33%) ULIRGs are in the "green valley" and host an AGN. One of the 10 (10%) ULIRGs is in the red sequence, and 16% of the ULIRGs in the blue cloud host an AGN. The fraction of the AGN-hosting ULIRGs is highest in the green valley. Some 40% (33 of 82) of the ULIRGs are located outside of the 90% level contour. The median absolute magnitude and the $u^{0.1}$–$r^{0.1}$ color of our ULIRG sample are $M_r^{0.1} = -21.40 \pm 0.71$ and $u^{0.1} - r^{0.1} = 1.91 \pm 0.64$. The median absolute magnitude of the comparison SDSS sample is $M_r^{0.1} = -20.55 \pm 1.12$. Compared to the local SDSS sample, the absolute magnitudes of ULIRGs are 0.86 mag brighter. The median $u^{0.1} - r^{0.1}$ of the comparison sample is $u^{0.1} - r^{0.1} = 2.56 \pm 0.55$, so ULIRGs have 0.64 mag brighter colors. Because ULIRGs are selected by their star-formation-powered IR luminosity, we expect them to be bright optical sources. So in a sense their bright optical colors are consistent with their identification criteria.

Chen et al. (2010) study the color–magnitude properties of a sample of 54 ULIRGs from a *IRAS* 1 Jy sample (Kim et al. 1998) and show that ULIRGs are mostly in the blue cloud. They also find that compared to SDSS galaxies local ULIRGs are 0.2 mag bluer in $g - r$. Compared to Chen et al. (2010), we study a larger ULIRG sample and find consistent results; we find very similar color–magnitude properties. The distribution of our ULIRG sample across the color–magnitude diagram is also similar to the distribution shown by Chen et al. (2010). We find a smaller fraction for the ULIRGs that lie outside of the 90% level contour. While they do not find any AGN-hosting ULIRGs in the "green valley," we find two ULIRGs. In our color–magnitude subsample, 22 of the 82 ULIRGs are also part of the 54 ULIRGs studied by Chen et al. (2010). Because only a small fraction (27%) of our color–magnitude subsample overlaps with the sample of Chen et al. (2010), our results are independent of theirs.

We note that the colors of the AGN-hosting ULIRGs have a contribution from the central AGN. In principle, AGN contamination makes the ULIRG colors bluer, and this may shift them from the green valley to the blue cloud. However, Chen et al. (2010) show that on average removing the AGN contamination changes the color only by a small amount (0.005–0.007 mag). For their sample, only one source moved closer to the green valley, and 11 out of 12 remained close to their original positions. Chen et al. (2010) show that the lack of AGNs in the green valley is not due to AGN contamination. In our sample, three of the 15 AGN ULIRGs are part of the 12 AGN ULIRGs studied by Chen et al. (2010), and therefore we assume their results to be valid for our sample. Because it is beyond the scope of this work, we do not attempt to remove the AGN contribution for the AGN-hosting ULIRGs.

4. DISCUSSION

4.1. Infrared Luminosities

The IR luminosities computed in this work highly depend on the selected SED library of Dale & Helou (2002). Goto et al. (2011a) compare the IR luminosities computed from the SED models of Chary & Elbaz (2001), Dale & Helou (2002), and Lagache et al. (2003) and quote the median offsets between the models as 13%–24%. The listed IR luminosities in this work might have similar offsets between these models.

In contrast, the SED models of Dale & Helou (2002) represent especially the IR SEDs of normal SFGs, and they are not specifically developed for ULIRGs. For example, Rieke et al.

(2009) compare the observed SEDs of five local purely star-forming ULIRGs with a Dale & Helou (2002) template with $\alpha = 1.5$ and point out that at high IR luminosities the FIR bump of their SEDs is more peaked. If the intrinsic SEDs of local ULIRGs are more peaked than in Dale & Helou (2002) SED models, then the IR luminosities computed in this work might be overestimated. However, the comparison of Rieke et al. (2009) is based on a very small sample, and a full comparison between possible ULIRG SEDs is beyond the scope of this work. However, Rieke et al. (2009) and our sample have one common source, *IRAS* 12112+0305, for which we compare the IR luminosities based on the Dale & Helou (2002) model SED and the observed SED used by Rieke et al. (2009). We find that the IR luminosity computed from the Dale & Helou (2002) model SED is only ∼5% higher than IR luminosity based on the SED template of Rieke et al. (2009). This shows that while Rieke et al. (2009) state that their SEDs are more peaked compared to the Dale & Helou (2002) template, the difference between the IR luminosities is small. These considerations suggest that the IR luminosities presented in this work do not have a significant systematic offset. Even though the Dale & Helou (2002) models are not special for ULIRGs, the high number of already known ULIRGs in our sample that are identified based on these SED templates indicates that the IR luminosity measurements based on the SED templates of Dale & Helou (2002) are reliable for identifying ULIRGs.

4.2. FIR Colors

In Panel (d) of Figure 4, four sources, J1639245+303719, J0159503+002340, J1356100+290538, and J1706529+382010, exhibit extreme $\log(F(140\,\mu\mathrm{m})/F(160\,\mu\mathrm{m})) > 0.9$ colors compared to the models. For these cases we check the reliability of the flux measurements from the *AKARI* catalogs. In all of these cases, while the 90 μm flux is highly reliable, the 65 μm, 140 μm and 160 μm flux measurements are of low quality, and the uncertainty of the 160 μm flux is not given. In such cases we assumed the uncertainty as 25% of the given flux measurement, but it seems that these uncertainties could be even larger. Because the 90 μm flux measurements are secure, we still consider the measured IR luminosities to be reliable. The SEDs of three cases, J1639245+303719, J1356100+290538, and J1706529+382010, show that their flux densities at 140 μm are ∼0.8 dex larger than that of the models. The SED of J0159503+002340 also exhibits a large difference (>1 dex) between the observed and model flux at 160 μm. We also checked five more sources with $\log(F(140\,\mu\mathrm{m})/F(160\,\mu\mathrm{m})) > 0.5$: J1603043+094717, J0030089−002743, J1102140+380240, J1346511+074720, and J2307212−343838. The SEDs of J0030089−002743, J1102140+380240, J1346511+074720, and J2307212−343838 show that their flux densities at 140 μm is 0.5–0.8 dex larger than that of the models. The SED of JJ1603043+094717 also exhibits a 0.6 dex difference between the observed and model flux at 160 μm. These large differences between the observed colors and what are expected from the SED models can be attributed to the low-quality 140 μm and 160 μm flux measurements.

As mentioned in Section 3.1.3, the SED models cover only the $\log(F(140\,\mu\mathrm{m})/F(160\,\mu\mathrm{m}))$ color range between −0.5425–0.2135, and therefore in Panel (c) the three sources, J1202527+195458, J1559301+380843, and J1502320+142132, appear as outliers with $\log(F(140\,\mu\mathrm{m})/F(160\,\mu\mathrm{m})) < -0.58$. The SEDs of these sources show that their 65 μm fluxes are ∼0.5 dex lower than that of the models. Although the quality of the 65 μm flux measurements are low for these sources, it is more likely that the limited parameter range of the models is the main reason for their large deviation from the models. If the intrinsic SEDs of ULIRGs are more peaked compared to the templates of Dale & Helou (2002) as shown by Rieke et al. (2009), then we might expect to have a wider distribution for the FIR colors, and this might explain the large scatter seen in Panels (c) and (d).

4.3. Interaction Classes

In Section 3.2 the interaction classes of 64 sources are adopted from the literature (Veilleux et al. 2002; Hwang et al. 2007), and 55 sources are classified in this work based on visual inspection. Although visual classification is a subjective method, we prefer it because of its practical application. Two classifiers independently classified each source, and for most of the cases there was good agreement. There was a disagreement between the classifiers only for a few cases that are single-nucleus systems at higher redshifts. In such systems, the identification of the disturbed morphologies or weak interaction signs is difficult. However, the number of such systems are only five, and most of them are not included in our statistics because of the applied redshift limit. Even if they were included in our statistics, they would be classified as N I instead of V, and this would only decrease the number of sources classified as old mergers. Such a change would not change the high percentage of IV and V systems in the overall population.

Wide binary (IIIa) systems have the largest uncertainties because most of the companion galaxies do not have spectroscopic redshifts. However, wide binary galaxies usually have similar colors, and they show interaction signs. Therefore the chance coincidences are low, and the assumed physical connection is highly likely. Even if most of the IIIa systems were instead IV, the dominance of the mergers still holds. So the overall conclusion of the morphology investigation in Section 3.2, that the vast majority of ULIRGs in the local universe are single-nucleus ongoing or old mergers, is not affected by the disagreements of the classifiers or unconfirmed redshifts of the companion galaxies in wide binaries.

4.4. AGN Fraction of Our ULIRG Sample

In Section 3.3 we investigate the optical spectral types of the ULIRGs in our sample. The classification of star-forming galaxies, composites, LINERs, and Seyferts is based on empirical emission-line diagnostics. The ULIRGs are dust-rich systems, and dust extinction at optical wavelengths is high. Therefore, the dusty nature of ULIRGs brings a large uncertainty to their optical emission-line diagnostics. Nardini et al. (2010) use the rest-frame 5–8 μm spectra to disentangle the contribution of star formation and AGNs in ULIRGs. As shown by Nardini et al. (2010), optical diagnostics do not provide reliable information on the presence of AGNs. They trace obscured AGNs in some LINERs and even some star-forming galaxies. Therefore, as stated earlier, our spectral classification provides only a lower limit on the AGN fraction. This brings a large uncertainty to the AGN fraction per L_{IR} bin presented in Figure 9. It is very highly likely that most of the composites and LINERs may have an AGN component. If all of the LINERs and composites had an AGN contribution, then the correlation between the AGN fraction and L_{IR} would still be valid.

Assuming all of the LINERs and composites as AGNs may be an unrealistic overestimation because we would expect at least some fraction of the low-luminosity ULIRGs to be dominated by star formation. To investigate the hidden AGNs among such sources in our sample, we look at the result of the mid-IR diagnostic applied by Nardini et al. (2010). In total we have 31 overlapping sources with their sample. Our main interest is the AGN component of the star-forming galaxies, composites, and LINERs in our sample. For those sources we adopt the AGN bolometric contribution parameter given by Nardini et al. (2010) (the $\alpha_{\rm bol}$ parameter in their Table 1). Only one star-forming galaxy (J0900252+390400) in our sample seems to have a significant AGN contribution. If we consider this source as an AGN instead of a star-forming galaxy, this would not affect the correlation of AGNs and the anticorrelation of star-forming galaxies with IR luminosity. Also, it would have a negligible effect on the fraction of AGNs: the fraction of AGNs would increase to 26%, and the fraction of star-forming galaxies would decrease to 19%.

4.5. The Offset of ULIRGs from the Main Sequence of Star-forming Galaxies

The star-formation rate and $M_{\rm star}$ are tightly correlated from $z \sim 0$ to $z \sim 2$; the slope is between ∼0.6 and ∼1.0 (mostly depending on the galaxy sample), but the normalization decreases with redshift. This indicates that the overall SFR increases from $z \sim 0$ to $z \sim 2$, and the SFGs were forming stars more actively in the past compared to lower redshift galaxies at the same masses. The observations indicate that high-redshift SFGs contain a larger molecular gas reservoir (e.g., Daddi et al. 2010; Tacconi et al. 2010), and therefore the star-formation rate per stellar mass is higher at $z \sim 2$; in time this reservoir is used up and results in lower SFRs at $z \sim 0$. Figure 10 clearly demonstrates that local ULIRGs are outliers with respect to the "main sequence" of the normal SFGs up to $z \sim 2$. Local ULIRGs are already known to be outliers compared to the local "main sequence" (Elbaz et al. 2007). This is not surprising because, in the first place, ULIRGs are defined by their enormous IR luminosities powered by intense star formation, and in order to be defined as ULIRGs they should have $172 \leqslant$ SFR(IR) $\leqslant$ 1721. So their position on the y-axis is a pure selection effect, and we expect them to have higher SFRs than normal star-forming galaxies. We note that Figure 10 includes type-2 AGNs, LINERs, and composites. As mentioned earlier, even the AGN has a contribution to $L_{\rm IR}$, and the measured IR luminosities are mainly dominated by the FIR emission. As mentioned in Section 3.4.1, the average AGN contamination is ∼40.0% (Veilleux et al. 2009), but the offset of the local ULIRGs from the "main sequence" relations from $z \sim 0$–2 is relatively large and cannot be attributed to the AGN contribution in the SFR(IR) estimates alone.

Normal starburst galaxies are also outliers off the "main sequence" at $z \sim 0.7$ (Guo et al. 2013) and at $z \sim 2$ (Rodighiero et al. 2011). Guo et al. (2013) show their best-fit main sequence and the main sequence relationships given by Elbaz et al. (2007) and Daddi et al. (2007) in their Figure 7, where they report starburst galaxies as outliers. Because the local ULIRG sample lies above these main sequence relationships and their galaxy sample, it can be concluded that compared to normal starburst galaxies at $z \sim 0.7$ local ULIRGs exhibit higher SFRs. Rodighiero et al. (2011) define off-sequence galaxies (see their Figure 1) as the ones lying a factor of 10 above the $z \sim 2$ SFR–$M_{\rm star}$ relation of Daddi et al. (2007). Compared to these extreme outliers at $z \sim 2$, as seen in Figure 10, 90% of the local ULIRGs have lower SFRs, and only 10% have comparable

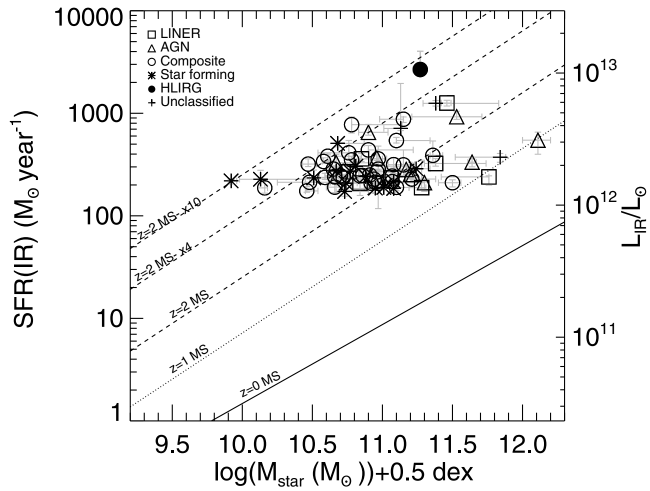

Figure 15. Same as Figure 10, but stellar masses are shifted by 0.5 dex.

SFRs. The SMGs, often referred as high-redshift analogs of local ULIRGS, are also known to be outliers compared to the $z \sim 2$ SFR–$M_{\rm star}$ relation (Tacconi et al. 2008; Daddi et al. 2007, 2009; Takagi et al. 2008). Compared to massive SFGs at the same masses, SFRs of SMGs are 10 times higher (Daddi et al. 2007, but also see Michałowski et al. 2012). As noted by Daddi et al. (2007), SMGs at $z \sim 2$ and local ULIRGs have similar properties: both are rare sources and outliers in SFR–$M_{\rm star}$ relations. However, compared to the location of SMGs shown by Daddi et al. (2007) (their Figure 17(b)), local ULIRGs occupy a wider $M_{\rm star}$ range, and they are closer to the $z \sim 2$ SFR–$M_{\rm star}$ relation.

As expected, galaxies with similar IR luminosities should have similar SFRs and positions in the SFR–$M_{\rm star}$ diagram. In particular, we call attention to the role of the stellar mass as the distinguishing parameter. At this point it is important to consider the uncertainties of the stellar masses in interpreting Figure 10. The ULIRGs in our sample have moderate stellar masses within the $9.42 < \log(M_{\rm star}(M_\odot)) < 11.61$ range, and the median is 10.41. We compare the adopted stellar masses from Maraston et al. (2013) with the $M_{\rm star}$ estimates given by previous ULIRG studies. Rodríguez Zaurín et al. (2010) provide $M_{\rm star}$ estimates for 36 local ULIRGs derived by performing spectral synthesis modeling on high-quality optical spectra. We have two sources that overlap with their sample, J0900252+390400 and J1052232+440849, and they report 1.0 dex and 0.5 dex higher stellar masses, respectively. However, we note that J0900252+390400 is the lowest mass ULIRG in our sample, and as mentioned in Section 4.4 it has an AGN. Therefore, we consider the difference of 1 dex in $M_{\rm star}$ for this particular object to be an exceptional case. da Cunha et al. (2010) also provide $M_{\rm star}$ estimates for a sample of 16 purely star-forming ULIRGs based on full SED modeling, including UV to FIR wavelengths. We have one common source with this sample (J1213460+024844), and for this source the $M_{\rm star}$ estimates agree well; their estimate is just 0.06 dex higher than the adopted value from Maraston et al. (2013). As shown by Rodríguez Zaurín et al. (2010), ULIRGs contain different stellar populations (very young, young, intermediate-young, and old stellar populations) at the same time, and their optical light is mainly dominated by the less-massive young stellar populations. Therefore, we expect the stellar mass estimates of ULIRGs to be highly dependent on the approach followed (SED or spectral fitting), the data used, and the assumed star-formation

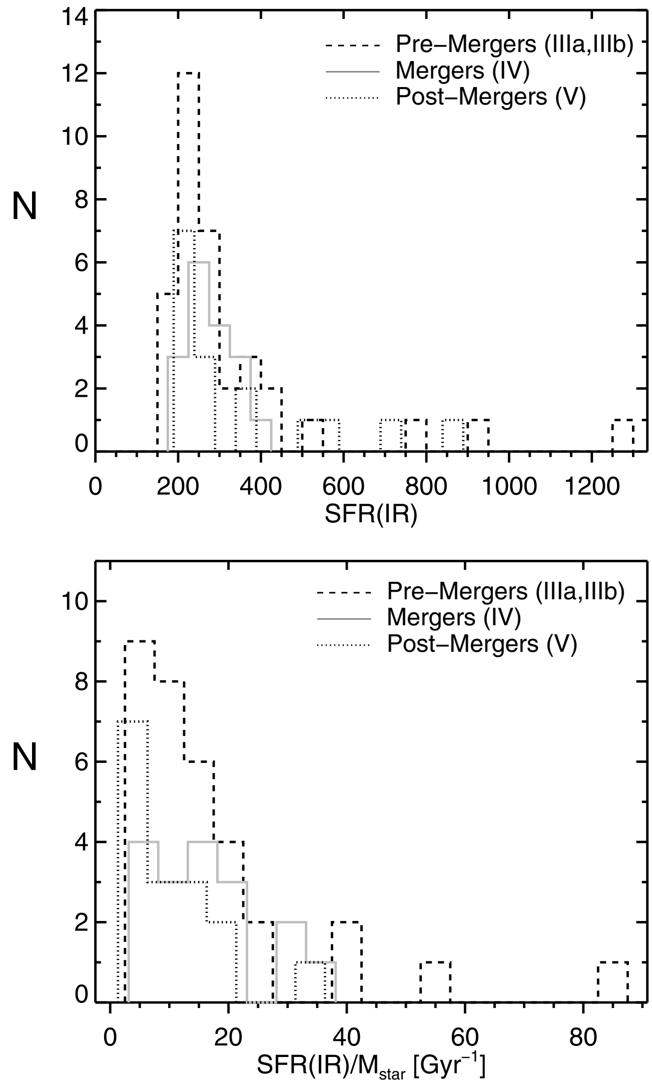

Figure 16. SFR(IR) (top) and specific star-formation rate (SFR/$M_{\rm star}$) (bottom) distribution of 68 ULIRGs as a function of interaction stage.

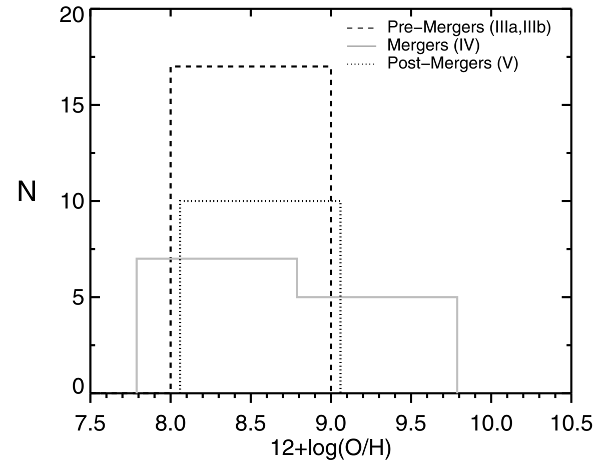

Figure 17. Oxygen abundance distributions of 39 ULIRGs as a function of interaction stage.

histories (SFHs). In particular, $M_{\rm star}$ estimates of ULIRGs like complex galaxies from SED fitting can be very sensitive to the assumed SFHs. As shown by Michałowski et al. (2012) and Michałowski (2014), using multicomponent SFHs that fit young and old populations result in systematically higher stellar masses compared to exponentially declining SFH. Therefore, it is very likely that the adopted $M_{\rm star}$ values in this work are underestimated. Obtaining the most robust stellar mass estimates of ULIRGs is beyond the scope of this paper, but with the available data we are able to assign an uncertainty limit. Considering the $M_{\rm star}$ differences of two (because it is an exceptional case, we exclude J0900252+390400) ULIRGs with respect to the values reported by Rodríguez Zaurín et al. (2010) and da Cunha et al. (2010), all of the adopted $M_{\rm star}$ values in this work might be underestimated by 0.06 dex–0.5 dex. A natural consequent question is the effect of this underestimate in Figure 10. To be conservative, we may assume that $M_{\rm star}$ are underestimated by 0.5 dex. As shown in Figure 15, if we shift stellar masses by 0.5 dex, ULIRGs still exhibit a large offset from the $z \sim 0$ and $z \sim 1$ main sequence, but they are consistent with the $z \sim 2$ main sequence. This shows that even the stellar masses adopted in Figure 10 are underestimated, but this does not change the main conclusion that ULIRGs are outliers compared to the $z \sim 0$ and $z \sim 1$ main sequence. However, it indicates that their offset from the $z \sim 2$ "main sequence" is very likely due to their underestimated stellar masses. Of course Figure 15 is a simple illustration and might not reflect the $M_{\rm star}$ distribution of ULIRGs at all; thus we caution against its interpretation.

4.6. Comparison of SFRs with Observations and Simulations of Mergers

The ULIRGs are interacting systems and are mostly ongoing or late mergers, and their extreme SFRs are generally attributed to merger events. Observations support this link: the SFRs of local ULIRGs are consistent with the observed enhanced SFR of mergers (e.g., Ellison et al. 2008, 2013). Moreover, the role of merger processes in triggering the SFR is a general prediction of merger models showing that major mergers cause nuclear gas inflows (Barnes & Hernquist 1991, 1996), and these inflows generate an intense SFR that peaks around when merging galaxies coalesce (e.g., Di Matteo et al. 2005, 2007; Springel et al. 2005; Montuori et al. 2010; Torrey et al. 2012). Merger models show that star-formation activity increases after the first peri-center passage and reaches its maximum level when two galaxies coalesce. In this picture we expect to observe lower SFRs in the premerger (widely or closely separated binaries) ULIRGs compared to the ULIRGs in the coalescence phase. In order to check whether the observed SFRs of our ULIRG sample are consistent with this prediction, in the top panel of Figure 16 the SFR(IR) distribution of ULIRGs is shown as a function of interaction class (defined in Section 3.2). We find that ULIRGs do not show a systematic difference in SFR(IR) for different interaction stages. We do not find the coalescence stage to be the peak of the SFR, as suggested by general merger simulations (e.g., Torrey et al. 2012). Because the SFR is correlated with stellar mass, in the bottom panel of Figure 16 we show a specific star-formation rate, sSFR (SFR(IR)/$M_{\rm star}$), as a function of interaction class. This panel shows a distribution similar to the top one: sSFR does not depend on the interaction stage. Of course this does not mean that ULIRGs are completely inconsistent with the merger models because we are not tracing single merger events in time as simulations do. Instead we are looking at different snapshots of merger events for different sources. Therefore, Figure 16 is rather consistent with the observations Rodríguez Zaurín et al. (2010) showing that ULIRGs have complex multistellar populations. In some ULIRGs, the SF activity triggered in

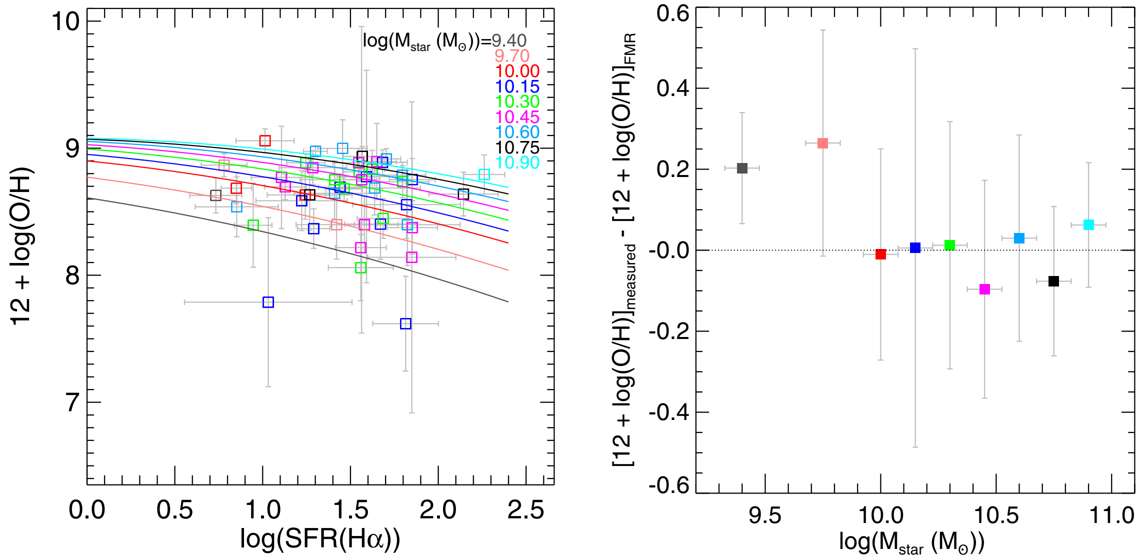

Figure 18. Left panel: FMR (Equation (2) of Mannucci et al. 2010) for different mass bins as a function of SFR. The colored lines show the mass bin. The colored open squares show the ULIRGs in each mass bin. Right panel: metallicity residuals of ULIRGs from the FMR; the colors represent the same mass bins labeled in the left panel. The residuals represent the median values in each bin, except for the first and the last bins, which have single measurements.

precoalescence epochs is probably comparable with that of the other coalescence phase; thus we see a similar distribution for different interaction phases.

Merger simulations also predict that nuclear gas inflows in the periods prior to increasing SFR epochs cause nuclear metallicity dilution, but afterward high SFRs cause metallicity enhancement (e.g., Torrey et al. 2012), so the overall metallicity change has a rather complex fluctuating nature as the merger progresses. In Figure 17, we show the oxygen abundance distribution of ULIRGs as a function of merger stage. Again the three distributions (premerger, merger, and postmerger) overlap and do not show a significant difference. As discussed above, we do not probe the evolution of oxygen abundances for individual ULIRGs as simulations do, so based on Figure 17 we cannot conclude any inconsistency with their predictions. However, when we compare oxygen abundances of ULIRGs with that of normal SFGs, we find that they systematically have lower oxygen abundances, and this is consistent with the predictions of the numerical simulations (e.g., Torrey et al. 2012). Similarly, interacting galaxies such as close pairs (e.g., Kewley et al. 2006; Ellison et al. 2008) do not lie on the $M_{\rm star}$–Z relation. These interacting, merging galaxies exhibit a lower metallicity than the noninteracting normal SFGs.

4.7. ULIRGs in the Fundamental Metallicity–Mass–SFR Plane

Figure 13 shows that ULIRGs have lower metallicities with respect to the $M_{\rm star}$–Z relation. The possible systematic uncertainties discussed in Section 4.5 are relevant to Figure 13, too. However, because the $M_{\rm star}$–Z relation is rather flat with increasing stellar mass, a shift of 0.5 dex in $M_{\rm star}$ does not change the observed scatter of ULIRGs.

Figure 10 indicates that local ULIRGs have SFRs comparable with $z \sim 2.0$ galaxies, and it is known that $z \sim 2.2$ galaxies have lower metallicities compared to local galaxies with the same masses (Erb et al. 2006; Tadaki et al. 2013). A similar result was also found for even higher redshift galaxies of $z = 3$–4 (Maiolino et al. 2008; Mannucci et al. 2009).

Star-forming galaxies up to $z \sim 2.5$ follow the fundamental metallicity relation (FMR), a tight relation between $M_{\rm star}$, gas metallicity, and SFR (Mannucci et al. 2010). This relation indicates that metallicity decreases with increasing SFR for low $M_{\rm star}$, but for high $M_{\rm star}$ it does not change with SFR. So, according to the FMR at a fixed mass we expect to have lower metallicities with increasing SFR. In order to understand if the lower metallicities of ULIRGs are due to higher SFRs, we need to check if they are on the FMR plane. We base this investigation on the FMR defined by Mannucci et al. (2010) for local SDSS galaxies. Following (Mannucci et al. 2010), we divide 47 (H)ULIRGs into 11 mass bins of 0.15 dex from $\log(M_{\rm star}(M_\odot)) = 9.70$ to 10.90. We only consider the bins containing at least one galaxy, and this selection results in 9 mass bins. To be consistent with Mannucci et al. (2010), we use the SFR(Hα) estimates obtained in Section 3.4.1. Because ULIRGs typically have larger SFRs, we extrapolate Equation (2) of Mannucci et al. (2010) up to log SFR(Hα) = 2.4. The left panel in Figure 18 shows the local FMR (Equation (2) of Mannucci et al. 2010) for these mass bins (color coded), where open circles show the distribution of ULIRGs in each mass bin (color coded with respect to mass). The right panel in Figure 18 shows the residuals between the measured metallicities of ULIRGs and FMR. These are the median values in each bin, but the first and the last bin represent residuals of single measurements. Without considering the uncertainties, the residuals of ULIRGs from the FMR are between 0.09 dex–0.26 dex. This is of course larger than the dispersions of the local SDSS galaxies that are $\sim$0.05 dex, but it indicates that local ULIRGs are consistent with the FMR. We also note that the residuals of local ULIRGs are comparable with that of high-redshift $z \sim 2$ galaxies (Mannucci et al. 2010). If we consider the uncertainties, the largest residual is $\sim$0.5 dex; this might indicate an inconsistency with the FMR. We used the same recipe to infer oxygen abundances and SFRs, so the offset of 0.5 dex cannot be due to metallicity or SFR measurements themselves. However, the largest contribution to the metallicity uncertainties comes directly from the emission-line flux uncertainties, and this point can only be addressed with higher quality data. So the large uncertainties showing $\sim$0.5 dex residuals do not necessarily mean a real offset from the FMR. However, also note that ULIRGs are interacting rare local galaxies with very high SFR, and they are expected to show a large scatter around the FMR (Mannucci et al. 2010).

4.8. ULIRGs in a Color–Magnitude Diagram

In Section 3.4.3 we found that local ULIRGs are optically bright and blue galaxies. As noted before, this is consistent with their starburst nature. However, ULIRGs are dusty galaxies, and one might expect them to have redder colors due to dust extinction. However, as suggested by Chen et al. (2010), the dust distribution in ULIRGs might not be uniform, and therefore their stellar light is not completely obscured.

The low fraction of ULIRGs in the green valley, as suggested by Chen et al. (2010), indicates that ULIRGs are rapidly SFGs, and they have not yet evolved into a transition phase. The evolution tracks of ULIRGs in the color–magnitude diagram is beyond the scope of this paper; for a discussion on this topic we refer readers to Chen et al. (2010).

5. CONCLUSIONS

We identified ULIRGs in the *AKARI* all-sky survey by cross-matching the *AKARI* catalogs with SDSS DR 10 and 2dFGRS. With the advantage of *AKARI* and the available SDSS data, we are able to investigate morphologies, stellar masses, SFRs, gas metallicities, and optical colors of a large sample of local ULIRGs. We examined the SFR–$M_{\rm star}$, $M_{\rm star}$–Z, SFR–$M_{\rm star}$–Z, and color–magnitude relations of our local ULIRG sample. The following summarizes the main conclusions from this work.

1. A sample of 118 ULIRGs and one HLIRG with $F(90\,\mu{\rm m}) \geqslant 0.22$ Jy have been identified in the *AKARI* all-sky survey. Forty of the ULIRGs and one HLIRG are newly identified in the *AKARI* all-sky survey based on the spectroscopic redshifts from SDSS DR10 and 2dFGRS. The redshift range of our ULIRG sample is $0.050 < z < 0.487$ and the median redshift is 0.181.
2. In the redshift ($z < 0.27$) limited sample of 100 ULIRGs, all show interaction features, either between two galaxies or in a single system. Only 5% are interacting triplets, 43% of the ULIRGs are two-galaxy systems with strong tidal tails or bridges, and 52% of the ULIRGs are ongoing/post mergers showing strong tidal tails or disturbed morphology. Our results support the known picture of ULIRGs as mergers.
3. Based on the adopted optical emission-line diagnostics, we confirm the known trend of increasing AGN fraction with higher IR luminosity.
4. Compared to SFR(IR), SFR(Hα) strongly underestimates the SFR of local ULIRGs by a factor of $\sim$8. This implies that IR observations provide the best estimate of SFR for highly star-forming dusty galaxies.
5. The ULIRGs have significantly higher SFRs than do the main sequence of normal SFGs up to $z \sim 2$. Local ULIRGs have 92, 17, and 5 times higher SFRs than do the main sequence galaxies with similar mass at $z \sim 0$, $z \sim 1$, and $z \sim 2$, respectively. Most of the local ULIRGs have lower SFRs than do the off-main sequence galaxies at $z \sim 2$.
6. We find that ULIRGs have lower gas metallicities compared to the $M_{\rm star}$–Z relation of normal star-forming galaxies; hence we confirm previous studies. We also find that local ULIRGs follow the FMR with high dispersions between 0.09 dex–0.5 dex, which is similar to that of high-redshift ($z \sim 2$–3) galaxies.
7. Compared to previous studies, we investigate the color properties of a larger ULIRG sample and find that 81% of the ULIRGs are in the blue cloud, 12% are in the "red sequence," and 7% are in the green valley. The vast majority of local ULIRGs in our sample are blue galaxies.

We provide the largest local ULIRG comparison sample to further study the $M_{\rm star}$, SFRs, gas metallicities, and optical colors of high-redshift ULIRGs.

We thank the anonymous referee for many insightful comments. We thank Marianne Vestergaard and Jens Hjorth for their comments. The Dark Cosmology Centre is funded by the Danish National Research Foundation. *AKARI* is a JAXA project with the participation of universities and research institutes in Japan, the European Space Agency (ESA), the IOSG (Imperial College, UK, Open University, UK, University of Sussex, UK, and University of Groningen, Netherlands) Consortium, and Seoul National University, Korea. Funding for SDSS-III has been provided by the Alfred P. Sloan Foundation, the participating institutions, the National Science Foundation, and the U.S. Department of Energy Office of Science. The SDSS-III Web site is http://www.sdss3.org/. SDSS-III is managed by the Astrophysical Research Consortium for the participating institutions of the SDSS-III Collaboration, including the University of Arizona, the Brazilian Participation Group, Brookhaven National Laboratory, Carnegie Mellon University, University of Florida, the French Participation Group, the German Participation Group, Harvard University, the Instituto de Astrofisica de Canarias, the Michigan State/Notre Dame/JINA Participation Group, Johns Hopkins University, Lawrence Berkeley National Laboratory, Max Planck Institute for Astrophysics, Max Planck Institute for Extraterrestrial Physics, New Mexico State University, New York University, Ohio State University, Pennsylvania State University, University of Portsmouth, Princeton University, the Spanish Participation Group, University of Tokyo, University of Utah, Vanderbilt University, University of Virginia, University of Washington, and Yale University. The digitized sky surveys were produced at the Space Telescope Science Institute under U.S. government grant NAG W-2166. The images of these surveys are based on photographic data obtained using the Oschin Schmidt Telescope on Palomar Mountain and the UK Schmidt Telescope. The plates were processed into the present compressed digital form with the permission of these institutions. The National Geographic Society-Palomar Observatory Sky Atlas (POSS-I) was made by the California Institute of Technology with grants from the National Geographic Society. The Second Palomar Observatory Sky Survey (POSS-II) was made by the California Institute of Technology with funds from the National Science Foundation, the National Geographic Society, the Sloan Foundation, the Samuel Oschin Foundation, and the Eastman Kodak Corporation. The Oschin Schmidt Telescope is operated by the California Institute of Technology and Palomar Observatory. The UK Schmidt Telescope was operated by the Royal Observatory Edinburgh, with funding from the UK Science and Engineering Research Council (later the UK Particle Physics and Astronomy Research Council), until 1988 June, and thereafter by the Anglo-Australian Observatory. The blue plates of the southern Sky Atlas and its Equatorial Extension (together known as the SERC-J), as well as the Equatorial Red (ER), and the Second Epoch [red] Survey (SES) were all taken with the UK Schmidt. This research has made use of NASA's Astrophysics Data System Bibliographic Service.

APPENDIX

IR IMAGES OF NEWLY IDENTIFIED SOURCES

We present the IR (AKARI 90 μm) images of the newly identified ULIRGs and one HLIRG in Figure A1.

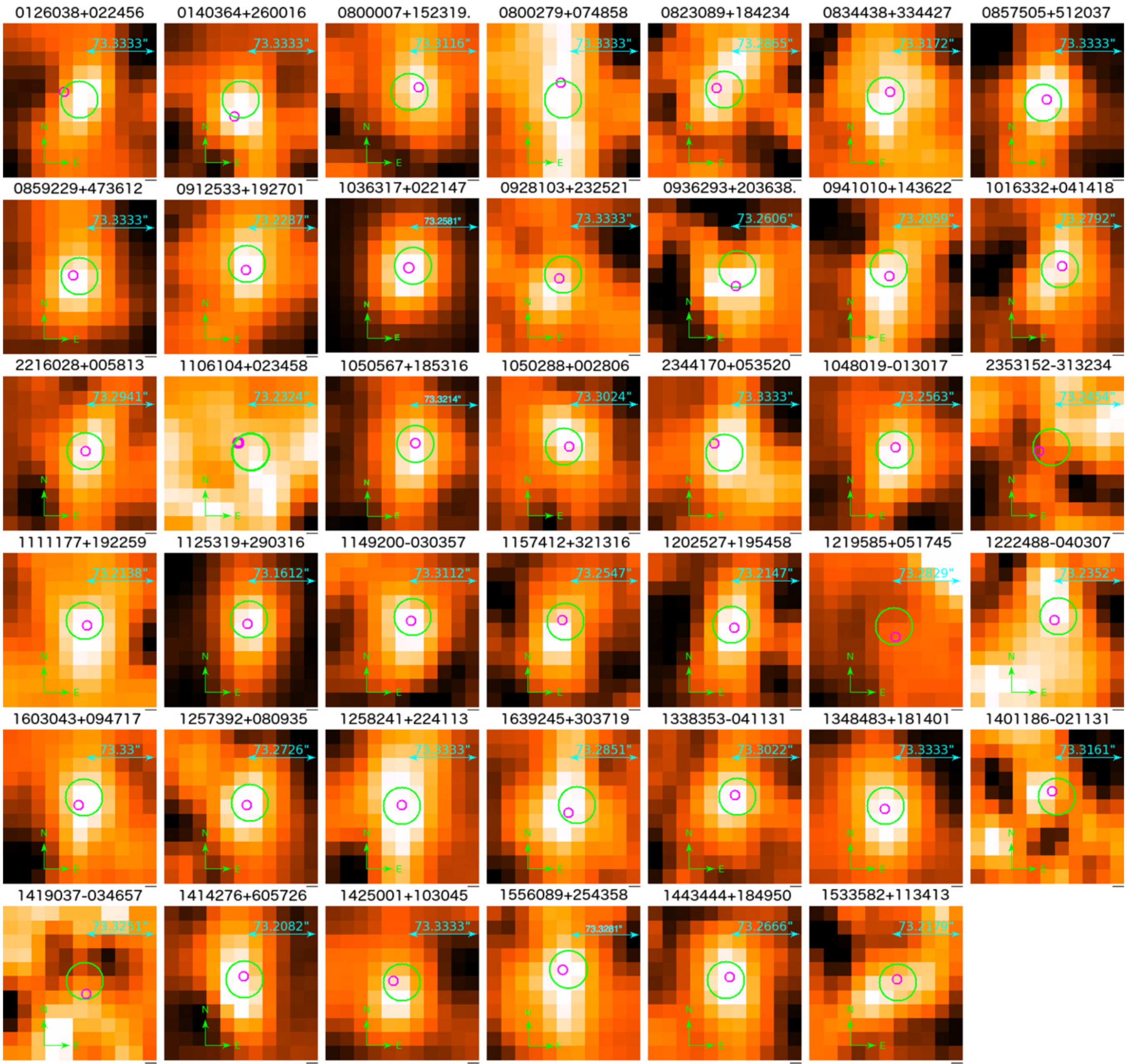

Figure A1. *AKARI* 90 μm images of all of the newly identified ULIRGs and one HLIRG. The scale of the images is $165'' \times 165''$. The $5''$ radius small circles (colored magenta in the online version) represent the optical counterpart, and the $20''$ radius big circle (colored green in the online version) shows the IR source.

(A color version of this figure is available in the online journal.)

REFERENCES

Abazajian, K., Adelman-McCarthy, J. K., Agüeros, M. A., et al. 2004, AJ, 128, 502

Abazajian, K., Adelman-McCarthy, J. K., Agüeros, M. A., et al. 2005, AJ, 129, 1755

Abazajian, K. N., Adelman-McCarthy, J. K., Agüeros, M. A., et al. 2009, ApJS, 182, 543

Adelman-McCarthy, J. K., Agüeros, M. A., Allam, S. S., et al. 2006, ApJS, 162, 38

Adelman-McCarthy, J. K., Agüeros, M. A., Allam, S. S., et al. 2008, ApJS, 175, 297

Ahn, C. P., Alexandroff, R., Allende Prieto, C., et al. 2014, ApJS, 211, 17

Arnouts, S., Cristiani, S., Moscardini, L., et al. 1999, MNRAS, 310, 540

Baldry, I. K., Balogh, M. L., Bower, R. G., et al. 2006, MNRAS, 373, 469

Baldry, I. K., Glazebrook, K., Brinkmann, J., et al. 2004, ApJ, 600, 681

Baldwin, J. A., Phillips, M. M., & Terlevich, R. 1981, PASP, 93, 5

Barnes, J. E., & Hernquist, L. 1996, ApJ, 471, 115

Barnes, J. E., & Hernquist, L. E. 1991, ApJL, 370, L65

Bell, E. F., Wolf, C., Meisenheimer, K., et al. 2004, ApJ, 608, 752

Blanton, M. R., Eisenstein, D., Hogg, D. W., Schlegel, D. J., & Brinkmann, J. 2005, ApJ, 629, 143

Blanton, M. R., Hogg, D. W., Bahcall, N. A., et al. 2003, ApJ, 594, 186

Blanton, M. R., & Roweis, S. 2007, AJ, 133, 734

Bolton, A. S., Schlegel, D. J., Aubourg, É., et al. 2012, AJ, 144, 144

Brinchmann, J., Charlot, S., White, S. D. M., et al. 2004, MNRAS, 351, 1151

Bruzual, G., & Charlot, S. 2003, MNRAS, 344, 1000

Calzetti, D. 2001, PASP, 113, 1449

Cao, C., Wu, H., Wang, J.-L., et al. 2006, ChJAA, 6, 197

Caputi, K. I., Lagache, G., Yan, L., et al. 2007, ApJ, 660, 97

Chary, R., & Elbaz, D. 2001, ApJ, 556, 562

Chen, Y., Lowenthal, J. D., & Yun, M. S. 2010, ApJ, 712, 1385

Chen, Y.-M., Kauffmann, G., Tremonti, C. A., et al. 2012, MNRAS, 421, 314
Clements, D. L., Sutherland, W. J., Saunders, W., et al. 1996, MNRAS, 279, 459
Colless, M. 2004, PASA, 21, 352
Colless, M., Dalton, G., Maddox, S., et al. 2001, MNRAS, 328, 1039
Cooper, M. C., Newman, J. A., Croton, D. J., et al. 2006, MNRAS, 370, 198
da Cunha, E., Charmandaris, V., Díaz-Santos, T., et al. 2010, A&A, 523, A78
Daddi, E., Bournaud, F., Walter, F., et al. 2010, ApJ, 713, 686
Daddi, E., Dannerbauer, H., Stern, D., et al. 2009, ApJ, 694, 1517
Daddi, E., Dickinson, M., Morrison, G., et al. 2007, ApJ, 670, 156
Dale, D. A., & Helou, G. 2002, ApJ, 576, 159
Dale, D. A., Helou, G., Contursi, A., Silbermann, N. A., & Kolhatkar, S. 2001, ApJ, 549, 215
Dasyra, K. M., Tacconi, L. J., Davies, R. I., et al. 2006a, ApJ, 638, 745
Dasyra, K. M., Tacconi, L. J., Davies, R. I., et al. 2006b, ApJ, 651, 835
Di Matteo, P., Combes, F., Melchior, A.-L., & Semelin, B. 2007, A&A, 468, 61
Di Matteo, T., Springel, V., & Hernquist, L. 2005, Natur, 433, 604
Doi, Y., Komugi, S., Kawada, M., et al. 2012, PKAS, 27, 111
Downes, D., & Solomon, P. M. 1998, ApJ, 507, 615
Driver, S. P., Allen, P. D., Graham, A. W., et al. 2006, MNRAS, 368, 414
Elbaz, D., Daddi, E., Le Borgne, D., et al. 2007, A&A, 468, 33
Ellison, S. L., Mendel, J. T., Scudder, J. M., Patton, D. R., & Palmer, M. J. D. 2013, MNRAS, 430, 3128
Ellison, S. L., Patton, D. R., Simard, L., & McConnachie, A. W. 2008, AJ, 135, 1877
Erb, D. K., Shapley, A. E., Pettini, M., et al. 2006, ApJ, 644, 813
Faber, S. M., Willmer, C. N. A., Wolf, C., et al. 2007, ApJ, 665, 265
Farrah, D., Lonsdale, C. J., Weedman, D. W., et al. 2008, ApJ, 677, 957
Farrah, D., Rowan-Robinson, M., Oliver, S., et al. 2001, MNRAS, 326, 1333
Fisher, K. B., Huchra, J. P., Strauss, M. A., et al. 1995, ApJS, 100, 69
Gehrels, N. 1986, ApJ, 303, 336
Genzel, R., Lutz, D., Sturm, E., et al. 1998, ApJ, 498, 579
Goldader, J. D., Joseph, R. D., Doyon, R., & Sanders, D. B. 1995, ApJ, 444, 97
Goto, T. 2005, MNRAS, 360, 322
Goto, T., Arnouts, S., Inami, H., et al. 2011a, MNRAS, 410, 573
Goto, T., Arnouts, S., Malkan, M., et al. 2011b, MNRAS, 414, 1903
Guo, K., Zheng, X. Z., & Fu, H. 2013, ApJ, 778, 23
Heckman, T. M., Lehnert, M. D., Strickland, D. K., & Armus, L. 2000, ApJS, 129, 493
Helou, G. 1986, ApJL, 311, L33
Hogg, D. W., Blanton, M. R., Eisenstein, D. J., et al. 2003, ApJL, 585, L5
Hopkins, P. F., Cox, T. J., Dutta, S. N., et al. 2009, ApJS, 181, 135
Hopkins, P. F., Cox, T. J., Kereš, D., & Hernquist, L. 2008a, ApJS, 175, 390
Hopkins, P. F., Hernquist, L., Cox, T. J., & Kereš, D. 2008b, ApJS, 175, 356
Hopkins, P. F., Hernquist, L., Cox, T. J., Robertson, B., & Krause, E. 2007, ApJ, 669, 45
Hopkins, P. F., Hernquist, L., Cox, T. J., et al. 2006, ApJS, 163, 1
Hou, L. G., Wu, X.-B., & Han, J. L. 2009, ApJ, 704, 789
Hwang, H. S., Serjeant, S., Lee, M. G., Lee, K. H., & White, G. J. 2007, MNRAS, 375, 115
Ilbert, O., Arnouts, S., McCracken, H. J., et al. 2006, A&A, 457, 841
Imanishi, M. 2009, ApJ, 694, 751
Ishida, C. M. 2004, PhD thesis, Univ. Hawai'i
Johnson, S. P., Wilson, G. W., Wang, Q. D., et al. 2013, MNRAS, 431, 662
Jones, D. H., Saunders, W., Colless, M., et al. 2004, MNRAS, 355, 747
Kartaltepe, J. S., Dickinson, M., Alexander, D. M., et al. 2012, ApJ, 757, 23
Kauffmann, G., Heckman, T. M., Tremonti, C., et al. 2003a, MNRAS, 346, 1055
Kauffmann, G., Heckman, T. M., White, S. D. M., et al. 2003b, MNRAS, 341, 54
Kennicutt, R. C., Jr. 1998, ARA&A, 36, 189
Kewley, L. J., Geller, M. J., & Barton, E. J. 2006, AJ, 131, 2004
Kim, D.-C., & Sanders, D. B. 1998, ApJS, 119, 41
Kim, D.-C., Veilleux, S., & Sanders, D. B. 1998, ApJ, 508, 627
Kim, D.-C., Veilleux, S., & Sanders, D. B. 2002, ApJS, 143, 277
Kroupa, P. 2001, MNRAS, 322, 231
Lagache, G., Dole, H., & Puget, J.-L. 2003, MNRAS, 338, 555
Lara-López, M. A., Cepa, J., Bongiovanni, A., et al. 2010, A&A, 521, L53
Lawrence, A., Rowan-Robinson, M., Ellis, R. S., et al. 1999, MNRAS, 308, 897
Le Floc'h, E., Papovich, C., Dole, H., et al. 2005, ApJ, 632, 169
Lonsdale, C. J., Farrah, D., & Smith, H. E. 2006, in Astrophysics Update 2, Ultraluminous Infrared Galaxies ed. J. W. Mason (Heidelberg: Springer), 285
Maiolino, R., Nagao, T., Grazian, A., et al. 2008, A&A, 488, 463
Mannucci, F., Cresci, G., Maiolino, R., Marconi, A., & Gnerucci, A. 2010, MNRAS, 408, 2115
Mannucci, F., Cresci, G., Maiolino, R., et al. 2009, MNRAS, 398, 1915
Maoz, D., Koratkar, A., Shields, J., et al. 1998, AJ, 116, 55
Maraston, C. 2005, MNRAS, 362, 799
Maraston, C., Pforr, J., Henriques, B. M., et al. 2013, MNRAS, 435, 2764
Maraston, C., & Strömbäck, G. 2011, MNRAS, 418, 2785
Maraston, C., Strömbäck, G., Thomas, D., Wake, D. A., & Nichol, R. C. 2009, MNRAS, 394, L107
Michałowski, M. J., Dunlop, J. S., Cirasuolo, M., et al. 2012, A&A, 541, A85
Michałowski, M. J., Hayward, C. C., Dunlop, J. S., et al. 2014, arXiv:1405.2335
Mihos, J. C., & Hernquist, L. 1996, ApJ, 464, 641
Montuori, M., Di Matteo, P., Lehnert, M. D., Combes, F., & Semelin, B. 2010, A&A, 518, A56
Moshir, M., Kopman, G., & Conrow, T. A. O. 1992, IRAS Faint Source Survey, Explanatory Supplement, Version 2, ed. M. Moshir, G. Kopman, & T. Conrow (Pasadena, CA: California Institute of Technology)
Murakami, H., Baba, H., Barthel, P., et al. 2007, PASJ, 59, 369
Muzzin, A., Wilson, G., Yee, H. K. C., et al. 2012, ApJ, 746, 188
Nagar, N. M., Falcke, H., & Wilson, A. S. 2005, A&A, 435, 521
Nardini, E., Risaliti, G., Watabe, Y., Salvati, M., & Sani, E. 2010, MNRAS, 405, 2505
Noeske, K. G., Weiner, B. J., Faber, S. M., et al. 2007, ApJL, 660, L43
Osterbrock, D. E., & Ferland, G. J. 2006, Astrophysics of Gaseous Nebulae and Active Galactic Nuclei (Mill Valley, CA: University Science Books)
Pasquali, A., Kauffmann, G., & Heckman, T. M. 2005, MNRAS, 361, 1121
Pier, J. R., Munn, J. A., Hindsley, R. B., et al. 2003, AJ, 125, 1559
Richards, G. T., Fan, X., Newberg, H. J., et al. 2002, AJ, 123, 2945
Rieke, G. H., Alonso-Herrero, A., Weiner, B. J., et al. 2009, ApJ, 692, 556
Rodighiero, G., Daddi, E., Baronchelli, I., et al. 2011, ApJL, 739, L40
Rodríguez Zaurín, J., Tadhunter, C. N., & González Delgado, R. M. 2010, MNRAS, 403, 1317
Rowan-Robinson, M. 2000, MNRAS, 316, 885
Rujopakarn, W., Rieke, G. H., Eisenstein, D. J., & Juneau, S. 2011, ApJ, 726, 93
Rupke, D. S., Veilleux, S., & Sanders, D. B. 2002, ApJ, 570, 588
Rupke, D. S., Veilleux, S., & Sanders, D. B. 2005, ApJS, 160, 115
Rupke, D. S. N., & Veilleux, S. 2011, ApJL, 729, L27
Rupke, D. S. N., & Veilleux, S. 2013, ApJ, 768, 75
Rupke, D. S. N., Veilleux, S., & Baker, A. J. 2008, ApJ, 674, 172
Salpeter, E. E. 1955, ApJ, 121, 161
Sanders, D. B., Mazzarella, J. M., Kim, D.-C., Surace, J. A., & Soifer, B. T. 2003, AJ, 126, 1607
Sanders, D. B., & Mirabel, I. F. 1996, ARA&A, 34, 749
Sanders, D. B., Soifer, B. T., Elias, J. H., Neugebauer, G., & Matthews, K. 1988a, ApJL, 328, L35
Sanders, D. B., Soifer, B. T., Elias, J. H., et al. 1988b, ApJ, 325, 74
Santini, P., Fontana, A., Grazian, A., et al. 2009, A&A, 504, 751
Santini, P., Maiolino, R., Magnelli, B., et al. 2014, A&A, 562, A30
Sarzi, M., Falcón-Barroso, J., Davies, R. L., et al. 2006, MNRAS, 366, 1151
Sarzi, M., Shields, J. C., Schawinski, K., et al. 2010, MNRAS, 402, 2187
Saunders, W., Sutherland, W. J., Maddox, S. J., et al. 2000, MNRAS, 317, 55
Schawinski, K., Thomas, D., Sarzi, M., et al. 2007, MNRAS, 382, 1415
Siebenmorgen, R., & Krügel, E. 2007, A&A, 461, 445
Soifer, B. T., & Neugebauer, G. 1991, AJ, 101, 354
Soifer, B. T., Neugebauer, G., Matthews, K., et al. 2000, AJ, 119, 509
Soifer, B. T., Sanders, D. B., Madore, B. F., et al. 1987, ApJ, 320, 238
Spoon, H. W. W., Farrah, D., Lebouteiller, V., et al. 2013, ApJ, 775, 127
Springel, V., Di Matteo, T., & Hernquist, L. 2005, MNRAS, 361, 776
Stanford, S. A., Stern, D., van Breugel, W., & De Breuck, C. 2000, ApJS, 131, 185
Strauss, M. A., Huchra, J. P., Davis, M., et al. 1992, ApJS, 83, 29
Surace, J. A. 1998, PhD thesis, Institute for Astronomy University of Hawaii 2680 Woodlawn Dr. Honolulu, HI 96822
Tacconi, L. J., Genzel, R., Neri, R., et al. 2010, Natur, 463, 781
Tacconi, L. J., Genzel, R., Smail, I., et al. 2008, ApJ, 680, 246
Tadaki, K.-i., Kodama, T., Tanaka, I., et al. 2013, ApJ, 778, 114
Takagi, T., Ohyama, Y., Goto, T., et al. 2010, A&A, 514, A5
Takagi, T., Ono, Y., Shimasaku, K., & Hanami, H. 2008, MNRAS, 389, 775
Thomas, D., Steele, O., Maraston, C., et al. 2013, MNRAS, 431, 1383
Toomre, A., & Toomre, J. 1972, ApJ, 178, 623

Torrey, P., Cox, T. J., Kewley, L., & Hernquist, L. 2012, ApJ, 746, 108
Tremonti, C. A., Heckman, T. M., Kauffmann, G., et al. 2004, ApJ, 613, 898
Veilleux, S., Kim, D.-C., Peng, C. Y., et al. 2006, ApJ, 643, 707
Veilleux, S., Kim, D.-C., & Sanders, D. B. 1999a, ApJ, 522, 113
Veilleux, S., Kim, D.-C., & Sanders, D. B. 2002, ApJS, 143, 315
Veilleux, S., Kim, D.-C., Sanders, D. B., Mazzarella, J. M., & Soifer, B. T. 1995, ApJS, 98, 171
Veilleux, S., Meléndez, M., Sturm, E., et al. 2013, ApJ, 776, 27
Veilleux, S., Rupke, D. S. N., Kim, D.-C., et al. 2009, ApJS, 182, 628
Veilleux, S., Sanders, D. B., & Kim, D.-C. 1999b, ApJ, 522, 139
Wang, L., & Rowan-Robinson, M. 2009, MNRAS, 398, 109
Wyder, T. K., Martin, D. C., Schiminovich, D., et al. 2007, ApJS, 173, 293
Yamamura, I., Makiuti, S., Ikeda, N., et al. 2010, yCat, 2298, 0
York, D. G., Adelman, J., Anderson, J. E., Jr., et al. 2000, AJ, 120, 1579